UNIVERSITY OF CALIFORNIA
SANTA CRUZ

PHASE TRANSITIONS IN THE EARLY UNIVERSE

A dissertation submitted in partial satisfaction of the
requirements for the degree of

DOCTOR OF PHILOSOPHY

in

PHYSICS

by

Carroll L. Wainwright

June 2013

The Dissertation of Carroll L. Wainwright
is approved:

Stefano Profumo, Chair

Anthony Aguirre

Tom Banks

Tyrus Miller
Vice Provost and Dean of Graduate Studies

Table of Contents

List of Figures

List of Tables

Abstract

Phase Transitions in the Early Universe

by

Carroll L. Wainwright

I explore the theory and computation of early-Universe finite-temperature phase transitions involving scalar fields. I focus primarily on the electroweak phase transition, but some of the methods I develop are applicable to any scalar-field cosmological phase transition (such as the computation of the lifetime of zero-temperature metastable vacua). I begin by examining phase transition thermodynamics with many extra coupled degrees of freedom, finding that such transitions have the potential to produce large amounts of entropy and can significantly dilute the concentration of thermal relic species (e.g., dark matter). I then detail a novel algorithm for calculating instanton solutions with multiple dynamic scalar fields, and present a computational package which implements the algorithm and computes the finite-temperature phase structure. Next, I discuss theoretical and practical problems of gauge dependence in finite-temperature effective potentials, using the Abelian Higgs and Abelian Higgs plus singlet models to show the severity of the problem. Finally, I apply the aforementioned algorithm to the electroweak phase transition in the next-to-minimal supersymmetric standard model (NMSSM). My collaborators and I find viable regions of the NMSSM which contain a strongly first-order phase transition and large enough CP violation to support electroweak baryogenesis, evade electric dipole moment constraints, and provide a dark matter candidate which could produce the observed 130 GeV gamma-ray line observed in the galactic center by the Fermi Gamma-ray Space Telescope.

Acknowledgments

This dissertation depends upon years of work and support from my advisor, Stefano Profumo. Stefano got me started on research in my first year at UC Santa Cruz, and kept pushing me with new ideas for the next four. He has supervised most of the work that I have done, and all of the work that forms the basis of this thesis. Stefano is widely known (in our department anyway) as a marathon runner and triathlete, and he has been nice enough to help me take my mind off of physics for an hour or so by going on long runs through Wilder Ranch and Pogonip, always slowing down to keep pace with me. Thanks Stefano!

I'd also like to thank Tom Banks and Anthony Aguirre, with whom I have done more recent research. Both provided invaluable support over my graduate career. In particular, Tom taught me most of the field theory that I think I know, and about 90% of the field theory that I realize I'll need at least another five years to figure out. I thank Michael Ramsey-Musolf for getting me interested in the gauge dependence problem and largely supervising that portion of my research. And, although I haven't worked with him directly, I thank Michael Dine for always being happy to help with any physics questions that I have.

I really lucked out with my graduate student cohort, who are an all-around excellent group of people. I worked (and am working) with Jonathan Kozaczuk, TJ Torres, and Laurel Stephenson-Haskins, all of whom have been great physicists and collaborators. Thanks especially to my office mates Chris Moody, Laura Fava, Lauren Porter, and Tim Linden for all the support that they've provided and friendly atmosphere that they've kept.

Much credit has to go to Sophia Magnone, without whom there's no way I would have made it through five years of graduate school.

Finally, a very heartfelt thank you to my parents, for always encouraging me, and to my sister Adelaide, for teaching me how to be who I am today.

I gratefully acknowledge support from the Graduate Assistance in Areas of National Need (GAANN) program and the National Science Foundation Graduate Research Fellowship Program (NSF GRFP).

The text of this dissertation includes reprints of the following previously published material: C. Wainwright and S. Profumo, Phys. Rev. D **80**, 103517 (2009) [arXiv:0909.1317 [hep-ph]]; C. Wainwright, S. Profumo and M. J. Ramsey-Musolf, Phys. Rev. D **84**, 023521 (2011) [arXiv:1104.5487 [hep-ph]]; C. L. Wainwright, Comput. Phys. Commun. **183**, 2006 (2012) [arXiv:1109.4189 [hep-ph]]; C. L. Wainwright, S. Profumo and M. J. Ramsey-Musolf, Phys. Rev. D **86**, 083537 (2012) [arXiv:1204.5464 [hep-ph]]; and J. Kozaczuk, S. Profumo and C. L. Wainwright, arXiv:1302.4781 [hep-ph]. Stefano Profumo directed and supervised the research which forms the basis for this dissertation. In the work which comprises the third and fourth papers, Michael Ramsey-Musolf also performed a largely advisory role. In the final paper, Jonathan Kozaczuk and I both contributed significant amounts of original research: Jonathan was primarily responsible for the baryon asymmetry, Higgs mass, and neutralino self-annihiliation to gamma ray calculations; and I was responsible for the electric dipole moment and phase transition calculations.

Chapter 1

Introduction

The history of the Universe, in a certain sense, is one which is best told backwards: scientists know much more about the effect than the cause, and we ought to start with what we know. The effect is the messy state of the present. This includes the state of the galaxy and large-scale cosmology; the state of the solar system and its planets; the state of Earth and its inhabitants; the state of the State and the people and all the complicated social institutions of which I personally know very little. The cause is the underlying fundamental physics and the initial conditions at the big bang, about which no one knows more than very little (although theories abound).

So, let us start with the present, ignoring, for simplicity, all features that are smaller than a galaxy. The Universe is currently made up of 4.9% ordinary baryonic matter and 26.8% dark matter (the best measurements of cosmological parameters come from the very recent results of the Planck experiment [1]). The baryonic matter composes virtually everything that people can see (electrons are not baryons, but they are tiny compared to

atomic nuclei), as well as a large amount that we cannot see, or at least cannot see in visible light, such as interstellar gas. Dark matter is simply the name we give to the matter that we cannot see by any electromagnetic means, although we have been able to infer a great deal about it by observing its effects upon visible matter. It must be made of small particles (it cannot primarily be large clumps of dark baryonic matter or black holes); it must be cold (it cannot be moving at relativistic speeds); it must be electrically non-interacting (it cannot emit or reflect light); and it must be long-lived (it cannot decay to ordinary matter or radiation with a lifetime shorter than the age of the Universe). No particle in the Standard Model of particle physics fits this description. There are well-motivated theories beyond the Standard Model with dark matter candidates, but no one yet knows which of these theories is correct.

All of the matter in the Universe is flying away from all of the other matter in the Universe at a rate governed by the Hubble constant: $H_0 = 67.3 \pm 1.2$ km/s/Mpc. That is, two objects that are one megaparsec apart will tend to be moving with a relative speed of 67.3 kilometers per second in opposite directions. Or, perhaps more accurately, the distance between any two objects is growing at a rate of 67.3 km/s/Mpc even though in certain (co-moving) coordinates the two objects remain in exactly the same spots. This cosmic expansion is partly due to momentum — a universe in expansion tends to stay in expansion — and partly due to the remaining 68.3% of the Universe's energy budget. Ordinary matter acting through gravity slows down the expansion, but we know that the expansion is actually speeding up. We call the cause of the speed-up dark energy. It must have a few exotic properties (it has negative pressure, for instance), but we otherwise know

very little about what it actually is.

As we go back in time the expansion looks like contraction and the universe shrinks. The total amount of matter stays the same (at first), but the total amount of dark energy decreases. The *density* of dark energy stays constant, but since the total volume of the universe goes down the relative importance of dark energy goes down as well. Larger galaxies form out of the collisions of smaller proto-galaxies, and proto-galaxies and the earliest stars form out of over-dense regions in the primordial gas. Before this, the Universe was dark. But as we keep going back in time the primordial gas gets hotter and hotter: the Universe adiabatically cooled as it expanded in much the same way as air cools as it expands when one blows on a hot bowl of soup. If we go back far enough, to roughly 13.4 billion years ago or 380,000 years after the big bang, the primordial gas becomes an optically thick primordial plasma. This is as far as we can see by conventional means, and the plasma to gas transition constitutes the surface of last scattering, which we see today as the cosmic microwave background radiation (CMB). A tremendous amount of information can be inferred from the CMB (again, see [1]), but we can go back further still.

Before 70,000 years after the big bang, and at temperatures of roughly 1 eV (or 12,000 kelvin), radiation energy dominated over matter density. The matter density is inversely proportional to the Universe's volume, but the radiation density is inversely proportional to the volume to the 4/3 power, so it dominates when the Universe was small and hot. Rewinding to much earlier times, on the order of minutes after the big bang and at temperatures of around 10 MeV, the individual primordial atomic nuclei split into their constituent parts. The transition from free neutrons and protons to stable nuclei is known

as big bang nucleosynthesis, and it is extremely well-described by Standard Model physics. The observed primordial abundances of light elements beautifully matches our theoretical expectations [2], and represents a triumph of modern cosmology. With big bang nucleosynthesis, we are confident we understand the basic evolution of the Universe starting at just a few minutes after the big bang. But, we can go back further still.

At this point, data is no longer a reliable guide (yet!), and we must instead rely on theoretical knowledge. At even higher temperatures and earlier times, the neutrons and protons must have been broken into their constituent parts: quarks and gluons. The transition from the quark-gluon plasma into baryons and mesons is called the QCD (quantum chromodynamic) phase transition, and it happened at a temperature of around 100 MeV.

Before this, at temperatures above about 100 GeV, even the force-carrying bosons are broken into simpler parts. The $W^{\pm}$ and Z^0 bosons are normally massive (which is why the weak force is so weak), and they get their masses from the Higgs mechanism. The Higgs field is closely linked to the weak vector fields: it has four degrees of freedom, three of which, due to a broken symmetry, become the longitudinal parts of the $W^{\pm}$ and Z^0 bosons, with the remaining degree of freedom acting as the Higgs boson. At very high temperature the Higgs is unlinked from the weak bosons, which are then indistinguishable from the photon. This is known as the electroweak phase transition (EWPT). Above the EWPT, electroweak symmetry is unbroken and the Higgs field has zero vacuum expectation value (vev). Below the transition, the Higgs gets a non-zero vev and the weak and electromagnetic forces separate.

If we keep going back, theories get more uncertain (but again, there are lots of

well-motivated ideas). At around 10^{16} GeV, the electroweak force may have been unified with the strong nuclear force, in much the same way as the electric force is unified with the weak nuclear force. At some point supersymmetry may have been unbroken. At the very beginning of the Universe, there was almost definitely an inflationary epoch which exponentially grew space and set the seeds of primordial fluctuations which would later collapse into the structures that we see today.

The grand goal of this thesis (and of my five years of doctoral study) is to push our knowledge a little bit further back from where we are confident we know the answers — to determine a small piece of cosmic history before big bang nucleosynthesis. I focus on the theory and phenomenology of phase transitions involving scalar fields. The electroweak phase transition, in particular, has a rich set of phenomenological possibilities which may be probed and verified in current and upcoming experiments. The electroweak phase transition may have produced a substantial amount of entropy and heat, leading to an altered thermal history; it may have produced a measurable stochastic gravitational radiation background; and it may have been responsible for matter's predominance over anti-matter in the present via electroweak baryogenesis.

The rest of this thesis is organized as follows. In chapter 2, I discuss phase transition thermodynamics and a transition's potential to dilute the abundance of thermal relics. Chapter 3 details a numerical method for calculating instantons in multiple-field scenarios. These instantons are the bubbles of low-temperature phase ("true vacuum") that nucleate and then grow to fill the expanding Universe. In chapters 4 and 5, I discuss gauge problems in finite-temperature field theory, and how naive calculations lead to gauge-dependent

results. Chapter 4 focuses on the simplest possible such theory — the abelian Higgs model — while chapter 5 extends the theory to include a singlet, which one may have expected to mitigate the problem. However, I show that the problem persists even with the extra singlet. Chapter 6 details a region of the next to minimal supersymmetric standard model (NMSSM) which not only can produce the observed baryon asymmetry, but also evades electric dipole moment constraints and provides a dark matter candidate which matches the 130 GeV line seen by the Fermi gamma-ray space telescope. I conclude in chapter 7, and briefly mention some of the work I performed during my graduate studies not otherwise mentioned in this thesis, as well as plans for future study.

Chapter 2

The impact of a strongly first-order phase transition on the abundance of thermal relics

The particle content of the Minimal Supersymmetric extension of the Standard Model (MSSM) of particle physics (see e.g. [3]) provides a stable weakly interacting massive particle which is, in principle, a viable particle dark matter candidate: the lightest neutralino. If the latter is the lightest R-parity odd particle, its thermal relic abundance can be close to the inferred density of dark matter on cosmological scales [4], whose ratio to the universal critical density is estimated to be $\Omega_{\rm astro} = \rho_{\rm DM}/\rho_c = 0.113\ h^{-2}$ [5], with h the present day Hubble expansion rate normalized in units of 100 km per sec per Mpc.

Several studies have pointed out that the thermal relic abundance of neutralinos in MSSM models where they are the lightest supersymmetric particles actually ranges over several orders of magnitude, simple estimates of their relic abundance being therefore only a generic order-of-magnitude estimate (see e.g. [6, 7]). Specifically, if the lightest neutralino has unsuppressed couplings to gauge bosons, and is heavy enough for annihilation to massive weak interaction gauge bosons to be kinematically open, it rapidly annihilates into W^+W^- and/or ZZ final states, and its relic density $\Omega_{\rm particle}$ is *below* the dark matter density, at least for neutralinos lighter than about a TeV. If the lightest neutralino has suppressed couplings to gauge bosons, as is the case for bino-like or singlino-like neutralinos, or if neutralinos are very heavy, the neutralino relic density is instead typically much larger than the universal dark matter density.

MSSM models with under-abundant neutralino relic density are phenomenologically perfectly viable: the lightest neutralino can very well not be the only contributor (or it can be a sub-dominant contributor) to the universal dark matter, in a standard cosmological setup. While modified cosmological setups can be concocted to enhance the thermal

relic abundance of neutralinos in those cases (for instance in the presence of non-thermal production [7], or of a faster expansion rate at the epoch of the lightest neutralino freeze-out [8, 9]), MSSM models with *over-abundant* relic neutralinos are, in principle, ruled out. A caveat to this conclusion is the possibility of an episode of entropy injection occurring at temperatures below the decoupling of neutralinos from the universe's thermal bath (entropy injection before freeze-out would not change today's relic abundance of neutralinos).

Ref. [7] gives a thorough discussion of such a class of scenarios for the specific case of an additional scalar field that drives both the entropy dilution and possibly the non-thermal production of neutralinos, as well as a modified cosmological expansion rate if the energy density associated to the scalar field dominates the universal energy budget. Specific examples of setups that can produce a dilution in the relic abundance of neutralinos (or, for that matter, of any other thermal relics decoupled from the thermal bath before entropy injection) include for example models with moduli [10] or Q-ball decays [11], and scenarios with low-temperature or even weak-scale inflation [12, 13, 14]. While a phase transition that plausibly occurred *after* the neutralino freeze-out is the QCD phase transition, lattice simulations [15] clearly indicate that the transition is not strongly first-order (see e.g. the discussion in Ref. [16]).

In the present study, we consider a specific instance of a possible source of dilution for the thermal relic abundance of relic neutralinos from the early universe, namely the electro-weak phase transition (EWPT). In the minimal formulation of the Standard Model Higgs sector, the EWPT is very weakly first-order, or entirely absent, as found e.g. in the non-perturbative analysis of Ref. [17]. However, a strongly first-order phase transition

can occur within the MSSM, or even in very simple extensions of the scalar sector of the Standard Model (for instance via the inclusion of additional singlet scalars [18, 19, 20]). Other possibilities include for instance models with multiple hidden sector scalars coupled only to the Higgs sector (which thus acts as a "portal" to the hidden sector, as envisioned in Ref. [21, 22, 23]). This possibility, which includes scenarios with tree-level conformal invariance where the Higgs mass is generated via dimensional transmutation, has been discussed and studied in detail in Ref. [24] and [25]. A strongly first-order phase transition needs to actually be posited in the context of scenarios where the baryon asymmetry is produced at the EWPT, to prevent the "washout" of the generated baryon number density by sphaleron processes (for a pedagogical introduction to the framework of electro-weak baryogenesis see e.g. Ref. [26]; classic studies on MSSM baryogenesis include [27] and [28]; recent discussions of the phenomenology of electro-weak baryogenesis in the MSSM are given in Ref. [29, 30]). In this case, the order parameter can be considered to be the ratio of the SU(2) Higgs background field $\phi = \sqrt{2}\langle H^0 \rangle$ to the critical temperature for the phase transition, T_c, and a strongly first-order phase transition corresponds to $\phi_c/T_c \gtrsim 1$ [26].

The entropy injection produced in any first-order phase transition can play a relevant role in the thermal history of species that froze out prior to the phase transition, since their relic density will be diluted away by an amount dependent upon the relative entropy injected to the entropy in the species in thermal equilibrium. Interestingly, the CERN Large Hadron Collider (LHC) might potentially inform us on both the details of the scalar electro-weak sector and of the EWPT in particular (including possible non-minimal extensions of the scalar sector [18, 19, 20]), as well as on the mass of a putative dark matter

particle. In some cases, data from the LHC might even enable us to infer, via the knowledge of particle masses and couplings, the thermal relic abundance of a stable neutralino that might be the main dark matter constituent (explicit examples with realistic assumptions on the LHC performance are given in Ref. [31]). A mismatch between the observed cold dark matter abundance and the inferred relic abundance of candidate particles discovered with colliders can have very profound consequences. If the resulting inferred thermal abundance were *larger* than the cold dark matter density, then the answer to the ensuing conundrum might lie in the EWPT and in the Higgs sector, and thus again in physics that can, and will, be tested with the LHC.

The present study is organized as follows: in the next section we describe in detail how a first-order phase transition affects the abundance of a species that froze out prior to the temperature at which the phase transition occurred; the following sec. 2.2 explores the ranges of freeze-out temperatures and of relic abundances relevant to the case of the lightest neutralinos of the MSSM. The ensuing sec. 2.3 describes simple models for the EWPT, and sec. 2.4 describes their impact upon the relic density of MSSM neutralinos. These last two sections present our main results. Finally, sec. 2.5 summarizes and concludes.

2.1 Relic Density Dilution: Thermodynamics

We are concerned here with determining the dilution of a relic species that decoupled (or "froze-out") from the thermal bath in the early universe by entropy injected during a first-order phase transition occurring after the species' freeze-out. The basic thermodynamics of the dilution, which we describe in the present section, is fully general, and does

not depend upon the specifics of the model for the phase transition.

Let $\mathcal{F}(\phi, T)$ be the finite temperature effective potential of the early universe, where ϕ is the order parameter of the phase transition, for instance the vacuum expectation value of the neutral component of the Higgs field. We assume that, for the temperatures under consideration here, there are at most two minima of the potential. At very high temperatures, the potential only has one minimum, at $\phi = 0$. As the temperature drops, a second minimum develops with a corresponding effective potential value larger than that at $\phi = 0$. The value of the potential at the second minimum relative to the first decreases with decreasing temperature so that at $T = 0$ the second minimum is the absolute minimum and there is spontaneous symmetry breaking. We define a "critical temperature" as the temperature $T = T_c$ when the two minima are degenerate. At some temperature $T_* < T_c$, the system transitions from $\phi = 0$ to the new minimum: the tunneling probability from the $\phi = 0$ minimum to the true vacuum is of order unity.

First, let us assume that the transition temperature T_* is very close to the critical temperature T_c so that supercooling is negligible. Here, we follow the discussion of Mégevand and Sánchez [32] (see also [33]). Let s_+ be the entropy density of the high-temperature phase, and let s_- be the entropy density of the low-temperature phase. We may then write the total entropy density as

$$s = s_+ - f\Delta s, \tag{2.1}$$

where $\Delta s = s_+ - s_-$ and f is the volumetric fraction of the system in the low temperature phase. Since the minima are degenerate at T_c, the system is in equilibrium and the total

entropy is conserved. The entropy density then scales as

$$s = s_+ \left(\frac{a_i}{a}\right)^3, \tag{2.2}$$

where a_i is the scale factor of the universe at the beginning of the phase transition. The transition is complete once $f = 1$. Plugging this into Eq. (2.1) and combining with Eq. (2.2), one finds that the total expansion during the phase transition is

$$\left(\frac{a_f}{a_i}\right)^3 = \frac{1}{1 - \Delta s/s_+} = \frac{s_+}{s_-}. \tag{2.3}$$

This is the equation we use to find the dilution in sec. 2.3.2.

Realistically, the system would not be in exact equilibrium—friction and collisions in the walls of bubbles of true vacuum would release entropy, slightly increasing the dilution [34]. This can be quantitatively captured by assessing the variation of the dilution factor with a variation to the temperature at which the phase transition occurs, this variation being driven by the mentioned effects (bubble collisions, friction in the bubble walls etc.). If the entire transition occurs at a temperature an amount ΔT below T_c, then one can show that the change in dilution D is $\Delta D = -3D(D-1)(\Delta T/T_c)$, assuming a radiation dominated energy density.

If $T_* \ll T_c$, then the two phases are not in equilibrium at the beginning of transition and Eq. (2.2) does not hold. Instead, there are three distinct stages to the phase transition: a supercooling stage, a reheating stage, and a phase-coexistence stage. During supercooling, entropy is conserved, so that

$$\frac{s_+(T_*)}{s_+(T_c)} = \left(\frac{a_i}{a_*}\right)^3 \tag{2.4}$$

where a_* is the scale factor at the minimum of supercooling. Assuming that reheating happens quickly relative to the expansion rate, the energy density ρ of the universe does

not change during reheating. The entropy, however, does. If a large enough amount of reheating occurs, the universe will reach a phase coexistence stage at $T = T_c$. Conservation of energy then gives the initial fraction of the universe in the low-temperature phase at the beginning of phase coexistence:

$$\begin{aligned} \rho_+(T_*) &= \rho_+(T_c) - f_0[\rho_+(T_c) - \rho_-(T_c)] \\ &= \rho_+(T_c) - f_0 L \end{aligned} \tag{2.5}$$

$$\rightarrow f_0 = \frac{\rho_+(T_c) - \rho_+(T_*)}{L}, \tag{2.6}$$

where L is the latent heat of the transition at T_c. The entropy density during phase-coexistence is then

$$s = (s_+ - f_0 \Delta s) \left(\frac{a_*}{a}\right)^3. \tag{2.7}$$

Combining this with Eq. (2.1), we have the expansion during phase coexistence

$$\left(\frac{a_f}{a_*}\right)^3 = \frac{1 - f_0 \Delta s/s_+(T_c)}{1 - \Delta s/s_+(T_c)}, \tag{2.8}$$

which gives a total expansion of

$$\left(\frac{a_f}{a_i}\right)^3 = \left(\frac{1 - f_0 \Delta s/s_+(T_c)}{1 - \Delta s/s_+(T_c)}\right) \frac{s_+(T_c)}{s_+(T_*)}. \tag{2.9}$$

We use this equation in sec. 2.3.3 where the transition is strongly first-order.

2.1.1 Determining the transition temperature

We specify here the definition we adopt for the transition temperature T_*, given its relevance in determining the dilution factor for a given effective potential. Shortly after the universe cools below the critical temperature, bubbles of true vacuum nucleate via

thermal tunneling. Most of these are too small to grow—the pressure difference $\Delta p = -\Delta\mathcal{F}$ between the true and false vacuum is not large enough to overcome the surface tension of their walls, so they collapse. Only large bubbles can grow. As the universe further cools, the nucleation rate of larger bubbles increases dramatically. The phase transition begins once the probability to nucleate a supercritical bubble in one Hubble volume is of order 1. Tunneling in cosmological phase transition was originally discussed in the seminal work of Ref. [35, 36, 37] (see also Ref. [33]). For a pedagogical review of cosmological phase transition, see e.g. Kolb and Turner [38].

The tunneling probability per unit time per unit volume goes with temperature roughly as $\Gamma \sim T^4 \exp^{-S_3/T}$, where S_3 is the three-dimensional Euclidean action

$$S_3 = 4\pi \int_0^\infty r^2 dr \left[\frac{1}{2} \left(\frac{d\phi}{dr} \right)^2 + \mathcal{F}(\phi(r), T) \right] \tag{2.10}$$

and where we assume spherical symmetry. The bubble shape $\phi(r)$ comes from the corresponding Euclidean equation of motion

$$\frac{d^2\phi}{dr^2} + \frac{2}{r}\frac{d\phi}{dr} = \frac{\partial}{\partial\phi}\mathcal{F}(\phi, T), \tag{2.11}$$

with the boundary conditions $\lim_{r\to\infty} \phi(r) = 0$ and $\left.\frac{d\phi}{dr}\right|_{r=0} = 0$. Finally, the requirement that one supercritical bubble nucleates per horizon volume in a Hubble time yields a phase transition temperature T_* such that

$$\int_{T_*}^\infty \frac{dT}{T} \left(\frac{2\zeta M_{Pl}}{T} \right)^4 \exp^{-S_3(T)/T} = \mathcal{O}(1), \tag{2.12}$$

where M_{Pl} is the Planck mass, $\zeta = \frac{1}{4\pi}\sqrt{\frac{45}{\pi g}}$, and g is the effective number of relativistic degrees of freedom (see Ref. [26]). For temperatures around the electroweak scale, Eq. (2.12) implies that $S_3/T \sim \mathcal{O}(130\text{–}140)$.

2.2 Salvaging MSSM models with over-abundant relics

In this section we calculate the degree of relic density dilution needed in MSSM models as a function of the temperature at which neutralinos freeze out. This will allow us to immediately determine whether a given MSSM model can or cannot be salvaged by a strongly first-order electro-weak phase transition, the requirement being that the critical temperature of the phase transition be smaller than the freeze-out temperature, and the dilution factor be large enough to bring the neutralino relic density at or below the level of the inferred average dark matter density in the universe.

We work in the context of the R-parity, flavor and CP-conserving MSSM, we enforce that the lightest supersymmetric particle be the lightest neutralino, and parameterize the soft supersymmetry breaking parameters that enter the relevant particle spectrum for the calculation of the neutralino relic abundance with their values at the electro-weak scale (we thus do not assume any grand unified structure for the soft supersymmetry-breaking terms). We do not assume any relationship between the gaugino soft supersymmetry breaking masses, nor about their relative signs, but we assume a common mass scale for all sfermions. Also, for simplicity we set to zero all trilinear scalar coupling with the exception of third generation sfermions. The gluino mass (which does not enter into the calculation of the relic abundance in the DarkSUSY code) was set to $M_3 = 3M_2$, which approximately follows the usual supergravity relation. Details of our scan procedure, including lower and upper limits for the scan as well as whether the sampling was carried out logarithmically or linearly, are given in Table 2.2.

Once a particular MSSM setup is defined by the random parameter values picked

Parameter	Lower Lim.	Upper Lim.	Scan Type
$\|\mu\|$	66 GeV	20 TeV	Log
$\|M_1\|$	40 GeV	20 TeV	Log
$\|M_2\|$	83 GeV	20 TeV	Log
$m_{\tilde{f}}$	$\frac{3}{2}\min(M_1, M_2, \mu)$	20 TeV	Log
$A_{\tilde{f}}$	-3	3	Lin
m_A	200 GeV	20 TeV	Log
$\tan\beta$	2.5	60	Lin

Table 2.1: Ranges for the parameter space scan we employ for our fig. 2.1.

by the procedure outlined above, we require that the resulting particle setup be compatible with updated versions of the limits from collider searches, rare decays and electro-weak precision measurements described in Ref. [39]. We then calculate the thermal relic abundance of the lightest neutralinos, in the context of a standard cosmological setup, with the DarkSUSY package [39].

The two parameters we are interested in for the present study are the thermal neutralino relic abundance, and the temperature at which the neutralino freezes out: a phase transition occurring at temperatures larger than the freeze-out temperature would not affect the relic abundance of neutralinos, since the latter would be in thermal equilibrium after the phase transition and its number density would re-equilibrate to the other thermal species. We define the freeze-out temperature according to the prescription of Ref. [40], that sets it as the temperature where the comoving neutralino number density is a factor 2.5 larger than its asymptotic zero-temperature value.

Fig. 2.1 shows the minimal dilution factor required to bring the thermal neutralino relic abundance below the upper limit set by determinations of the average universal dark matter density, $\Omega_{\rm astro}h^2 \simeq 0.113$ [5] as a function of the neutralino freeze-out temperature.

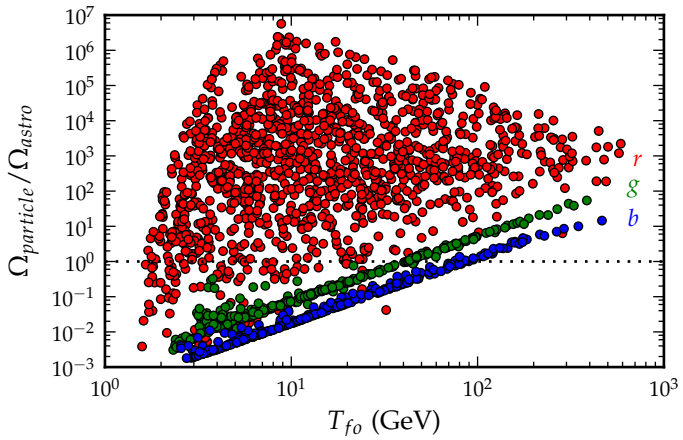

Figure 2.1: A scatter plot of MSSM models on the plane defined by the ratio of the models' thermal neutralino relic abundance ($\Omega_{\rm particle}$) over the universal dark matter density ($\Omega_{\rm astro}$), versus the neutralino freeze-out temperature T_{fo}. Red points correspond to bino-like lightest neutralino, while blue and green points to wino- and higgsino-like lightest neutralinos, respectively. Models above the horizontal line at $\Omega_{\rm particle}/\Omega_{\rm astro} = 1$ are over-abundant, and are ruled out unless a dilution mechanism such as the one we discuss in the present study is operative. See the text for definitions and details.

Loosely, the latter is a factor of 20-25 times smaller than the neutralino mass, which thus increases linearly with the x-axis. We indicate with blue dots models where $M_2 < M_1,\ \mu$, i.e. models corresponding to a dominant wino component in the lightest neutralino mass eigenstate; green dots correspond to models with $\mu < M_1,\ M_2$ (higgsino-dominated lightest neutralinos) and red dots to $M_1 < M_2,\ \mu$ (bino-dominated lightest neutralinos).

Notice that the pair annihilation of bino-like neutralinos proceeds through a variety of channels, including squark and higgs exchanges, which dramatically depend on the details of the spectrum of the relevant particles. This induces a wide scatter in the relic abundance versus mass (or freeze-out temperature) of bino-like models, as evident in fig. 2.1. On the other hand, for dominantly wino- and higgsino-like neutralinos, the dominant annihilation modes always proceed through gauge boson pairs, mediated by chargino (or by the next-to-lightest higgsino in the case of ZZ final state) exchange. In this case, the pair-annihilation

cross section is fixed by gauge couplings and by the mass of the neutralino/chargino system, modulo kinematic threshold effects for neutralino masses near the gauge boson mass (this shows up in fig. 2.1 for $T_{\rm fo} \sim 2-5$ GeV). This is the reason why the wino and the higgsino-like models all fall approximately on a line in the log-log plot of fig. 2.1.

MSSM models whose relic abundance can be salvaged by a strongly first-order electro-weak phase transition therefore feature either higgsino-like lightest neutralinos with masses larger than a TeV, or wino-like neutralinos with masses in excess of 2 TeV, or bino-like neutralinos in a wide mass range, provided the freeze-out temperature is large enough to be above the temperature at which the phase transition occurs. We discuss the possible effects of entropy dilution in the electro-weak phase transition and its impact on the MSSM parameter space in the following section, where we show which regions of fig. 2.1 can potentially be salvaged by the resulting entropy injection.

2.3 Relic Density Dilution and First-Order Phase Transitions

2.3.1 Overview of the Field-Theoretical Setup

We calculate here the dilution of a thermal relic due to a first-order phase transition driven by a scalar field ϕ. Since we are interested in the specific case of the EWPT, as an illustrative instance we consider here the effective potential of the neutral component of the scalar electro-weak sector of the Standard Model ϕ. The extension to the Standard Model we then take into consideration will include an additional set of fermionic and/or bosonic degrees of freedom, which might be thought of as being singlets under the Standard Model

gauge group, but that might transform nontrivially under a hidden sector gauge group, and are coupled to the visible sector only through the Higgs sector [21, 22, 23, 24, 25]. These class of models includes so-called Higgs Portal scenarios, where (partly) secluded hidden sectors communicate with the Standard Model (the "visible" sector) exclusively via interactions in the Higgs sector [22]. Early studies on such models include those listed in Refs. [41, 42, 43, 44, 45, 46, 47], where the Higgs portal was often invoked in the context of identifying a viable particle dark matter candidate. The existence of hidden sectors that might be only partially secluded is ubiquitous to extension to the Standard Model, such as those based on high-rank GUT models, e.g. where the GUT group is E_6 [48], in gauge-mediated supersymmetry breaking setups (for a review, see e.g. [49]) as well as in the landscape of string compactifications [50]. In all of these setups, a potentially large number of (fermionic or bosonic) degrees of freedom, neutral under the Standard Model gauge interactions, might interact with the Higgs sector alone.

At tree-level, the effective potential associated to the field ϕ only we consider here is:

$$V_0(\phi) = -\tfrac{1}{2}\lambda v^2\phi^2 + \tfrac{1}{4}\lambda\phi^4, \tag{2.13}$$

while the zero-temperature one-loop corrections read:

$$V_1(\phi) = \sum_i \pm\frac{g_i}{64\pi^2}\left[m_i^4(\phi)\left(\log\left(\frac{m_i^2(\phi)}{m_i^2(v)}\right) - \frac{3}{2}\right) + 2m_i^2(\phi)m_i^2(v)\right], \tag{2.14}$$

where g_i is the number of degrees of freedom of each particle species in the theory coupled to ϕ, $m_i(\phi)$ is the particle species mass, and the upper and lower signs correspond to bosons and fermions, respectively. We consider only scalar bosons in this paper. Notice that the potential for vector bosons would carry a constant of $\frac{5}{6}$ in place of the $\frac{3}{2}$ in Eq. (2.14) (see

Ref. [24]). Note that both $V_0(\phi)$ and $V_1(\phi)$ have stationary points at $\phi = 0$ and $\phi = v$. These points are respectively local maxima and minima of $V_0(\phi)$. $V_1(\phi)$ has a saddle point at $\phi = v$ and either a maximum or a minimum at $\phi = 0$, depending upon the leading sign.

We obtain the free energy density by adding the finite-temperature one-loop correction

$$\mathcal{F}_1(\phi, T) = \sum_i \frac{g_i T^4}{2\pi^2} I_{\mp}\left[\frac{m_i(\phi)}{T}\right] + \sum_{\text{bosons}} \frac{Tg}{12\pi}\left[m_i(\phi)^3 - [m_i(\phi)^2 + \Pi_i(T)]^{3/2}\right], \qquad (2.15)$$

where I_- and I_+ are for the relevant thermal distribution functions for the bosonic and for the fermionic contributions, respectively:

$$I_{\mp}(x) = \pm \int_0^\infty dy\, y^2 \log\left(1 \mp \exp^{-\sqrt{y^2+x^2}}\right), \qquad (2.16)$$

and where the second summation is for the resummed Daisy diagrams with $\Pi_i(T) = \frac{1}{3}h_i^2 T^2$, where h_i is the Yukawa coupling. Assuming all particles acquire mass through a Higgs-like mechanism in which the mass terms are of the form $m_i(\phi) = h_i\phi$ (i.e. neglecting explicit mass terms for all the additional degrees of freedom interacting with the field ϕ), the free energy density takes the form

$$\begin{aligned}\mathcal{F}(\phi, T) = \lambda(-\tfrac{1}{2}v^2\phi^2 + \tfrac{1}{4}\phi^4) + \sum \pm \frac{g_i h_i^4}{64\pi^2}\left[\phi^4\left(\log\frac{\phi^2}{v^2} - \frac{3}{2}\right) + 2v^2\phi^2\right] \\ + \sum \frac{g_i T^4}{2\pi^2}\left[I_{\mp}\left(\frac{h_i\phi}{T}\right) + \frac{\pi(-1 \mp 1)}{12} D\left(\frac{h_i\phi}{T}, h_i\right)\right] \qquad (2.17)\end{aligned}$$

where $D(x, h) = (x^2 + \frac{1}{3}h^2)^{3/2} - x^3$. For our purposes, we can ignore a constant vacuum energy term. It will also be interesting in our analysis to add a temperature independent cubic term $V_0'(\phi) = \alpha(\frac{1}{2}v^2\phi^2 - \frac{1}{3}v\phi^3)$ with $\alpha \ll \lambda$ to account for example for the possible effects, at the level of the ϕ effective potential, of tree level cubic terms, driven by mixing

with one or multiple gauge singlet scalar fields (see e.g. Ref. [51]). Notice that the purpose of the quadratic term in V_0' is to ensure that the vacuum expectation value is maintained at $\phi = v$ at zero temperature.

In the high-temperature (low-ϕ) limit, Eq. (2.16) can be expanded as

$$\begin{aligned} I_-(x) = &-\frac{\pi^4}{45} + \frac{\pi^2}{12}x^2 - \frac{\pi}{6}x^3 - \frac{x^4}{32}\log\frac{x^2}{a_b} \\ &-2\pi^{7/2}\sum_{l=1}^{\infty}(-1)^l\frac{\zeta(2l+1)}{(l+2)!}\Gamma\left(l+\tfrac{1}{2}\right)\left(\frac{x}{2\pi}\right)^{2l+4}, \text{ and} \end{aligned} \tag{2.18}$$

$$\begin{aligned} I_+(x) = &-\frac{7\pi^4}{360} + \frac{\pi^2}{24}x^2 + \frac{x^4}{32}\log\frac{x^2}{a_f} \\ &+\tfrac{1}{4}\pi^{7/2}\sum_{l=1}^{\infty}(-1)^l\frac{\zeta(2l+1)}{(l+2)!}\left(1-\frac{1}{2^{2l+1}}\right)\Gamma\left(l+\tfrac{1}{2}\right)\left(\frac{x}{\pi}\right)^{2l+4}, \end{aligned} \tag{2.19}$$

(see e.g. the seminal work of Ref. [33]; see also [32]) where $\log a_b = \frac{3}{2} - 2\gamma + 2\log(4\pi)$, $\log a_f = \frac{3}{2} - 2\gamma + 2\log\pi$, γ is the Euler constant, ζ is the Riemann zeta function, and Γ is the Gamma function.

In the low-temperature (high-ϕ) limit, the expansions are given by

$$I_\mp(x) = -x^2\sum_{k=1}^{\infty}\frac{(\pm 1)^{k+1}}{k^2}K_2(kx), \tag{2.20}$$

(again, see e.g. Ref. [33] and [32]) where K_2 is the modified Bessel function of the second kind of order 2.

There are a few important things to note about these expansions. The original integrals in Eq. (2.16) are negative monotonically increasing functions with $\lim_{x\to\infty} I_\pm(x) = 0$. They are similar in shape to upside-down bell-curves (see Fig. 2.2). The low-temperature expansions have this same character for any finite number of terms. If we keep only terms up to $k = 8$ (as we do for the numerical study we present in this analysis), the errors at $x = 0$ are only 0.01% and 0.05% for I_+ and I_-, respectively. The errors drop exponentially

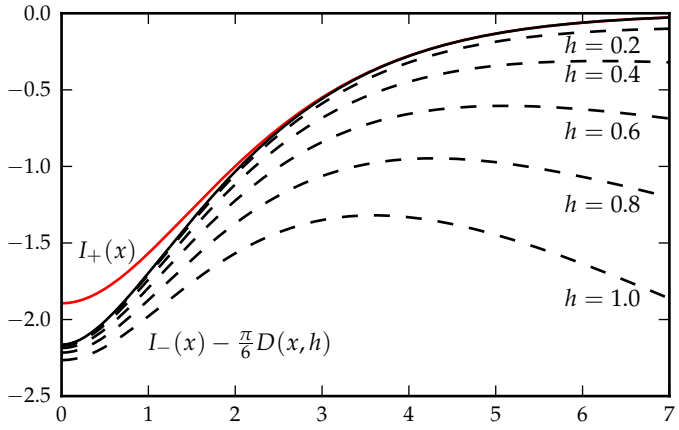

Figure 2.2: The integrals of Eq. (2.16). Bosons correspond to $I_-(x)$ (black line), and fermions correspond to $I_+(x)$ (red line). The dashed lines show the resummed Daisy diagram contributions for h =0.2, 0.4, 0.6, 0.8, and 1.0.

for $x > 0$, with fractional errors of $\sim 10^{-10}$ at $x = 2$. In contrast, the high-temperature expansion diverges towards $\pm\infty$ for a finite number of terms. For example, retaining even up to $l = 15$ produces a visible divergence in $I_+(x)$ towards negative infinity at $x = 3.5$. The benefit of the high-temperature expansions is that they contain an explicit cubic term, whereas the low-temperature expansions do not. If the phase transition is weakly first-order so that terms of order x^5 can be ignored, then the cubic term is necessary to avoid a continuous phase transition. Therefore, the low-temperature expansions underestimate the strength of the transition when the transition is weak.

As argued in Ref. [25], higher-order corrections to the potential are subdominant and can be safely neglected. In particular, Ref. [25], which adopts a setup very similar to ours, finds that two-loop effects, as caluclated e.g. in [52], do not affect significantly the structure of the effective potential. We thus neglect them here.

2.3.2 Semi-Analytical Results in the High-Temperature Limit

If the phase transition is weakly first-order, we may use a temperature-dependent quartic potential as an approximation to the free energy:

$$\mathcal{F}(\phi, T) = D(T^2 - T_0^2)\phi^2 + (\tfrac{1}{3}\alpha v - ET)\phi^3 + \tfrac{1}{4}\lambda\phi^4 - \frac{\pi^2}{90} g_l T^4. \tag{2.21}$$

The constants D, E, and T_0 come directly from the coefficients of Eq. (2.17) and Eqs. (2.18-2.19), and $g_l = g_b + \frac{7}{8} g_f$ are the effective number of degrees of freedom of particle species. For this analysis we assume that D is positive, which does not necessarily follow from Eq. (2.17).

It is much more simple to analyze this equation if we recast it in the dimensionless form

$$\tilde{\mathcal{F}}(\varphi, \tau) = D(\tau^2 - 1)\varphi^2 + E(x - \tau)\varphi^3 + \tfrac{1}{4}\lambda\varphi^4 - \frac{\pi^2}{90} g_l \tau^4, \tag{2.22}$$

where $\tilde{\mathcal{F}} = \mathcal{F}/T_0^4$, $\varphi = \phi/T_0$, $\tau = T/T_0$, and $x = \frac{1}{3}\alpha v/ET_0$. The critical temperature (the temperature of degenerate minima), is then easy to find analytically:

$$\tau_c = \frac{-x \pm \sqrt{y\,[y - (1 - x^2)]}}{y - 1}, \tag{2.23}$$

where $y = D\lambda/E^2$. In all situations, the solution corresponding to the positive root is the correct physical solution, while the negative root is an unphysical solution resulting from the use of an approximate potential. Note that if $x > 1$ then by Eq. (2.23) $x > \tau_c$ and the second minimum is at $\varphi < 0$ at $\tau = \tau_c$. Since the temperature-dependent terms in Eq. (2.17) are even in ϕ while those in Eq. (2.21) are not, we reject all solutions with $\phi < 0$ and demand that $x < 1$.

If the transition temperature is close to the critical temperature, as we expect for a weakly first-order phase transition, then Eq. (2.3) gives the correct amount of dilution. The entropy density is $s = -d\mathcal{F}/dT \to s/T_0^3 = -d\tilde{\mathcal{F}}/d\tau$. In the high-temperature phase at the critical temperature, we have $s_+/T_0^3 = \frac{2\pi^2}{45} g_l \tau_c^3$. In the low temperature phase, the minimum is $\varphi_c = 2E(\tau_c - x)/\lambda$ and the entropy difference is $\Delta s/T_0^3 = \varphi_c^2(2D\tau_c - E\varphi_c)$. Plugging in values, we get

$$\frac{\Delta s}{s_+} = \frac{45}{2g_l\pi^2}\frac{8E^4}{\lambda^3}\left(y - \frac{y - x\sqrt{(x^2+y-1)y}}{x^2+y}\right)\left(\frac{y - x\sqrt{(x^2+y-1)y}}{x^2+y}\right)^2, \tag{2.24}$$

which simplifies to

$$\frac{\Delta s}{s_+} \approx \frac{45}{2g_l\pi^2}\frac{8DE^2}{\lambda^2}, \tag{2.25}$$

in the limit that $y \gg x, 1$. Note that the cubic term does not have a noticeable effect upon the dilution until it becomes quite large, which would violate our original assumptions.

In passing, we remark that, taking the above analysis at face value, in the Standard Model, where the top quark and the W and Z bosons are the only relevant degrees of freedom (see Ref. [26]), and $D = 0.16$, $E = 0.0096$, $y \sim 300$ (dependent upon the Higgs mass), and $g_l = 106.75$, one finds a negligible dilution factor, namely:

$$\left(\frac{a_f}{a_i}\right)^3 = \frac{s_+}{s_-} \approx 1 + \frac{\Delta s}{s_+} = 1 + \frac{45}{2g_l\pi^2}\frac{8DE^2}{\lambda^2} \approx 1.0001. \tag{2.26}$$

Interestingly, the semi-analytic setup outlined above also allows us to get an estimate of the dilution factor expected in the context of the minimal supersymmetric extension of the Standard Model with light scalar tops (see e.g. Ref. [27, 28, 30]), which has often been considered in the context of electro-weak baryogenesis. In that case, the cubic term E can be one order of magnitude larger than in the Standard Model, implying a dilution

factor of at most 1.01. According to our equation (2.25) this means that in the MSSM the dilution to the relic density of species freezing out prior to the electro-weak phase transition is a small effect (at most a few percent).

2.3.3 Strongly First-order Phase Transitions: Numerical Solutions

If the phase transition is strongly first-order, Eq. (2.21) does not hold and we must instead resort to the full expression for the free energy density with the low-temperature expansion of Eq. (2.16). One must compute the dilution factor fully numerically.

In our models, we proceed with the following steps. First, we obtain a function of the minimum of the true vacuum $\phi_0(T)$ up to the critical temperature by numerically solving the differential equation

$$\frac{d\phi_0}{dT} = -\left(\frac{\partial^2 \mathcal{F}}{\partial\phi\partial T}\right) \Big/ \left(\frac{\partial^2 \mathcal{F}}{\partial\phi^2}\right) \tag{2.27}$$

with the initial condition $\phi_0(T=0) = v$. We then calculate the transition temperature T_* by calculating the Euclidean action at many temperatures and searching for $S_3/T \sim \mathcal{O}(130\text{–}140)$. To account for a potentially wide range of transition temperatures and relativistic degrees of freedom, we use $S_3(T_*)/T_* = 170 - 5\log(T/1\text{ GeV}) - 2\log(g)$. We then calculate the dilution factor directly from Eq. (2.9) using $s = -d\mathcal{F}/dT$.

For definiteness, we consider two classes of models: one with only additional scalar bosonic degrees of freedom, and one with an equal number of additional bosonic and fermionic contributions. An explicit realization of the former case is given by the multiple hidden sector scalars S_i discussed in Ref. [24, 25], where the coupling between the hidden and the visible sector occurs only through renormalizable terms in the potential

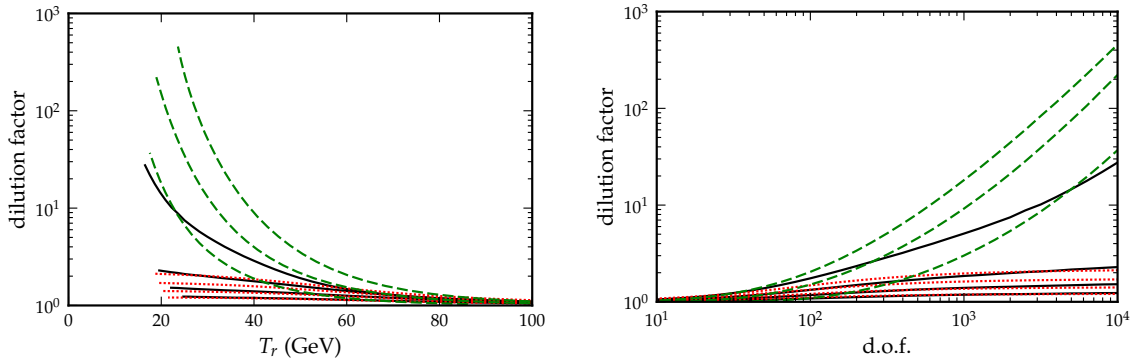

Figure 2.3: Dilution factors for boson-fermion models (dotted red and dashed green) and purely bosonic models (solid black) as functions of the temperature at the end of reheating (left) and the number of fermion and boson degrees of freedom (right). For the purely bosonic models, the highest line corresponds to the highest Yukawa coupling for which the point at $\phi = 0$ is a minimum at zero temperature. The three lower lines have 0.7, 0.8 and 0.9 times this value. For boson-fermion models, the four dotted red lines correspond to Yukawa couplings identical to those in the bosonic cases, while the dashed green lines corresond to Yukawa couplings of 0.5, 0.75, and 1.0.

proportional to $H^\dagger H S_i^2$. The latter, instead, alludes to a supersymmetric particle content for the additional degrees of freedom; one possible example is an extension to multiple extra generations of fermion-sfermions along the lines of the analysis of Ref. [53], that discusses the impact on the EWPT of a supersymmetric model with four chiral matter generations.

For the ease of analysis, all massive particles in a given model have the same Yukawa coupling so that we effectively have only one (or two) massive particle species with a potentially large number of degrees of freedom. In each case, the degrees of freedom per fermion and/or boson range from 10 to 10,000. We additionally add massless bosons (i.e., $h = 0$) with $g_l = 100$ degrees of freedom, which approximates the number of relativistic degrees of freedom in the standard model. That is, we have a variable number of degrees of freedom for massive particles, but keep the number of massless particles constant. The latter just adds the ϕ-independent term $-\pi^2 g_l T^4/90$ to the free energy of Eq. (2.17), and

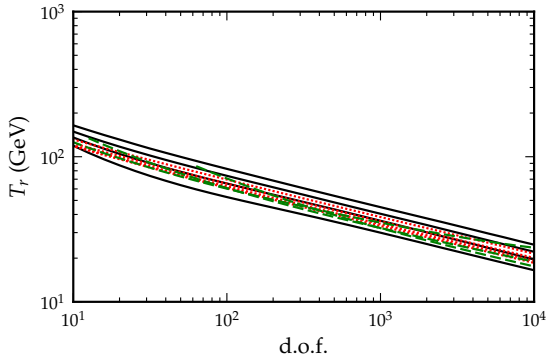

Figure 2.4: Reheating temperature as a function of fermion and boson degrees of freedom. Lines correspond to the same models as in Fig. 2.3, with higher Yukawa couplings resulting in lower reheating temperatures.

gives an additional suppression to the factor ζ of Eq. (2.12). Note that the addition of massless particles does not change the phase transition temperature or dynamics. It does, however, add entropy to both the high and low-temperature phases, which decreases the overall dilution factor via Eq. 2.9. In the boson-only models, large couplings turn the point at $\phi = 0$ into a maximum at zero temperature via the quadratic term in Eq. (2.14). We limit ourselves to the maximum couplings for which this is not the case. In all cases, we set the zero-temperature Higgs mass to be $m_h = 150$ GeV.

Figures 2.3 and 2.4 display our results. The black lines correspond to models without any fermion contribution and variable Yukawa couplings. The models in the highest of these lines have the maximal couplings for which the point at $\phi = 0$, $T = 0$ is a maximum, while the lower lines have 0.9, 0.8, and 0.7 times the maximum couplings. The dotted red and dashed green lines correspond to models with equal fermion and boson contributions. The dotted red lines have the same couplings as the solid black lines, while the dashed green lines have fixed couplings of 0.5, 0.75, and 1.0. For boson-fermion models with reasonably large Yukawa couplings and many degrees of freedom, one can achieve dilution factors on

the order of 100. Purely bosonic models, on the other hand, can only reach dilution factors on the order of 10. The largest aspect contributing to this discrepancy is the range of Yukawa couplings available to the different cases. At $g = 10{,}000$, the maximum coupling for bosons is only $h_b = 0.23$, while the highest plotted dilution factor for a boson-fermion model has $h_b = h_f = 1.0$. When purely bosonic and boson-fermion models have identical couplings, the bosonic models tend to have slightly higher dilution factors.

One can easily explain two of the important qualitative features of Figs. 2.3 and 2.4 by examining the free energy of Eq. (2.17). First, the temperature of the phase transition tends to decrease with increasing degrees of freedom. The temperature-dependent term in the free energy has a coefficient of gT^4. When this term is large, the second minimum of the potential disappears and the origin becomes the true vacuum. Thus, we expect the temperature of the transition to scale as $T \propto g^{-1/4}$, as seen in Fig. 2.4. Second, the dilution factor tends to increase with increasing Yukawa couplings and decreasing temperature scales. If either h is large or T is small, then the temperature-dependent term is nearly zero except for small ϕ, excluding resummed Daisy terms (see Fig. 2.2 for the behavior of $I_{\pm}(x)$). Therefore, the entropy $s = -d\mathcal{F}/dT$ is much smaller in the true vacuum than it is at the origin. Including the Daisy terms, the negative slope of $I_{-}(x) - \frac{\pi}{6}D(x,h)$ tends to decrease the entropy at high ϕ. If the transition reaches a phase coexistence stage, then the small entropy leads directly to a high dilution factor via Eq. (2.3). This effect dominates when $h\phi/T \approx hv/T \gtrsim 5$, which is the case for the boson-fermion models in Fig. 2.3 with $h \geq 0.5$ (dashed green lines).

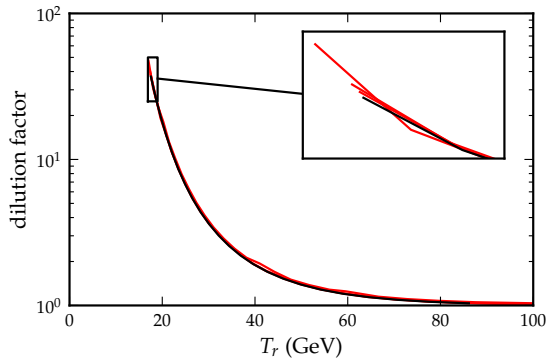

Figure 2.5: Dilution factors for models with cubic terms (red lines) added to the boson-fermion models in Fig. 2.3 with Yukawa couplings of $h = 0.5$ (black line). The red lines have cubic strengths of $\alpha/\lambda = 0.05$, 0.15, and 0.50.

2.3.4 Models with Tree-Level Cubic Terms

We also examine what happens when we add a tree-level cubic term $V_0'(\phi) = \alpha(\frac{1}{2}v^2\phi^2 - \frac{1}{3}v\phi^3)$ to the free energy. Fig. 2.5 shows cubic terms added to boson-fermion models with Yukawa couplings fixed at $h_f = h_b = 0.5$. The models are otherwise exactly the same as those in the previous section: $g_l = 100$, $m_h = 150$ GeV, and the boson/fermion degrees of freedom $g_f = g_b$ range from 10 (corresponding to the lower-right portion of Fig. 2.5) to 10,000. The black line has no added cubic term, while the red lines have cubic strengths of $\alpha/\lambda = 0.05$, 0.15, and 0.50. Even large terms with $\alpha = \frac{1}{2}\lambda$ do not seem to significantly impact the dilution factor. The effects of cubic terms upon purely bosonic models and models with smaller Yukawa couplings are qualitatively similar.

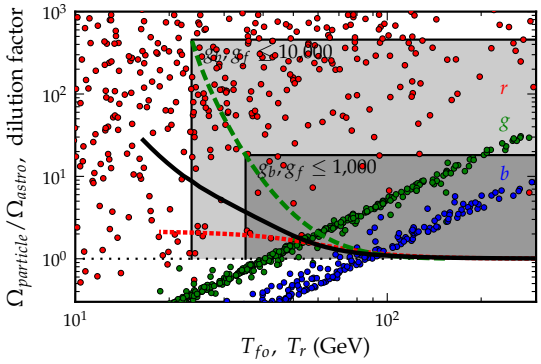

Figure 2.6: An overlay of dilution factors for boson and boson-fermion models on top of a scatter plot of dark matter abundance in different MSSM models. The points are the same as those in Fig. 2.1. The green, black, and red lines correspond to the highest green, black, and red lines of Fig. 2.3. The two boxes show which MSSM models are viable for dilution models with $h_f = h_b = 1.0$ and $g_b, g_f \leq$ 10,000 and 1,000.

2.4 Supersymmetric Dark Matter and a Strongly First-Order Phase Transition

We determine here which MSSM models with neutralino dark matter might not overproduce dark matter given a strongly first-order phase transition. Figure 2.6 shows an overlay of the dilution from different models of phase transitions on top of our scan of the dark matter abundance in MSSM models. Red, green and blue points correspond to bino, higgsino, and wino-like models, while the solid black, dotted red, and dashed green lines correspond to phase transition models with only bosons at their maximal Yukawa couplings, bosons and fermions at the same Yukawa couplings, and bosons and fermions with fixed Yukawa couplings of $h_f = h_b = 1.0$. These are the same as the highest of the black, red and green lines in Fig. 2.3.

The freeze-out temperature of the dark matter must be larger than the final re-heating temperature of the phase transition if the transition is to have an effect upon dark

matter abundance. Therefore, any point that lies to the right of any of the three lines can be diluted to the cosmic relic abundance by a sufficiently strong phase transition. If a point lies between the lines, then one can easily pick a phase transition model that produces the correct amount of dilution. Note that only MSSM models with an overabundance of dark matter are problematic—if a given phase transition model over-dilutes a given MSSM model of dark matter, then the two models can still be mutually viable if the neutralino dark matter does not constitute the entire universal dark matter abundance.

The two boxes in Fig. 2.6 show which MSSM models are viable given the most optimistic phase transition models (that is, boson-fermion models with $h_f = h_b = 1.0$) with degrees of freedom $g_f = g_b =$ 1,000 (inner box) and 10,000 (outer box). With 1,000 d.o.f., almost all of the over-abundant higgsino and wino-like models are viable. With 10,000 d.o.f., a handful of bino-like models become viable as well. However, there are no viable models with freeze-out temperatures less than ~ 20 GeV or overabundances greater than a factor of ~ 200 unless they are accompanied by phase transitions with very large ($> 10{,}000$) particle degrees of freedom. This includes most of the bino-like models and a small subset of the low-mass higgsino-like models.

2.5 Summary

A strongly first-order electro-weak phase transition, warranted in the context of scenarios for the production of the observed baryon asymmetry at the electro-weak scale, can lead to a significant dilution of the thermal relic abundance of the lightest supersymmetric particle, if the latter is stable. In this paper we studied the impact of toy models for the

electro-weak sector on the relic abundance of MSSM neutralinos. Specifically, we considered the effect on the electro-weak sector of adding a large number of bosonic or bosonic-plus-fermionic degrees of freedom, which affects both the one-loop temperature-independent and the temperature-dependent contribution to the effective potential of the Higgs field. We noted that for neutralino freeze-out temperatures between 20-40 GeV, corresponding to neutralino masses at or above 400 GeV, the dilution due to the entropy injected in the first-order electro-weak phase transition can be as large as 10–100 if we postulate a large number of extra degrees of freedom ($10^3 - -10^4$). Numerous MSSM models exist that could be viable if such a dilution effect is in fact operative. For models with a more modest number of additional d.o.f. (say, of the same order of the Standard Model d.o.f.), the dilution can still be on the order of 2. We find that a cubic term in the effective potential has a comparatively small effect upon the relic abundance of species. Also, we showed that the dilution expected in the context of the MSSM without additional degrees of freedom coupled to the Higgs sector is a very small effect, at most at the few-percent level.

Should future data from the LHC point towards a neutralino relic abundance larger than the cosmological dark matter density, the origin of the mis-match might lie in the same electro-weak scale physics that the LHC itself will concurrently explore. Interestingly, this can be profoundly intertwined with the question of the origin of the matter-antimatter asymmetry in the early universe, opening up the possibility that electro-weak physics lie at the core of both dark and visible matter, and that the LHC will soon shed light and perhaps unveil this scenario.

Chapter 3

Computing Cosmological Phase Transition Temperatures and Bubble Profiles with Multiple Fields

Phase transitions driven by scalar fields likely played an important role in the very early evolution of the Universe. In most inflationary models, the dynamics are driven by the evolution of a scalar inflaton field, while at later times electroweak symmetry breaking is thought to be driven by a transition in the Higgs field vacuum expectation value. Electroweak scale physics is currently being probed by the LHC, so the phenomenology of the electroweak phase transition is of particular interest. A strongly first-order electroweak phase transition would have been a source of entropy production in the early Universe (thereby changing the evolution of its scale with respect to temperature) and produced a stochastic background of gravitational radiation[54], perhaps observable by future space-based gravitational radiation observatories[55]. In addition, a strongly first-order electroweak phase transition may have satisfied the Sakharov conditions[56] and been responsible for the current baryon asymmetry of the universe (for recent studies see e.g. Refs. [57, 58, 59, 30, 60, 61, 62, 63, 19, 64, 65, 66, 67, 68, 69]), or may have affected the relic density of (for example) dark matter particles [70, 71, 72].

In the standard model, the electroweak phase transition is not strongly first-order unless the Higgs mass is below ~ 70 GeV[73, 74, 75], which is excluded by the current LEP bound of 114.4 GeV[76]. However, electroweak baryogensis can be saved in extensions to the standard model, many of which include extra dynamic scalar fields (such as two-Higgs-doublet models [77, 78, 79, 80, 81, 82, 83]). The amount of produced baryon asymmetry depends crucially upon the dynamics of the phase transition, and particularly upon the bubble-wall profiles that separate the high- and low-temperature phases. These profiles are fairly easy to calculate using effective field theory if there is only one scalar field, but

multiple fields greatly increase the computational complexity.

In this paper, I present an easy-to-use numerical package (CosmoTransitions) to analyze phase transitions in finite temperature field theory with multiple scalar fields. The program consists of three basic parts (see fig. 3.1): modules for finding the tunneling solution (bubble wall profile) between different vacua, a module for finding critical temperatures and phase transitions, and an abstract class to define specific field-theoretic models and their effective potentials. In section 3.1, I describe the algorithms for finding bubble wall profiles for both single and multiple fields. Section 3.2 describes the algorithm for finding phase transitions, while section 3.3 describes how one can implement a specific model in a simple program. Finally, I present numerical results in section 3.4 and conclude in section 3.5.

To download the latest version of CosmoTransitions, visit `http://chasm.ucsc.edu/cosmotransitions`.

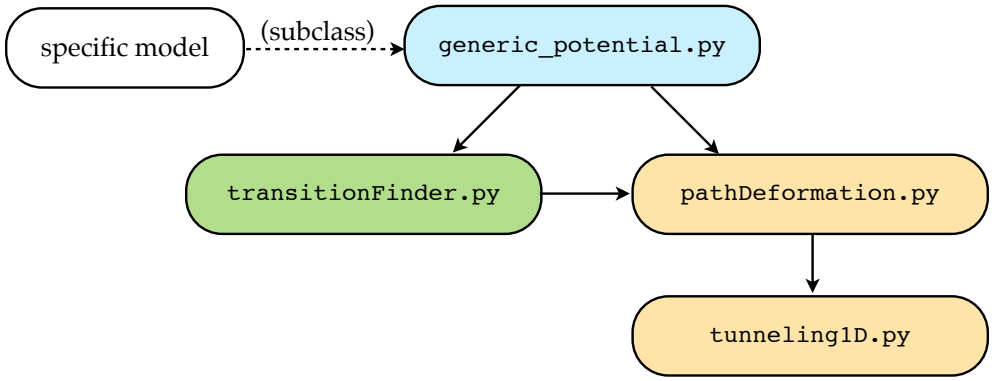

Figure 3.1: Overview of the CosmoTransitions package file structure. The files `pathDeformation.py` and `tunneling1D.py` find critical bubble profiles, `transitionFinder.py` finds the minima of finite temperature potentials as a function of temperature and analyzes phase transitions, and `generic_potential.py` defines an abstract class that can easily be subclassed to examine a specific model.

3.1 Calculating bubble profiles

First-order cosmological phase transitions proceed by the nucleation of bubbles of true vacuum out of metastable false vacuum states. The bubbles have both surface tension and internal pressure, so that large bubbles tend to expand and small bubbles tend to collapse. Critical bubbles—bubbles that are just large enough to avoid collapse—will drive the phase transition.

Given a Lagrangian

$$\mathcal{L} = \frac{1}{2}(\partial_\mu \vec{\phi})(\partial^\mu \vec{\phi}) - V(\vec{\phi}), \tag{3.1}$$

where $\vec{\phi}$ is a vector of scalar fields, a critical bubble can be found by extremizing the Euclidean action

$$S_E = \int d^d x \left[\frac{1}{2}\left(\partial_\mu \vec{\phi}\right)^2 + V(\vec{\phi})\right], \tag{3.2}$$

where $d = 4$ (3) for tunneling at zero (finite) temperature. This quantity is critical for finding the nucleation rate, and thereby determining the phase transition temperature and whether or not the transition actually happens (see Refs. [35, 36, 37] for seminal work on phase transitions in quantum field theory). The bubble nucleation rate per unit volume is $\Gamma/V = Ae^{-S_E}$ at zero temperature and $\Gamma/V = Ae^{-S_E/T}$ at finite temperature. The prefactor A is quite difficult to calculate, but it has only weak temperature dependence and can generally be estimated on dimensional grounds (see, e.g., Ref. [26]). By requiring that the expectation value for one bubble to nucleate per Hubble volume is $\sim \mathcal{O}(1)$, one can show that the bubble nucleation temperature for weak-scale fields is given by $S_E/T \sim 140$.

Assuming spherical symmetry, the bubble's equations of motion are

$$\frac{d^2\vec{\phi}}{d\rho^2} + \frac{\alpha}{\rho}\frac{d\vec{\phi}}{d\rho} = \nabla V(\vec{\phi}). \tag{3.3}$$

At finite temperature, ρ is simply the spatial radial coordinate and $\alpha = 2$. At zero temperature, $\rho^2 = r^2 - t^2$ and $\alpha = 3$. The program defaults to $\alpha = 2$, but this can be overridden when using either `pathDeformation.py` or `tunneling1D.py` directly, ignoring the temperature-dependent routines in `transitionFinder.py`. Let $\vec{\phi}_T$ and $\vec{\phi}_F$ denote the true and false vacua, respectively. Then in order for the solution to match the field at infinity, we require that $\vec{\phi}(\infty) = \vec{\phi}_F$. We also demand that $\left.\frac{d\vec{\phi}}{dr}\right|_{\rho=0} = 0$ so that the bubble is non-singular at the origin.

Note that this procedure is limited by the validity of perturbation theory and of the effective potential. Ideally, once all model parameters are set, one should perform a lattice Monte-Carlo simulation to compute the nucleation rate and bubble profile as accurately as possible [84, 85]. However, this is often computationally impractical.

3.1.1 One-dimensional solution

When the field has only one dimension, the solution to the critical bubble profile can easily be solved by the overshoot/undershoot method (see, e.g., Ref. [86]). Here, it is easiest to think of the problem as that of a classical particle moving under the influence of the inverted potential $-V(\phi)$ plus a peculiar looking friction term, where ϕ takes on the role of a spatial coordinate and ρ acts as the time coordinate. The problem then is to find the initial placement of the particle near ϕ_T such that it rolls down the potential and comes to a stop at ϕ_F when $\rho = \infty$ (see figure 3.2). If the particle rolls past (overshoots) ϕ_F, then

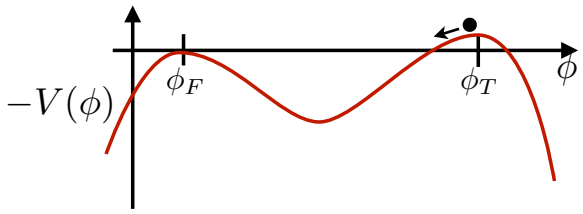

Figure 3.2: The equations of motion for a field with a potential $V(\phi)$ can be thought of as the equations for a particle moving in an inverted potential $-V(\phi)$.

the initial placement was too close to ϕ_T. If it doesn't have enough energy to make it to ϕ_F (an undershoot), then the initial placement needs to be closer to $\vec{\phi}_T$. Through trial and error, one can find the initial placement to arbitrary precision.

The code presented with this paper follows the general overshoot/undershoot method, implemented by the class `tunneling1D.bubbleProfile`. Calculation of thick-walled bubbles is straightforward, but thin-walled bubbles require extra consideration. In thin-walled bubbles, the transition from $\phi \approx \phi_T$ to $\phi \approx \phi_F$ happens over a distance much shorter than the bubble's overall size. In the particle analogy, the particle sits very close to ϕ_T for a very long time before quickly rolling down the potential and stopping at ϕ_F. Extreme accuracy in $\phi_0 = \phi(\rho = 0)$ would be needed to reliably calculate the wall profile, since a small change in ϕ_0 would lead to a large change in the radius of the bubble. Instead, I define a new variable x such that $\phi_0 = \phi_T + e^{-x}(\phi_F - \phi_T)$, and use it as the initial condition to vary instead.

For small ρ and $\phi \approx \phi_T$, the equation of motion can be approximated as

$$\frac{d^2\phi}{d\rho^2} + \frac{\alpha}{\rho}\frac{d\phi}{d\rho} = \left.\frac{d^2V}{d\phi^2}\right|_{\phi=\phi_T} (\phi - \phi_T) \tag{3.4}$$

which has the exact solution

$$\phi(\rho) - \phi_T = C\rho^{-\nu} I_\nu \left(\rho\sqrt{b}\right) \tag{3.5}$$

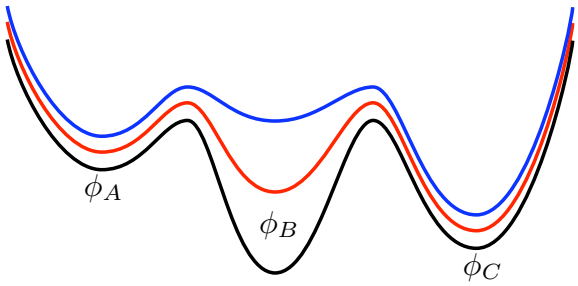

Figure 3.3: A problematic potential with more than two minima. A tunneling solution from ϕ_A to ϕ_C is only guaranteed to exist for the topmost potential (blue line).

where $\nu = \frac{\alpha-1}{2}$, $b = \left.\frac{d^2V}{d\phi^2}\right|_{\phi=\phi_T}$, and I_ν is the modified Bessel function of the first kind. For $\alpha = 2$, this simplifies to $\phi(\rho) - \phi_T \propto \frac{1}{\rho}\sinh(\rho\sqrt{b})$. These can be numerically inverted to find $\rho(\phi)$, which allows one to calculate the approximate radius of a thin-walled bubble without performing any integration. The integration can then start at the edge of the bubble wall, which both increases accuracy and decreases computation time.

The overshoot/undershoot implementation is fairly robust, but there are situations in which it either does not work or is unreliable. Consider the potentials shown in figure 3.3. They each have three minima $\phi_A < \phi_B < \phi_C$, with $V(\phi_A) > V(\phi_C)$. If one tries to calculate the bubble profile for tunneling from ϕ_A to ϕ_C, only the topmost potential is unproblematic. There, there will be a solution where the field starts near ϕ_C, rolls over the bump at ϕ_B, and ends up at ϕ_A. In the bottommost potential, no such solution exists. The minimum at ϕ_B is the true vacuum of the theory, so the field will tunnel from ϕ_A to ϕ_B, ignoring ϕ_C completely. The overshoot/undershoot method will return this solution (any initial $\phi_0 > \phi_B$ will register as an undershoot), but it won't perform any optimization for thin-walled bubbles and may have poor accuracy. In the middle case, with $V(\phi_A) > V(\phi_B) > V(\phi_C)$, there may or may not be a direct tunneling solution from ϕ_A to ϕ_C. Using the particle analogy, it could be

that any particle that starts near ϕ_C and has enough momentum to get beyond ϕ_B will necessarily overshoot ϕ_A. In this case, the field can only tunnel to ϕ_C in two steps: first by tunneling to ϕ_B, and then by tunneling to ϕ_C in a separate nucleation event. The algorithm in `tunneling1D.bubbleProfile` will only ever return the first of these transitions, and it may have poor accuracy.

3.1.2 Multi-dimensional solution and path deformation

With the solution to the one-dimensional problem in hand, we are ready to tackle the more challenging problem with multiple field dimensions. The overshoot/undershoot method no longer works because we required the unique topology of the one-dimensional case to determine whether a particular solution overshot or undershot the boundary condition at $\rho = \infty$. Instead, I propose a method of path deformation.

First, assume as an initial guess that the tunneling occurs on some fixed path in field space. That is, $\vec{\phi}_{guess} = \vec{\phi}(x)$, where x parametrizes the path and for simplicity we require that $\left|\frac{d\vec{\phi}}{dx}\right| = 1$. The equations of motion split into two parts—one parallel and one perpendicular to the path:

$$\frac{d^2x}{d\rho^2} + \frac{\alpha}{\rho}\frac{dx}{d\rho} = \frac{\partial}{\partial x}V[\vec{\phi}(x)] \tag{3.6}$$

$$\frac{d^2\vec{\phi}}{dx^2}\left(\frac{dx}{d\rho}\right)^2 = \nabla_\perp V(\vec{\phi}), \tag{3.7}$$

where $\nabla_\perp V$ represents the components of the gradient of V that are perpendicular to the path. Equation 3.6 is the same as the one-dimensional equation of motion, which we can solve by the overshoot/undershoot method. If the path guess $\vec{\phi}(x)$ is correct, then the solution to equation 3.6 will also solve equation 3.7. The trick then is to find the

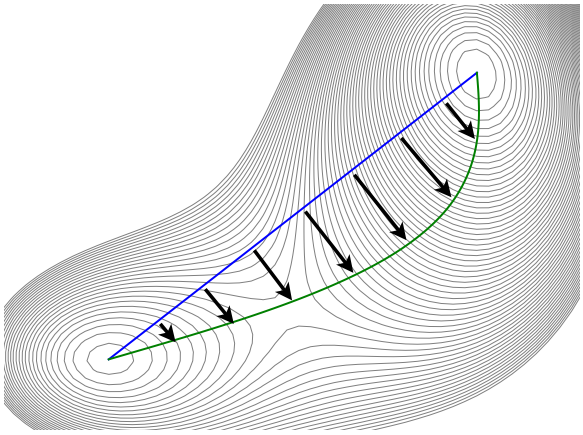

Figure 3.4: Path deformation in two field dimensions. The normal force exerted on the starting path (blue straight line) pushes it in the direction of the true tunneling solution (green curved line).

right path. A similar approach of path deformation has been proposed by Ref. [87], while Refs. [88, 89, 90] use alternate methods to solve the equations of motion. I have previously employed the basic algorithm described below in the context of zero-temperature phase temperatures and singlet scalar dark matter models [91].

Using the particle analogy, we can think of the path guess as a fixed track on which the particle moves through the multi-dimensional space. Equation 3.6 describes the forces parallel to the track and thus determine the particle's speed. Equation 3.7 does not effect the motion of the particle, but instead determines the normal force N that the track must exert on the particle to keep it from falling off: $N = \frac{d^2\vec{\phi}}{dx^2}\left(\frac{dx}{d\rho}\right)^2 - \nabla_\perp V(\vec{\phi})$. For the right path, $N = 0$. Given a starting guess, one can deform the path to the correct solution by continually pushing it in the direction of N (see figure 3.4).

I implement this general method in the CosmoTransitions package using B-splines in the module `pathDeformation.py`. Each path is written as a linear combination of spline basis functions plus a linear component connecting its ends: $\vec{\phi}(y) = \sum_i \beta_i \vec{\phi}_i(y) + (\vec{\phi}_0 -$

$\vec{\phi}_F)y + \vec{\phi}_F$, where y parametrizes the path ($0 \leq y \leq 1$, and generally $\left|\frac{d\vec{\phi}}{dy}\right| \neq 1$), β_i are the spline coefficients, $\vec{\phi}_i(y)$ are the basis functions, and $\vec{\phi}_i(0) = \vec{\phi}_i(1) = 0$. This fixes the path's endpoints at $\vec{\phi}_0 \sim \vec{\phi}(\rho{=}0)$ and $\vec{\phi}_F$. Generally, only a small number of basis functions is needed to accurately model the path (~ 10 per field direction) unless it contains sharp bends or many different curves.

Before any deformation, the algorithm first calculates the bubble profile along the starting path using the overshoot/undershoot method. Then it deforms the path in a series of steps without recalculating either the one-dimensional profile or $\left|\frac{d\vec{\phi}}{d\rho}\right|$. At each step it calculates the normal force for a relatively large number of points (~ 100) along the path, rescales the normal force by $|\vec{\phi}_T - \vec{\phi}_F|/|\nabla V|_{max}$, and moves the points in that direction times some small stepsize. If the one-dimensional solution is thick-walled (that is, $\vec{\phi}(\rho{=}0)$ is not very close $\vec{\phi}_T$), the algorithm also moves $\vec{\phi}_0$ in the direction of N averaged over the first several points (note that $N(\rho{=}0) = 0$ as long as the path aligns with ∇V). Otherwise, $\vec{\phi}_0$ stays fixed at $\vec{\phi}_T$. It then recalculates the spline coefficients by a least-squares fit to the moved points with the restriction that the path aligns with ∇V at $\vec{\phi}_0$ when thick-walled. The deformation converges when the normal force is much smaller than forces parallel to the path. At this point, the algorithm recalculates $\left|\frac{d\vec{\phi}}{d\rho}\right|$ and deforms the path again. After repeating this procedure a few times, the deformation should converge after a single step and the algorithm will return the final tunneling solution.

Choosing an appropriate stepsize is important. Errors in individual steps are generally self-correcting, but only for small stepsizes. Consider a situation in which the correct tunneling path is a straight line, but we introduce errors in the deformation to add

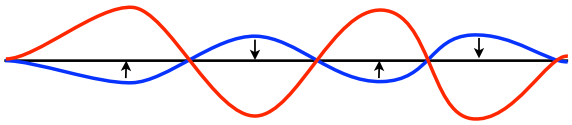

Figure 3.5: Example of error correction in deformation. The normal force will push wiggles down towards the straight line solution. But if the stepsize is too large, the wiggles will get reversed and amplified instead.

wiggles (see figure 3.5). A small stepsize in deformation will tend to smooth out the errors, but a large stepsize will instead reverse and amplify them. By checking for such reversals, the algorithm can keep the stepsize at the appropriate level.

3.2 Exploring phase structures

In order to determine the characteristics of a phase transition, we must first find where, and at what temperatures, the various phases exist. In theories with spontaneously broken symmetries there is at least one zero-temperature phase and there is generally one high-temperature symmetry-restoring phase. If these phases coexistence at some temperature, then there is likely a first-order phase transition between them. However, even in relatively simple models there can be intermediate phases (see, e.g., Ref. [92]) which can lead to secondary phase transitions, or can change the quality of the primary transition. Therefore, it is helpful to find the location of the minima as a function of temperature.

By writing the potential about any point $\vec{\phi}'$ as

$$V(\vec{\phi}, T) = a_i + b_i(\phi_i - \phi_i') + \frac{1}{2} M_{ij}(\phi_i - \phi_i')(\phi_j - \phi_j') + \cdots , \tag{3.8}$$

where $b_i = \frac{\partial V}{\partial \phi_i}$ and $M_{ij} = \frac{\partial^2 V}{\partial \phi_i \partial \phi_j}$, one can show that there is a (nearby) minimum at

$\vec{\phi}_{min} - \vec{\phi}' = -M^{-1}\vec{b}$. Therefore, the change in the minimum with respect to temperature is

$$\frac{\partial \vec{\phi}_{min}}{\partial T} = -M^{-1}\frac{\partial \vec{b}}{\partial T} - \left(\frac{\partial}{\partial T}M^{-1}\right)\vec{b} = -M^{-1}\frac{\partial \vec{b}}{\partial T}, \tag{3.9}$$

since $\vec{b} = 0$ at the minimum. Given a minimum at a single temperature, this allows one to find all of the minima of a given phase as a function of T. A singular matrix M indicates a rapid change in the minimum caused by either the disappearance of the phase or a second-order phase transition. A negative eigenvalue in M indicates that the extremum is no longer a minimum.

Practically, it is much easier to use this equation in conjunction with a minimization routine than it is to integrate it by itself. The algorithm in `transitionFinder.traceMinimum` uses the Nelder-Mead downhill simplex method [93] to find the local minimum at particular temperatures, and then uses equation 3.9 to find how the minimum changes. The former acts as an error check on the latter, which allows for an adaptive stepsize in the temperature. Once the phase disappears, the downhill simplex method can search for a new phase and then trace that. In this manner, one can trace the phase structure of the entire theory (assuming that each phase can be found by minimizing the potential at one of the ends of the other phases using the downhill simplex method). If there are multiple distinct phases at zero temperature, it is necessary to manually enter their (approximate) locations in order to trace them independently.

3.3 Structure of a simple program

There are essentially three parts to a simple program using my code: the tunneling algorithms and phase tracing algorithms described above, and the implementation of a

specific model. Much of this last task happens in the `generic_potential` class, which must be subclassed to study any particular theory.

From the point of view of the finite temperature effective potential, the theory is completely determined by the tree-level potential and field-dependent mass spectrum. The `generic_potential` class calculates the one-loop corrections from these masses using $\overline{\text{MS}}$ renormalization [94, 95]

$$V_1(\vec{\phi}) = \pm\frac{1}{64\pi^2}\sum_i n_i m_i^4(\vec{\phi})\left[\log\frac{m_i^2(\vec{\phi})}{Q^2} - c_i\right], \tag{3.10}$$

where n_i and m_i are the numbers of degrees of freedom and the field-dependent masses of each particle species. The quantity Q is the renormalization scale; $c = 1/2$ for gauge boson transverse modes and $3/2$ for all other particles; and the upper (lower) sign is for bosons (fermions). The one-loop finite-temperature corrections are

$$V_1(\vec{\phi}, T) = \frac{T^4}{2\pi^2}\sum_i n_i J_\mp\left[\frac{m_i(\vec{\phi})}{T}\right] \tag{3.11}$$

with

$$J_\mp(x) = \pm\int_0^\infty dy\, y^2 \log\left(1 \mp e^{-\sqrt{y^2+x^2}}\right). \tag{3.12}$$

The functions $J_\mp(x)$ are implemented in the module `finiteT.py` using direct integration and cubic interpolation. Of course, one can add additional structure (such as counter-terms) to a subclass.

To create a fully functioning model using the CosmoTransitions package, one need only subclass `generic_potential` and overwrite four functions: the initialization function `init()` to specify the number of field dimensions, the tree-level potential function `V0()`, and the mass-spectrum functions `boson_massSq()` and `fermion_massSq()`.

At high temperature, the perturbative expansion of the effective potential fails and must be supplemented with daisy resummation, which amounts to adding thermal masses to all bosonic propagators [96, 97]. These temperature-dependent masses can easily be added directly to `boson_massSq()`. Generally, one only needs to add the thermal masses to zero-mode propagators, corresponding to the cubic terms in $J(x)$, but it is easier in this program to add them to all propagators and all terms in $J(x)$.

Additionally, one should overwrite `approxZeroTMin()` to return the approximate locations of the zero temperature minima, especially if more than one minimum exists. Calling the function `getPhases()` will run routines from `transitionFinder.py` and calculate the phase structure of the theory. The critical temperature(s) (the temperature of degenerate minima between two phases) can be found by calling the function `calcTcTrans()`, while the function `calcFullTrans()` will find the amount of supercooling and the critical bubble profile for each transition. The supercooling criterion defaults to $S_E/T = 140$, which corresponds to the nucleation temperature in the electroweak phase transition, but this can easily be changed to study other phase transitions using the parameter `nuclCriterion` in `calcFullTrans()`.

3.4 Numerical results

3.4.1 Deformation

To test the path deformation and tunneling routines, I use a simple potential given by

$$V(x, y) = \left(x^2 + y^2\right)\left[1.8(x-1)^2 + 0.2(y-1)^2 - \delta\right]. \tag{3.13}$$

This has one local minimum at $x = y = 0$, and a global minimum near $x = y = 1$. For $\delta \ll 1$, the phases are nearly degenerate and any tunneling between them will be thin-walled.

I run the `pathDeformation.fullTunneling` class for both thin ($\delta = 0.02$) and thick-walled ($\delta = 0.4$) potentials, with results shown in figure 3.6. Each line represents 15 individual deformation steps with adaptive stepsizes on the order of 0.005. In this case, and in general, the thick-walled case converges more slowly due to the added complication of moving $\phi_0 = \phi(\rho = 0)$ with each step. The thin-walled case converges in ~ 60 steps, while the thick-walled case takes ~ 150 steps.

To check the deformation solution, I numerically integrate the equations of motion 3.3, using manual trial and error to find the correct initial conditions. These are shown in figure 3.6 as the red dashed lines. The deformation algorithm gets extremely close to—but not exactly to—the integrated solution. In the thin-walled case, the deformed path is within 0.1% of the integrated solution (defined as the largest distance separating the two paths divided by the total path length), while in the thick-walled case the error is 0.3%.

3.4.2 Calculating transition temperatures

To demonstrate the transition finding algorithms, I consider a theory with two scalar fields and a tree-level potential

$$V_0(s_1, s_2) = \frac{1}{8}\frac{m_1^2}{v^2}\left(s_1^2 - v^2\right)^2 + \frac{1}{8}\frac{m_2^2}{v^2}\left(s_2^2 - v^2\right)^2 - \mu^2 s_1 s_2. \tag{3.14}$$

When $\mu^2 = 0$, the theory has four identical minima located at $(s_1, s_2) = (\pm v, \pm v)$ and $(s_1, s_2) = (\pm v, \mp v)$. The effect of $\mu^2 > 0$ is to lower the minima at $(\pm v, \pm v)$ and raise those

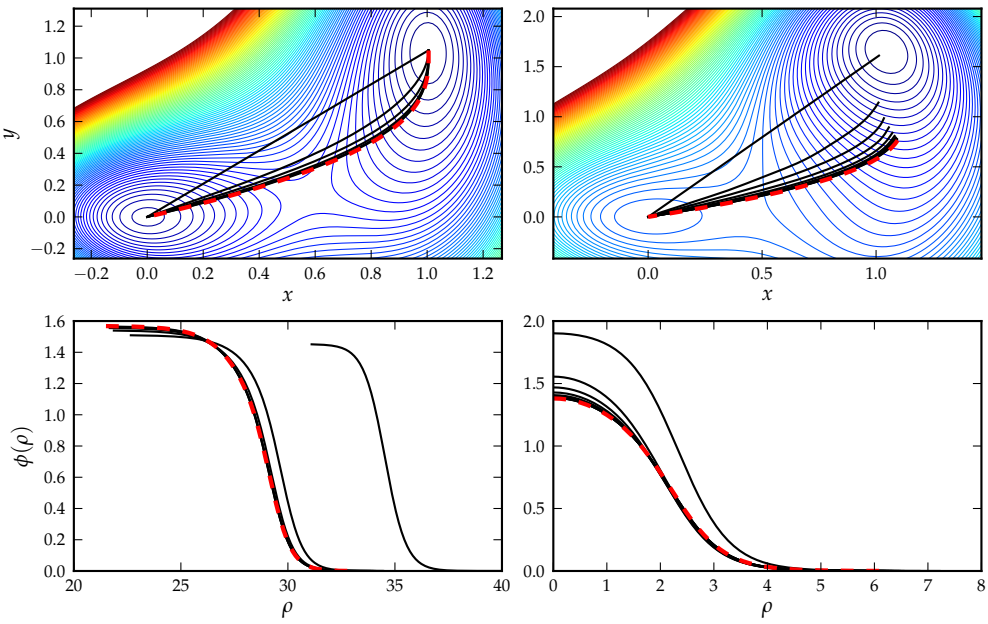

Figure 3.6: Top: the potential $V(x, y)$ given by equation 3.13 for $\delta = 0.02$ (left) and $\delta = 0.4$ (right). Black lines show successive deformations of the tunneling path, while red dashed lines show direct integration of equation 3.3 with manually chosen initial conditions. Note that the x and y axes are not to scale, so ∇V does not appear perpendicular to the contour lines. Bottom: the bubble profiles associated with each of the above deformations, where $\phi(\rho)$ is measured along the path.

at $(\pm v, \mp v)$. The tree-level scalar mass-matrix is

$$m_{ij}^2(s_1, s_2) = \frac{1}{2v^2} \begin{pmatrix} m_1^2(3s_1^2 - v^2) & -\mu^2 \\ -\mu^2 & m_2^2(3s_2^2 - v^2) \end{pmatrix}, \tag{3.15}$$

so that the masses at the tree-level minima are m_1 and m_2 when $\mu^2 = 0$. I also add an extra bosonic degree of freedom with the field-dependent mass

$$m_X(s_1, s_2) = y_A^2 \left(s_1^2 + s_2^2\right) + y_B^2 s_1 s_2. \tag{3.16}$$

The peculiar coupling y_B is designed to lift the minima at $(\pm v, \pm v)$ relative to $(\pm v, \mp v)$ at finite temperature so that there may be a phase transition between the two.

Table 3.1: Model parameters

m_1	m_2	μ	v	Q	y_A^2	y_B^2	n_X
120 GeV	50 GeV	25 GeV	246 GeV	246 GeV	0.10	0.15	30

I examine a model with the parameters given in table 3.1, where Q is the renormalization scale used in equation 3.10 and n_X is the number of degrees of freedom assigned to the extra boson with mass m_X. For this particular choice of parameters there are four local minima at tree-level, but loop corrections destroy the zero-temperature minima at $(\pm v, \mp v)$. I chose the parameters primarily to showcase multiple transitions within a single model, not for any physically motived purpose. The tunneling condition is $S_E/T = 140$.

Figure 3.7 shows the phase structure of the model, and figure 3.8 shows the general evolution of the potential as a function of temperature. At high temperatures, there is a single phase with $s_1 = s_2 = 0$. When the temperature drops to 128.2 GeV, a new phase appears at $(s_1, s_2) = (43, -33)$ GeV. The system tunnels to this phase at $T = 128.1$ GeV via a first-order phase transition (see figure 3.9), and the high-temperature phase disappears by $T = 127.6$ GeV. At $T = 112.2$ GeV, there is a small discontinuity due to the non-analyticity of $J_-(m/T)$ when $m = 0$. At the default resolution the algorithm registers this as a second-order phase transition, but for a small range of temperatures (112.14–112.22 GeV) there are actually two distinct phases separated by $\Delta\phi \approx 2$ GeV (that is, the algorithm sees that each phase terminates near $T = 112.2$ GeV, but it does not probe the small temperature window where they coexist. Instead, it assumes that they are continuously linked by a second-order transition). Immediately below this the system can be thought of as being in the phase associated with the tree-level vev at $(s_1, s_2) = (+v, -v)$. As the system cools,

the phase associated with $(s_1, s_2) = (+v, +v)$ appears, and by $T = 75.2$ GeV the two phases are degenerate. Below this the former phase is metastable, but it does not transition until $T = 54.4$ GeV, which is just above the point at which it disappears. Thus, the final tunneling is very thick-walled (see figure 3.9).

In order to reproduce these calculations, one needs to create an instance of the class `testModels.model1` with parameters given by table 3.1 and call the class functions `getPhases()`, `calcTcTrans()` and `calcFullTrans()` with their default parameters. Much of the plotting can be handled by the functions `plot2d()` and `plotPhasesPhi()`.

To check that the code works with three scalar fields, I simply add an extra field to the potential such that its minimum is always zero: $V_0(s_1, s_2, s_3) = V_0(s_1, s_2) + v^2 s_3^2$. I then rotate s_2 and s_3 by 45°. This gives an easily visualizable potential with non-trivial minima. Running the above commands produces the same results as in the two-dimensional model within the default error tolerances. I successfully tested a four dimensional model in a similar way. In four dimensions, the transition finding routine with default resolution labels the highest temperature transition as second-order instead of weakly first-order, but this can be corrected by increasing the resolution. Higher dimensional models have not been tested, but the code was written to support an arbitrary number of scalar fields.

3.5 Summary

I presented the publicly available CosmoTransitions package to analyze cosmological phase transitions. This included algorithms to find the temperature-dependent phase minima, their critical temperatures, and the actual nucleation temperatures and tunneling

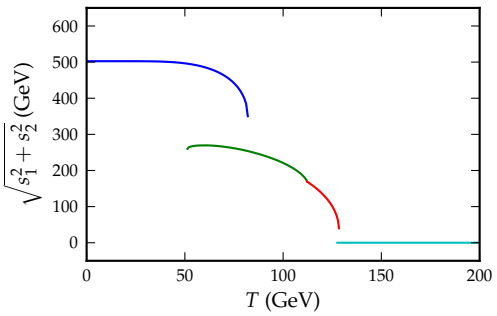

Figure 3.7: The position of the minima as a function of temperature.

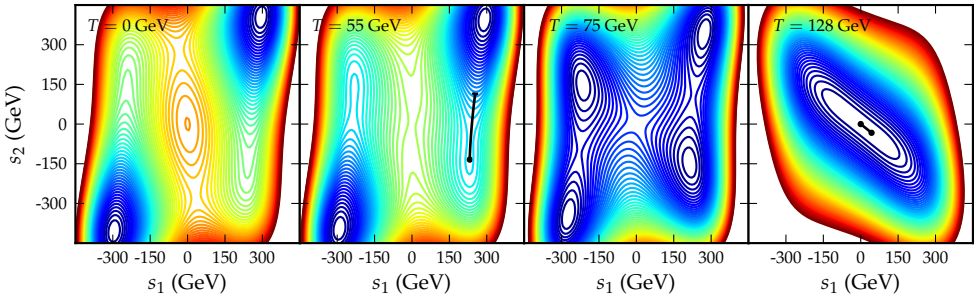

Figure 3.8: The finite-temperature effective potential $V(s_1, s_2, T)$ at $T = 0$, 55, 75, and 128 GeV. Thick black lines at $T = 55$ and 128 GeV show the tunneling paths for the phase transitions.

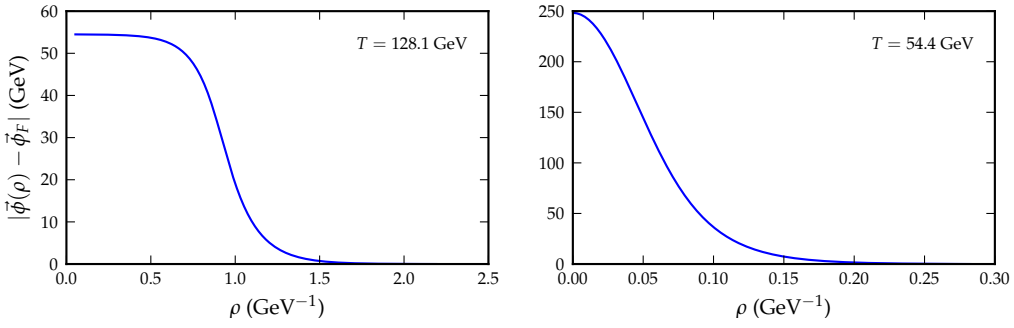

Figure 3.9: Bubble profiles along the tunneling paths for both the high- and low-temperature phase transitions. The high-temperature profile is (relatively) thin-walled, while the low-temperature profile is very much thick-walled.

profiles of the transitions. I introduced a novel method of path deformation to find the profiles, which I then demonstrated in simple test cases to accuracies of order $\sim 0.1\%$. The deformation algorithm has been successfully tested in 2 and 3 dimensions with both thick- and thin-walled profiles, but it should work in any number of higher dimensions as well.

CosmoTransitions is designed to be easily extensible, with minimal work needed on the part of the model builder. A new model can be created by subclassing the `generic_potential` class and specifying only the number of dynamic scalar fields, the tree-level potential, and the field-dependent particle spectrum. This will (hopefully) allow for the quick analysis of phase transitions in many extensions to the standard model.

Chapter 4

Gravity Waves from a Cosmological Phase Transition: Gauge Artifacts and Daisy Resummations

The search for gravitational waves is entering an exciting phase. The current generation of experiments is already delivering interesting results, including recent limits on the amplitude of stochastic gravitational wave backgrounds from the LIGO Collaboration [98, 99]. Rapid advances in the development of space-borne detectors [100] that might be operational in the relatively near future are also expected [101].

As pointed out long ago [54, 102, 103], cosmological phase transitions in the early universe might produce an imprint in the form of a stochastic background of relic gravity waves. These would arise as a result of the collision or turbulent motion of bubbles of "true vacuum" expanding and eventually filling the metastable vacuum in a cosmological first order phase transition [104]. The resulting signal might be large enough to be detectable by the next generation gravity wave search experiments, providing a unique window on the early cosmological history of the universe [105].

The spectrum of the gravity wave background arising from a first order cosmological phase transition is controlled by two physical properties of the phase transition itself: (a) the amount of false vacuum energy liberated during the phase transition – in other words, the latent heat associated with the transition; and (b) the bubble nucleation time scale, which gives a measure of how rapidly the phase transition occurs relative to the early universe Hubble expansion rate [104, 106]. The resulting gravity wave normalization and spectral peak can be estimated as a function of these two physical quantities. Detailed analytical [104, 86] and numerical [107, 108] studies exist that relate the two parameters to the predicted spectrum, in particular for the case of detonations, where the speed of the bubble wall is larger than the speed of sound (see Ref. [108] for a discussion of the opposite

case of deflagration).

One class of models where a strongly first order phase transition is a necessary ingredient is electroweak baryogenesis [109]. In the presence of B-violating electroweak sphalerons in the Standard Model(SM) and sources of CP-violation beyond those of the CKM CP violating phase, the electroweak phase transition (EWPT) can produce a sufficiently large baryon number density to explain the observed baryon asymmetry (for recent studies see e.g. [57, 58, 59, 30, 60, 61, 63, 19, 65, 66, 110, 68, 69]. To prevent the washout of the produced asymmetry, the phase transition must be strongly first order, thus necessarily producing gravity waves. Interestingly, the typical frequencies at which gravity waves from the EWPT are red-shifted today falls in the milli-Hertz to Hertz range, where the expected sensitivity of the space-based interferometer LISA is maximal. The search for a gravity wave relic from the EWPT is therefore especially intriguing and promising (see e.g. [111, 112]).

From a particle physics perspective, the determination of the details of an EWPT depends on the calculation of the finite-temperature effective action $\Gamma_{\rm eff}$ as a function of the background bosonic fields — denoted generically here as $\varphi(x)$ — that are present in the theory. In the case of the SM, lattice computations and the LEP lower bound on the mass of the Higgs boson imply that electroweak symmetry breaking in a SM universe occurs through a cross-over transition[73, 75]. To obtain a strongly first-order EWPT as needed for both electroweak baryogenesis (EWB) and the associated relic gravity waves, one must augment the SM scalar sector by the addition of new scalar fields, such as a second Higgs $\mathrm{SU}(2)_L$ doublet as in the Minimal Supersymmetric Standard Model (MSSM) [57, 58, 59, 30, 60, 61, 63] or a real singlet in minimal extensions of the SM scalar sector

(see e.g. [19]). Electroweak bubble nucleation occurs when a combination of the one of these new fields and the neutral component of the SM Higgs doublet becomes non-zero. The properties of relic gravity waves produced by bubble collisions then follows from the behavior of $\Gamma_{\rm eff}[\varphi(x)]$.

The most theoretically robust computations of the effective action are performed using non-pertrubative (lattice) methods. Given the cost of such computations, however, this approach is not feasible for exploring EWPT dynamics in a variety of beyond the Standard Model (BSM) scenarios. Consequently, one must resort to perturbation theory which, in turn, requires introduction of gauge-fixing. As recognized long ago [113], perturbative computations of the effective potential — and more generally $\Gamma_{\rm eff}[\varphi(x)]$ — generically lead to a gauge-dependent function. Physical quantities like the latent heat or the bubble nucleation rate should not, however, exhibit any gauge dependence.

In fact, general arguments imply that the critical temperature [114] and the bubble nucleation rate [115] are gauge independent. These statements follow from the so-called Nielsen identities and their generalization [116, 117] that describe the dependence of the effective action on the gauge fixing condition imposed on the quantized fields. In particular, the effective action $\Gamma_{\rm eff}[\varphi(x)]$ is gauge-invariant when $\varphi(x)$ is an extremal configuration, that is, one satisfying the equations of motion[1]. In principle, then, one should be able to obtain physical, gauge-invariant quantities relevant to the EWPT from $\Gamma_{\rm eff}$ by working with an appropriate set of extremal field configurations.

In practice, a non-trivial gauge-dependence can enter perturbative computations

[1]In the case of the effective potential, $\varphi(x) = \text{const} \equiv \varphi_{\rm min}$ is just the spacetime independent background field (*e.g.*, Higgs vacuum expectation value) that gives a minimum or maximum of the potential.

from an inconsistent truncation of the perturbative expansion[118]. In the context of sphaleron-induced baryon number washout, following on earlier work by Refs. [119, 120, 121], it was shown in Ref. [118] how a consistent, systematic order-by-order approach can yield a gauge-invariant perturbative result. However, most of the remaining literature on the topic of the EWPT, including the context of gravity wave production and of baryogenesis relevant here, appears to suffer from gauge-dependence (typically, perturbative calculations of EWPT-relevant quantities have been performed in the Landau gauge)[2]. Apart from the point of principle, the question then arises as to the quantitative impact that this gauge artifact has upon predictions of observable quantities.

In the present study, we address this question as it pertains to computations of gravitational wave spectra from a first order EWPT. To that end, we consider the simplest model involving scalar fields charged under a gauge group: the Abelian Higgs model, also known as the Coleman-Weinberg or scalar QED model. We then resort to a class of gauges known as R_ξ (or renormalizable) gauges, and we calculate the effective potential at finite temperature including its explicit dependence on the parameter ξ.

Studying the Abelian Higgs model has two clear advantages. First, its parameter space is small and easily analyzed. Second, and more importantly, one may calculate its effective potential using a gauge-invariant Hamiltonian approach[122] whose results can be compared with those obtained from the gauge-dependent approach. We then calculate quantities relevant to the character, strength and duration of the EWPT both in the R_ξ gauges (including Landau gauge) and in the gauge-invariant approach, and systematically

[2]To our knowledge, there exist no non-perturbative computations of all of the quantities relevant for predictions of GW spectra.

compare the results.

We find that the gauge choice may have a dramatic impact, amounting to several orders of magnitude, on the inferred gravity wave spectrum, and even on the first- or second-order character of the phase transition itself. We also observe that the Landau gauge results closely matches, at least for the Abelian Higgs model, the results using the explicitly gauge-invariant Hamiltonian formulation. This situation is perhaps not surprising, given the arguments in Ref. [123] (see below). We caution however that this conclusion might not be easily generalizable to non-Abelian gauge theories and that even in the Abelian Higgs model, a gauge-invariant resummation of higher-order terms that would otherwise spoil the convergence of the perturbative expansion remains to be developed[3]. To underscore the importance of the latter problem, we study the impact of including the "daisy resummation" in R_ξ gauges. We find that in the Landau gauge, inclusion of the resummation typically reduces the overall amplitude of the GW spectrum compared to the gauge-invariant but un-resummed result. We then comment on strategies to tackle these issues in non-Abelian models (such as the Standard Model or its supersymmetric extensions) – including those of Ref. [118].

We begin in section 4.1 with the explicit calculation of the gauge-dependence of the effective potential, at both zero and finite temperature, for the Abelian Higgs model. In section 4.2, we explain the calculations required to predict gravitational wave spectra and other physical observables related to the phase transition. Finally, we present our results and conclusions in sections 4.3 and 4.4.

[3] A gauge-invariant prescription for estimating these terms was developed in Ref. [118].

4.1 Gauge Dependence of the Effective Potential

We are concerned here with an Abelian Higgs model encompassing a complex singlet Higgs field with Lagrangian

$$\mathcal{L} = -\frac{1}{4}F_{\mu\nu}F^{\mu\nu} + \frac{1}{2}(D_\mu\phi)^* D^\mu\phi - V_0(\phi^*\phi), \tag{4.1}$$

where $F_{\mu\nu} = \partial_\mu A_\nu - \partial_\nu A_\mu$ and $D_\mu = \partial_\mu - ieA_\mu$ are the standard electromagnetic tensor and covariant derivative, respectively. The potential V_0 is

$$V_0(\phi^*\phi) = -\frac{1}{2}m^2\phi^*\phi + \frac{1}{8}\lambda(\phi^*\phi)^2. \tag{4.2}$$

The tree-level vacuum expectation value is $v^2 = \frac{2m^2}{\lambda}$, and the bare Higgs mass at the vacuum expectation value (vev) is $m_h^2 = 2m^2$.

In order to perform perturbative calculations, we must add gauge-fixing and ghost terms to the Lagrangian. In the R_ξ gauge, these are

$$\mathcal{L}_{gf} + \mathcal{L}_{ghost} = -\frac{1}{2\xi}(\partial_\mu A^\mu + \xi ev\eta)^2 + \partial_\mu\bar{c}\partial^\mu c - \xi e^2 v\sigma\bar{c}c, \tag{4.3}$$

where c is the Grassmann-valued ghost field, and where we have split ϕ into its real and imaginary components: $\phi = \sigma + i\eta$. We choose the vev such that $\langle\eta\rangle = 0$, making σ the physical Higgs boson and η the non-physical goldstone boson. Note that in Landau gauge ($\xi = 0$, fixing $\partial_\mu A^\mu = 0$), the ghost field completely decouples from the theory.

To include finite-temperature corrections, we must go to (at least) one-loop order in the effective potential. At zero-temperature, the calculation of the one-loop effective potential proceeds by taking the trace of the inverse propagators for each particle. This yields terms like $\frac{1}{2}\int \frac{d^4k}{(2\pi)^4}\log(k^2 + m_i^2(\sigma))$, although determining the proper expression for

the ξ-dependence of the gauge boson is somewhat complicated by the need to sum over Lorentz indices (see, *e.g.*, Ref. [124]). Using $\overline{MS}$ renormalization, the full one-loop zero-temperature potential is

$$V_1(\sigma, T=0) = \sum_{\text{particles}} \frac{n_i}{64\pi^2} m_i^4(\sigma) \left[\log\left(\frac{m_i^2(\sigma)}{\mu^2} \right) - c \right], \tag{4.4}$$

where n_i are the degrees of freedom for each particle and $c = \frac{1}{2}$ for the gauge boson's transverse modes and $c = \frac{3}{2}$ for its other modes and all other particles[4]. Table 4.1 lists all particle masses and their degrees of freedom. Several of the masses are gauge-dependent, and, precisely because of this fact, the effective potential is also gauge-dependent. Note that at both the origin and the tree-level vev ($\sigma^2 = v^2 = 2m^2/\lambda$) the gauge-dependence disappears[118], as expected from the Nielsen identities [116, 117]. However, the value of σ that minimizes the one-loop effective potential *is not* gauge invariant.

For the particular case of the Abelian Higgs model, Fischler and Brout [123] defined an effective potential from the vacuum-to-vacuum S-matrix element without resorting to the introduction of sources, a procedure that contrasts with the conventional definition in terms of the Legendre transform of the source-dependent generating functional, $Z[j]$. In this context, the "free-energy" is minimized by a spacetime-independent background field only in the Landau gauge, whereas in other gauges the minimizing fields must carry a spacetime dependence. Consequently, only in the Landau gauge does the minimum of the effective potential in the absence of sources characterize the presence or absence of symmetry-breaking. For the formulation with sources, a spacetime-independent background field will yield the minimum of energy in any gauge of the form given in Eq. (4.3), implying

[4]In the literature, authors generally use $c = \frac{5}{6}$ for all three physical modes of the gauge boson. This only makes a difference if one includes thermal masses in the zero-temperature potential, which is a small correction that few authors include.

particles	d.o.f.	$(\text{masses})^2$	$(\text{thermal masses})^2$
transverse gauge polarization	2	$e^2\sigma^2$	
longitudinal gauge polarization	1	$e^2\sigma^2$	$\frac{1}{3}e^2T^2$
time-like gauge polarization	1	$\xi e^2\sigma^2$	
higgs boson	1	$-m^2+\frac{3}{2}\lambda\sigma^2$	$(\frac{1}{3}\lambda+\frac{1}{4}e^2)T^2$
goldstone boson	1	$-m^2+(\frac{1}{2}\lambda+\xi e^2)\sigma^2$	$(\frac{1}{3}\lambda+\frac{1}{4}e^2)T^2$
ghosts	-2	$\xi e^2\sigma^2$	

Table 4.1: Particle content of the Abelian Higgs model, including Fadeev-Popov ghosts. One ghost effectively cancels the contribution from the unphysical time-like polarization, while the other cancels either the longitudinal polarization (at $\sigma = 0$) or the goldstone boson (at $\sigma = v$).

equal values of the minima of the effective potential for any choice of ξ [116, 117]. While the formulation of Ref. [123] is manifestly gauge invariant by construction, its relationship with the development in terms of sources has not to our knowledge been clarified. That being said, the arguments of Ref. [123] are suggestive that results obtained with the Landau gauge effective potential may be most physically reasonable. Indeed, we find close numerical agreement between Landau gauge quantities and those obtained using an explicitly gauge-invariant Hamiltonian formalism (see below). We emphasize, however, that this agreement does not carry over to the non-Abelian case.

The finite temperature contribution can be derived similarly to the zero-temperature contribution, except that the integral over momenta is replaced with a sum over Matsubara modes: $\int dk^0 \to \frac{1}{\beta}\sum_\beta$ and $k^0 \to \frac{2n\pi}{\beta}$. This yields

$$V_1(\sigma, T>0) = \frac{T^4}{2\pi^2}\sum_{\text{particles}} J\left[\frac{m_i^2(\sigma)}{T^2}\right], \tag{4.5}$$

where

$$J(x^2) \equiv \int_0^\infty dy\, y^2 \log\left(1-e^{-\sqrt{y^2+x^2}}\right). \tag{4.6}$$

In the high-temperature (low-x) limit,

$$J(x^2) \approx -\frac{\pi^4}{45} + \frac{\pi^2}{12}x^2 - \frac{\pi}{6}x^3 - \frac{x^4}{32}\log\frac{x^2}{a_b} - \mathcal{O}(x^6) \tag{4.7}$$

where $\log a_b = \frac{3}{2} - 2\gamma_E + 2\log(4\pi)$ and γ_E is the Euler constant [33]. All higher-order terms are simple polynomials in x^2. Again, the gauge dependence disappears at $\sigma^2 = v^2$ and at $\sigma = 0$, but it is non-trivial everywhere else. We also observe that the general arguments in Ref. [123] do not depend on whether one works with a Minkowski or Euclidean formulation of the functional integral appearing in the generating functional, so that even at finite-T use of the Landau gauge is equivalent to a gauge-invariant formulation for the Abelian Higgs model.

4.1.1 Thermal Mass Corrections

It is well-known that near the critical temperature for a phase transition, validity of the perturbative expansion of the effective potential breaks down. Quadratically divergent contributions from non-zero Matsubara modes must be re-summed through inclusion of thermal masses in the one-loop propagators[96, 97]: $m^2(\sigma) \to m^2_{eff}(\sigma) = m^2(\sigma) + m^2_{therm}(T)$. Table 4.1 lists all thermal mass corrections (see ref. [125] for further discussion and explicit calculations of the masses). Generally, one performs this "daisy resummation" by only including the thermal masses in the zero-mode propagators, which results in a mass correction to only the cubic term in the effective potential. It is slightly more convenient from a computational standpoint to include the corrections in all propagators, although we do check that this only makes a small difference in the resulting potential.

4.1.2 Alternative Gauge Invariant Formulation

For comparison, we also examine the gauge-invariant effective potential put forward by Boyanovsky et al. [122]. These authors derive the potential by working in the Hamiltonian formalism using only gauge-invariant physical states. In this case, there exist only four independent degrees of freedom (two transverse gauge, one longitudinal gauge, and Higgs), with no need for ghost cancellations. The unrenormalized one-loop effective potential is

$$V_1(\chi) = \frac{1}{2}\int \frac{d^3k}{(2\pi^3)} \left[2\omega_T + \omega_h + \omega_p\right], \tag{4.8}$$

where $\omega_T^2 = k^2 + m_T^2$ and $\omega_h^2 = k^2 + m_h^2$ arise from the transverse gauge and Higgs degrees of freedom, respectively, and the plasma frequency $\omega_p^2 = (k^2 + m_g^2)(k^2 + m_T^2)/k^2$ contains the contribution of both the gauge boson's longitudinal polarization and the Goldstone boson. The order parameter χ is a spacetime-independent, gauge-independent shift of the field, and the gauge, Higgs, and Goldstone masses m_T, m_h, and m_g are given in table 4.1 with $\xi = 0$ and $\sigma \to \chi$. The tree-level potential is unchanged.

The first two contributions to $V_1(\chi)$ exactly match the transverse gauge polarization and Higgs boson contributions to the potential in R_ξ gauge. At the tree-level extrema, the plasma frequency also matches the contributions from all other modes. However, away from the tree-level extrema, the plasma frequency does not match and looks similar only to Landau gauge ($\xi = 0$), as one would expect from the general arguments in Ref. [123]. Therefore, we anticipate the Landau gauge will provide a close approximation to the gauge-independent Hamiltonian result, a conclusion similar to what was found in Boyanovsky et al. [122].

Using $\overline{MS}$ regularization (see the appendix), we find that the plasma frequency contribution to the one-loop potential is

$$V_{1p}(\chi, T=0) = \frac{1}{64\pi^2}\left[(m_T^2 - m_g^2)^2\left(\log\frac{m_T^2 - m_g^2}{\mu^2} - \frac{3}{2}\right) + 4m_T^2 m_g^2\right] \tag{4.9}$$

$$V_{1p}(\chi, T>0) = \frac{T^4}{2\pi^2} J_2\left(\frac{m_T^2}{T^2}, \frac{m_g^2}{T^2}\right), \tag{4.10}$$

where J_2 is calculated by Boyanovsky et al. to be

$$J_2(a^2, b^2) \equiv \int_0^\infty dy\, y^2 \log\left[1 - e^{-\frac{1}{x}\sqrt{(y^2+a^2)(y^2+b^2)}}\right]. \tag{4.11}$$

In the high temperature expansion, Boyanovsky et al. find that their gauge invariant potential is the same as the potential in Landau gauge up to the cubic terms, but the equality breaks down beyond this.

In what follows, we compare results for the GW spectra using the Lagrangian and gauge-invariant Hamiltonian methods. We observe that the daisy resummation of higher-order contributions was not considered in Ref. [122], and it is not immediately clear how one would do so. Consequently, when comparing results in the two approaches, we will not include the Daisy resummation in the Lagrangian formulation.

4.2 Calculation of GW Parameters

We calculate several parameters of interest to gravitational wave production from early universe phase transitions using the Abelian Higgs model with full and explicit gauge dependence in the class of R_ξ gauges. These include the transition temperature T_*, the minima of the low and high-temperature phases at the transition, the relative change in energy density α, and the approximate duration of the phase transition β^{-1}.

4.2.1 Calculating the Transition Temperature

In first-order cosmological phase transitions, the low-temperature phase develops by nucleating bubbles within the high-temperature phase (see Refs. [35, 37, 126] for original work on cosmological transitions). A critical bubble—one whose surface tension exactly balances its outward pressure—is given by the $\mathcal{O}(3)$ symmetric action

$$S_3 = 4\pi \int_0^\infty r^2 dr \left[\frac{1}{2} \left(\frac{d\sigma}{dr} \right)^2 + V(\sigma(r), T) \right], \tag{4.12}$$

subject to the constraints that the field is smooth at $r = 0$ and in the high-temperature minimum at $r = \infty$. Smaller bubbles collapse, while larger bubbles grow and eventually fill the universe with the new phase. Equation 4.12 yields the radial equation of motion

$$\frac{d^2\sigma}{dr^2} + \frac{2}{r}\frac{d\sigma}{dr} = \frac{\partial}{\partial\sigma} V(\sigma, T), \tag{4.13}$$

which we solve using the 'undershoot/overshoot' method (see e.g. Ref. [86]).

To find the exact transition temperature T_*, we must determine when the low-temperature phase nucleates at least one bubble per Hubble volume. The nucleation rate goes roughly as $\Gamma \propto T^4 e^{-S_3/T}$, where the constant of proportionality can be found largely on dimensional grounds. For electroweak scales, this gives a transition temperature determined by $S_3/T_* \sim 140$ (see e.g. Ref. [26]). Note that the exponent changes very rapidly, so determining the exact form of the coefficient is quantitatively unimportant.

Finding the minima of the low- and high-temperature phases can be a non-trivial task, especially since the high-temperature minimum is not necessarily at $\sigma = 0$ and intermediate minima can develop for $\xi > 0$ (see section 4.3 below). Our strategy, however, is fairly straightforward. We first observe that the transition occurs in the range $T_C > T_* > T_{\min}$,

where $T_{\min}$ is the lowest temperature at which the original, high-temperature phase exists and T_C is the temperature at which the minima of the potential in the two phases are degenerate. We then trace the low-temperature minimum upwards from $T = 0$ and the high-temperature minimum downwards from $T = T_0$ by numerically integrating

$$\frac{d\sigma_{min}}{dT} = -\left(\frac{\partial^2 V}{\partial\sigma\partial T}\right) / \left(\frac{\partial^2 V}{\partial\sigma^2}\right). \tag{4.14}$$

At each point, we calculate the transition rate by finding S_3. Following the evolution of the minima and S_c we then determine the temperature at which $S_3/T = 140$.

4.2.2 Calculating the Latent Heat and Transition Duration

With the transition temperature in hand, the relative change in energy densities α and transition duration β^{-1} follow without much effort. When evaluated at its minimum, the effective potential is the same as the free energy density of the system[5]. Therefore, the energy density difference between the two phases is

$$\Delta\rho = [V(\sigma_{hot}, T_*) + s_{hot}T_*] - [V(\sigma_{cold}, T_*) + s_{cold}T_*], \tag{4.15}$$

where the entropy density is $s = -\partial V/\partial T$. Note that at $T_* = T_c$, $\Delta\rho$ is identical to the latent heat. The quantity of interest in the production of gravitational waves is $\alpha = \Delta\rho/\rho_{rad}$, where $\rho_{rad} = \frac{g_*\pi^2}{30}T^4$ and g_* is the number of relativistic degrees of freedom at the phase transition, which we take to be 100.

Writing the bubble nucleation rate as $\Gamma = \Gamma_0 e^{\beta t}$, β^{-1} gives the approximate phase

[5]Here, we neglect kinetic energy contributions associated with non-vanishing gradients of the background field in the bubble walls.

transition duration. For a radiation dominated universe,

$$\frac{\beta}{H_*} = T_* \left. \frac{d(S_3/T)}{dT} \right|_{T_*} \tag{4.16}$$

where H_* is the Hubble expansion rate during the transition (see e.g. Ref. [86]).

4.2.3 Calculating GW Spectra

We employ here the analytical approximation provided in ref. [107] to the numerical simulations carried out in that same work. We refer the Reader to ref. [108] for further insights on the results of ref. [107] The gravity wave spectrum (more precisely, the gravity wave energy density per frequency octave) from collisions at production is parameterized by

$$\Omega_{\mathrm{GW}*}(f_*) = \tilde{\Omega}_{\mathrm{GW}*} \frac{(a+b)\tilde{f}_*^b f_*^a}{b\tilde{f}_*^{(a+b)} + a f_*^{(a+b)}}, \tag{4.17}$$

where the two exponents, obtained from fits to the numerical results, are set to $a = 2.8$ and $b = 1.0$. The spectrum is redshifted according to

$$\tilde{f} = 16.5 \times 10^{-3} \text{ mHz} \left(\frac{\tilde{f}_*}{\beta} \right) \left(\frac{\beta}{H_*} \right) \left(\frac{T_*}{100 \text{ GeV}} \right) \left(\frac{g_*}{100} \right)^{1/6}, \tag{4.18}$$

$$h^2 \tilde{\Omega}_{\mathrm{GW}} = 1.67 \times 10^{-5} \, \tilde{\Omega}_{\mathrm{GW}*} \left(\frac{100}{g_*} \right)^{1/3} \tag{4.19}$$

$$= 1.67 \times 10^{-5} \tilde{\Delta} \, \kappa^2 \left(\frac{H}{\beta} \right)^2 \left(\frac{\alpha}{\alpha+1} \right)^2 \left(\frac{100}{g_*} \right)^{1/3}, \tag{4.20}$$

with the functions $(\tilde{f}_*/\beta)$ and $\tilde{\Delta}$ depending on the bubble wall velocity v_b (and hence implicitly on the relative energy density difference α) according to the following parameterization (again as given in ref. [107]):

$$\tilde{\Delta}(v_b) = \frac{0.11 \, v_b^3}{0.42 + v_b^2} \tag{4.21}$$

$$(\tilde{f}_*/\beta)(v_b) = \frac{0.62}{1.8 - 0.1v_b + v_b^2}. \tag{4.22}$$

Finally, we employ the following parameterization for the bubble wall velocity [127]

$$v_b = \frac{\sqrt{1/3} + \sqrt{\alpha^2 + 2\alpha/3}}{1 + \alpha}, \tag{4.23}$$

valid in the limit of interest here of strongly first order phase transitions. Note that the overall amplitude scales as $h^2\tilde{\Omega}_{\rm GW} \propto g_*^{-7/3}$ for $\alpha \ll 1$, so it can be changed by several orders of magnitude by choosing a model with a different g_*.

There should also be a contribution to the GW spectra from the turbulence immediately following the bubble collisions (instead of from the collisions themselves), and this contribution may be quite large [128, 129]. However, this still requires a strongly first-order phase transition and will therefore contain gauge artifacts similar to those in the simpler calculation. For our toy model, the simpler calculation suffices for a demonstration of the gauge-dependence problem.

4.3 Numerical Results

In the most basic model without any additional fields, four parameters determine the effective potential: the tree-level Higgs mass m_h, the tree-level vev v, the gauge coupling e^2, and the renormalization scale μ. We vary only the first two of these, keeping $v = 246$ GeV and $\mu = 1$ TeV fixed. We include phase transition calculations using the gauge-invariant Hamiltonian formalism of Boyanovsky et al. [122] without resummation, shown in the figures as solid arrows.

In order to generate a fairly strong first-order phase transition, the gauge boson

mass must be relatively large. However, if the mass is too large then the one-loop zero-temperature potential overwhelms the tree-level potential and perturbation theory is unreliable. At the tree-level vev, $V_0(\sigma = v) = -\frac{1}{8}\lambda v^4$ and $V_1(\sigma = v, T = 0) = \frac{3}{64\pi^2}(e^2v^2)^2[\log(\frac{e^2v^2}{\mu^2}) - \frac{5}{6}]$ plus a small contribution from the Higgs boson. These two are roughly equal when $e^4 \approx 4\lambda$ or $e^2 \approx \frac{2m_h}{v}$. To be slightly more conservative, we demand that $e^2 \leq \frac{m_h}{v}$.

Figures 4.2–4.4 display our results for the gauge dependence of the different phase transition properties. All four properties—the transition temperature, the values of σ corresponding to the minima of the phases, the relative change in energy density, and the transition duration—heavily depend upon the choice of gauge. We also show the impact of including the daisy resummation, as discussed above.

Three broad features emerge from these figures. The results obtained with the Hamiltonian formulation most closely match the results of Landau gauge ($\xi = 0$). However, the match is not exact. Most significantly, the Hamiltonian approach yields a small but measurable increase in the critical and transition temperatures.

Second, at $\xi = 0$, there can exist significant shifts in the GW-wave relevant parameters due to the inclusion of the daisy resummation. Generally, one finds that the values of α are decreased while β/H_* are increased due to the inclusion of the resummation, implying a reduced amplitude and higher peak frequency in the GW spectrum. This significant departure from the fully gauge-invariant results (albeit within the Landau gauge) suggests that developing a gauge-invariant daisy resummation procedure will be essential for obtaining physically realistic predictions.

Third, the dependence on ξ can both exacerbate these differences and lead to new

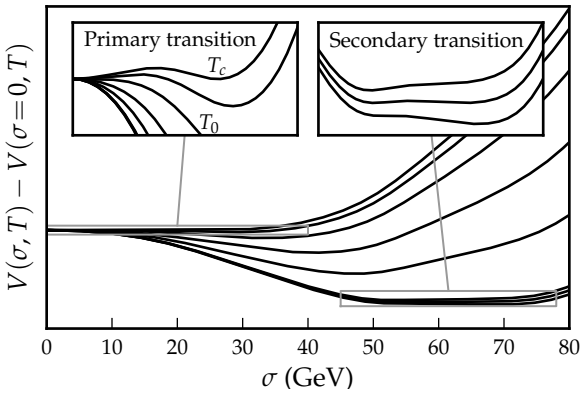

Figure 4.1: An example of multiple phase transitions in the same model. Here, $m_h = 35$ GeV, $e^2 = \frac{2m_h}{3v}$, and $\xi = 3$. Since the existence of the secondary phase transition is gauge-dependent, it is clearly non-physical.

phase structures that are clearly unphysical artifacts of the gauge choice. For example, for $m_h = 120$ GeV (fig. 4.4), the phase transition becomes second-order at high ξ, so the change in energy density goes to zero and β goes to infinity. A change in gauge can also lead to secondary minima and secondary transitions (see fig. 4.1). In figs. 4.2–4.4, we always perform calculations for the transition with the largest change in vev, even when this transition happens after initial symmetry breaking. This leads to the discontinuities in figs. 4.3 and 4.4. Given the unphysical nature of these artifacts, we do not discuss them further but simply point out the danger in this context of attempting to draw physical inferences from a gauge-dependent calculation.

Finally, we present our calculations for various gravitational wave spectra in figures 4.5–4.10. We make comparisons of the Hamiltonian approach and R_ξ gauges without daisy resummation in figures 4.5–4.7, and include the effects of resummation in figures 4.8–4.10. Again, Landau gauge and the Hamiltonian approach produce very similar results. However, a change in the gauge parameter produces very large changes in both the cal-

culated amplitude and peak frequency of the wave. Without daisy resummation it does not appear possible, or at least feasible, to determine which way this change will manifest without doing the full numerical calculation. With resummation, an increase in the gauge parameter tends to make the phase transition less strongly first-order, thereby decreasing amplitude and increasing the peak frequency of the resulting spectrum.

4.4 Summary

We have thus far presented numerical calculations of strongly first-order phase transitions and spectra of the resultant gravitational waves in the Abelian Higgs model both for various values of the gauge parameter ξ and in two gauge-invariant formalisms. The gauge-invariant Hamiltonian formalism closely matches Landau gauge. We find that small changes in ξ can produce large changes in calculated physical quantities, implying that attention to gauge invariance in GW computations is essential for reaching physically meaningful predictions. Moreover, we find that in the Lagrangian formalism, the result may be significantly affected by inclusion of the daisy resummation, a conclusion similar to what has been observed in the context of sphaleron rate computations[118].

From these observations, we conclude that the use of a non-gauge-invariant framework and the neglect of daisy resummations in computations of GW spectra for non-Abelian phase transitions are likely to lead to physically unreliable predictions. At present, it appears that the generalization of gauge-invariant perturbative methods applicable in the Abelian Higgs model to non-Abelian spontaneously broken theories is not straightforward. The Hamiltonian formalism does not easily carry over to the non-Abelian case and, given

how drastically observables change with a change in gauge parameter, one should not trust gauge-dependent calculations for anything other than rough estimates.

We see several possible directions. First, one can compute thermodynamic quantities of interest (such as α and T_*) as well as the bounce action with Monte Carlo methods, thereby circumventing the gauge problem at the outset while including all higher-order effects (including those entering daisy resummed perturbation theory) by construction. The results would undoubtedly be the most reliable theoretically, but this approach is unlikely to be practically feasible for surveying a wide variety of models or exploring wide regions of parameter space for models like the MSSM. As an alternative, following Ref. [118], one can use R_ξ gauge and the Nielsen identities to ensure gauge-independence at each order in $\hbar$. The latter approach is relatively straightforward conceptually, but computationally involved, as one must go to at least second order in the loop expansion. It appears particularly challenging in the case of the tunneling rate computation. From a more formal side, it may be possible to construct a gauge-invariant Hamiltonian formalism for spontaneously-broken non-Abelian gauge theories. Although we are not aware of any work in this particular direction, we note that such a formulation has been achieved in the absence of spontaneous symmetry breaking for the specific case of quantum chromodynamics (see, *e.g.*, Refs. [130, 131] and references therein).

4.5 Appendix: Calculating 1-loop zero-T potential

To calculate the one-loop potential, we must examine integrals like $\int \frac{d^3k}{(2\pi)^3}\omega$. For $\omega^2 = k^2 + m^2$, this gives the standard one-loop potential associated with a particle of mass

m. However, in the gauge invariant approach of Boyanovsky et al. the plasma frequency has the form $\omega_p^2 = (k^2+\alpha)(k^2+\beta)/k^2$. They perform the integral using a cutoff regulator, but we would like to use dimensional regularization in order to better compare with the R_ξ gauge.

The potential associated with the plasma mode is given by

$$V_p = \frac{\mu^{3-d}}{2}\int \frac{d^dk}{(2\pi)^d}\left(\frac{k^2}{(k^2+\alpha)(k^2+\beta)}\right)^n \tag{4.24}$$

with $d=3$ and $n=-\frac{1}{2}$, and μ is a mass dimension that balances the integration measure. For $n-\frac{d}{2}>0$, the integral converges. Performing the integral over the d-dimensional sphere yields

$$\begin{aligned} V_p =& \frac{1}{(4\pi)^{d/2}}\frac{1}{\Gamma(d/2)}\int dk\; k^{d-1}\left(\frac{k^2}{(k^2+\alpha)(k^2+\beta)}\right)^n \\ =& \frac{1}{(4\pi)^{d/2}}\frac{1}{\Gamma(d/2)}\frac{1}{2}\int dk\; \rho^{d/2-1}\left(\frac{\rho}{(\rho+\alpha)(\rho+\beta)}\right)^n. \end{aligned} \tag{4.25}$$

We can introduce a Feynman parameter to rewrite the fraction as

$$\left(\frac{\rho}{(\rho+\alpha)(\rho+\beta)}\right)^n = \int_0^1 dxdy\;\delta(x+y-1)\frac{(xy)^{n-1}}{(\rho+\alpha x+\beta y)^{2n}}. \tag{4.26}$$

Using this, and the definition of the beta function

$$\int_0^1 dx\; x^{a-1}(1-x)^{b-1} = B(a,b) = \frac{\Gamma(a)\Gamma(b)}{\Gamma(a+b)}, \tag{4.27}$$

one can show that

$$V_p = \frac{1}{(4\pi)^{d/2}}\frac{\Gamma(n+d/2)\Gamma(n-d/2)}{2\Gamma(d/2)\Gamma(n)^2}\int_0^1 dx\;[x(1-x)]^{n-1}[\alpha x+\beta(1-x)]^{d/2-n}. \tag{4.28}$$

Then, using the generalized binomial theorem,

$$V_p = \frac{1}{(4\pi)^{d/2}}\frac{\Gamma(n-d/2)}{2\Gamma(d/2)\Gamma(n)^2}\sum_{l=0}^{\infty}\frac{\Gamma(d/2-n+1)\Gamma(d/2-l)\Gamma(n+l)}{\Gamma(d/2-n+1-l)\Gamma(l+1)}\alpha^{d/2-n-l}\beta^l, \tag{4.29}$$

where we demand that $|\beta| \leq |\alpha|$. Expanding this out in $\epsilon = \frac{3-d}{2}$, one finds

$$V_p = \frac{1}{64\pi^2}\left[(\alpha-\beta)^2\left(-\frac{1}{\epsilon}+\gamma_E-\log(4\pi)\right)\right.$$
$$\left.+(\alpha-\beta)^2\left(\log\frac{\alpha-\beta}{\mu^2}-\frac{3}{2}\right)+4\alpha\beta\right]+\mathcal{O}(\epsilon), \quad (4.30)$$

where γ_E is the Euler-Mascheroni constant. In $\overline{MS}$ regularization, we simply subtract out the term containing $1/\epsilon$, as well as the γ_E and $\log(4\pi)$ terms. Note that for $\beta = 0$, this reproduces the standard one-loop potential in equation 4.4.

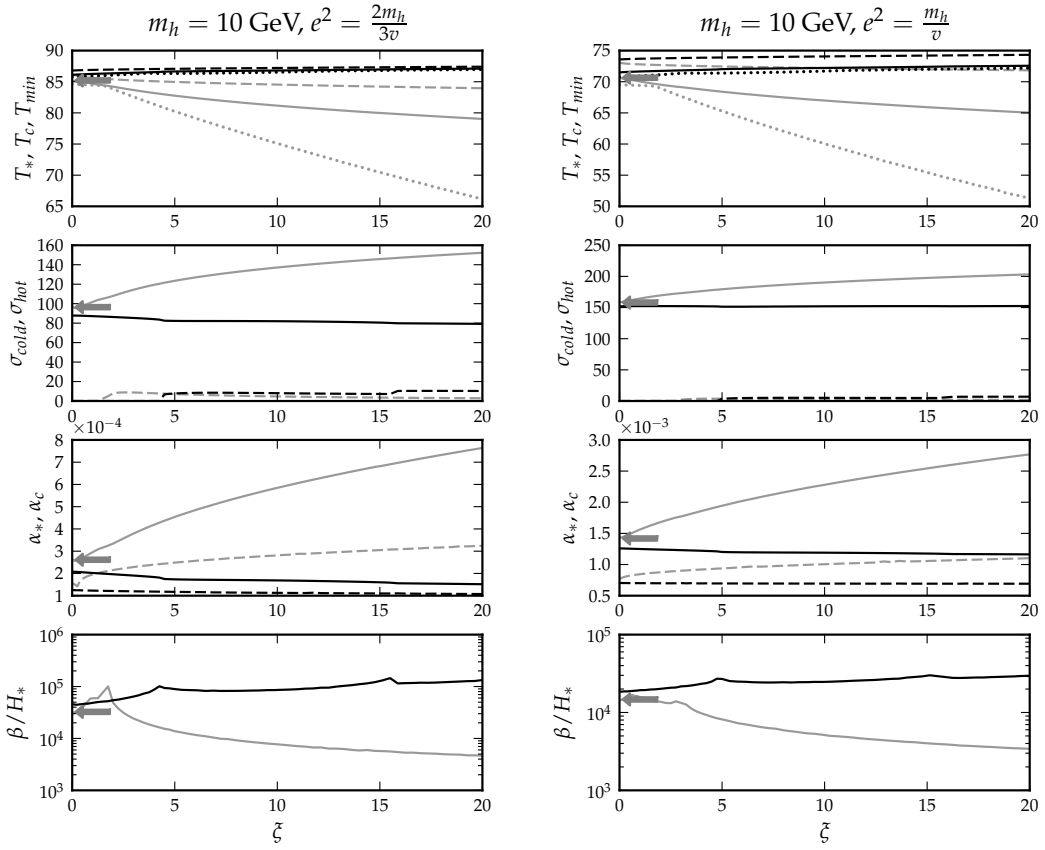

Figure 4.2: Calculated gauge dependence of phase transition parameters for a low-mass Higgs boson. In all panels, black (grey) lines denote models with (without) resummation. The arrows denote values corresponding to the solid lines, but calculated in the gauge-invariant Hamiltonian formalism. All quantities along the y-axes are in units of GeV, except for β/H which is unitless. In the first panel, solid, dashed and dotted lines denote the transition temperature T_*, the critical temperature T_c, and the minimum temperature at which the hot phase exists. In the second panel, solid and dashed lines denote the minima of the cold and hot phases. The third panel shows the relative difference in energy densities at both the critical temperature (dashed line) and the actual transition temperature (solid line). The final panel gives β/H_*, where β is the approximate inverse phase transition duration and H_* is the Hubble constant at the transition temperature.

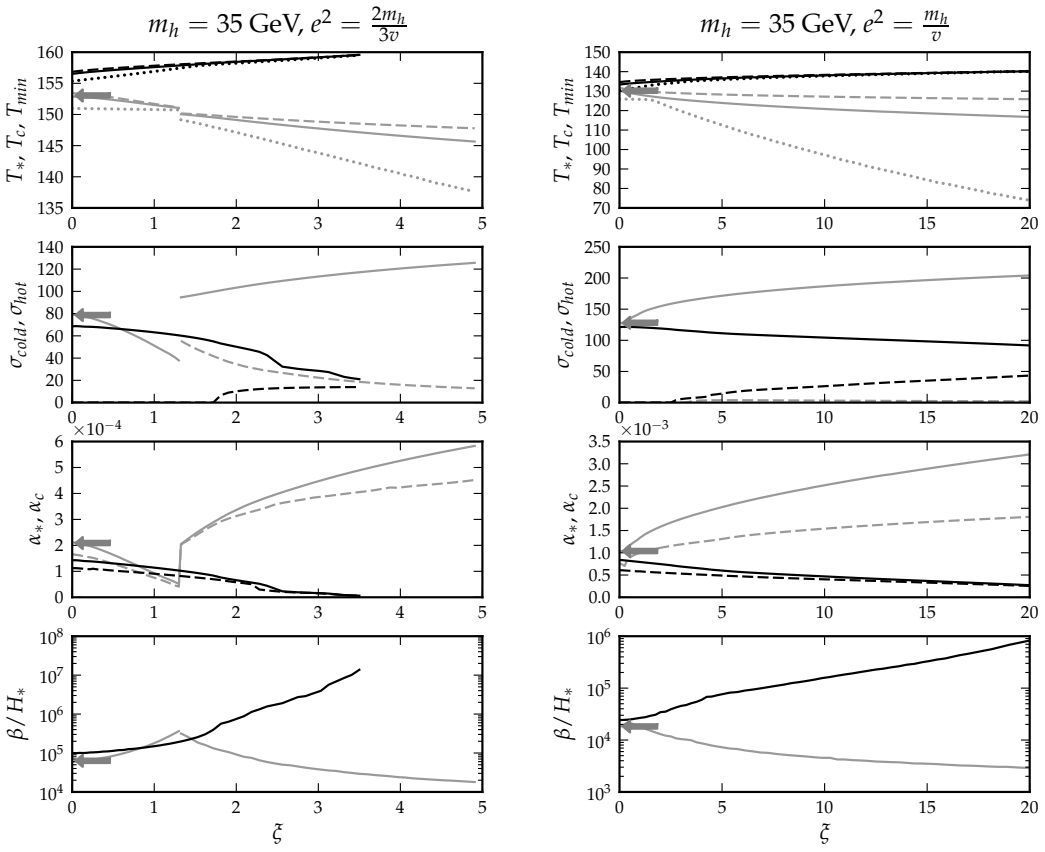

Figure 4.3: Calculated gauge dependence of phase transition parameters for a medium-mass Higgs boson. See fig. 4.2 for a thorough explanation of the different lines.

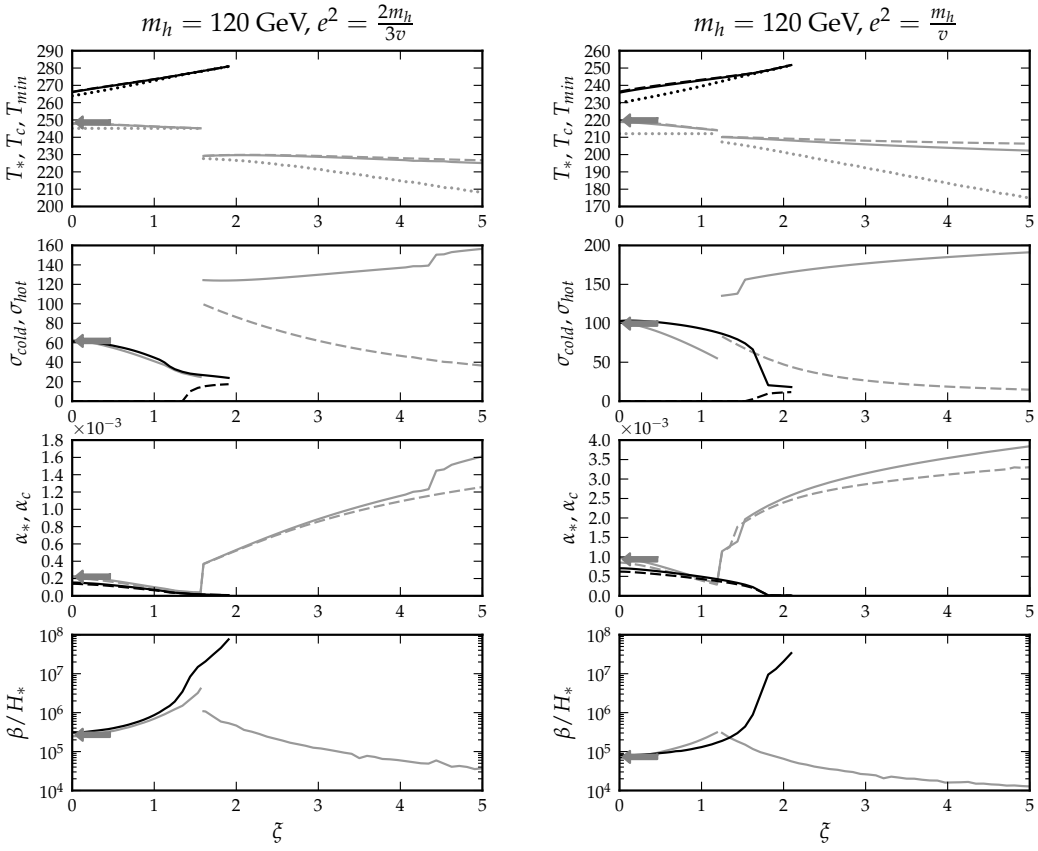

Figure 4.4: Calculated gauge dependence of phase transition parameters for a high-mass Higgs boson. See fig. 4.2 for a thorough explanation of the different lines.

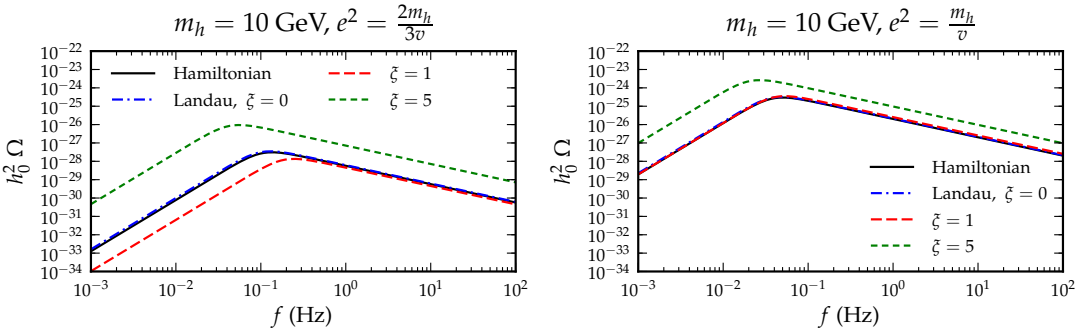

Figure 4.5: Expected gravitational wave spectrum for a Higgs mass of 10 GeV, calculated in Landau gauge ($\xi = 0$), two high-ξ gauges ($\xi = 1, 5$), and the gauge-invariant Hamiltonian formalism.

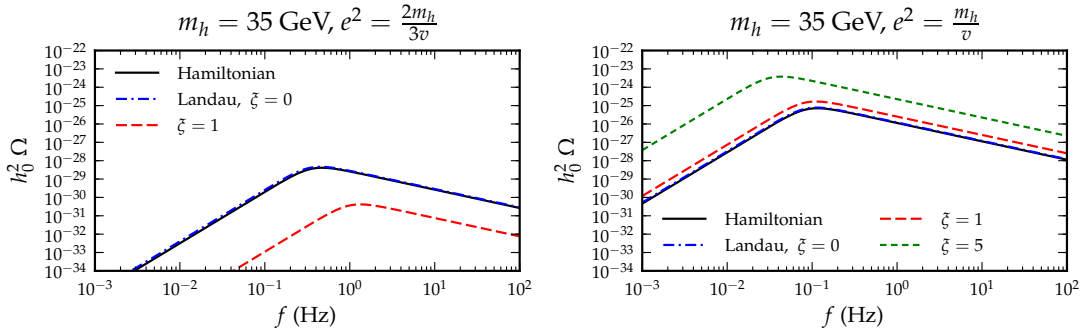

Figure 4.6: Expected gravitational wave spectrum for a Higgs mass of 35 GeV, calculated in Landau gauge ($\xi = 0$), one or two high-ξ gauges ($\xi = 1, 5$), and the gauge-invariant Hamiltonian formalism.

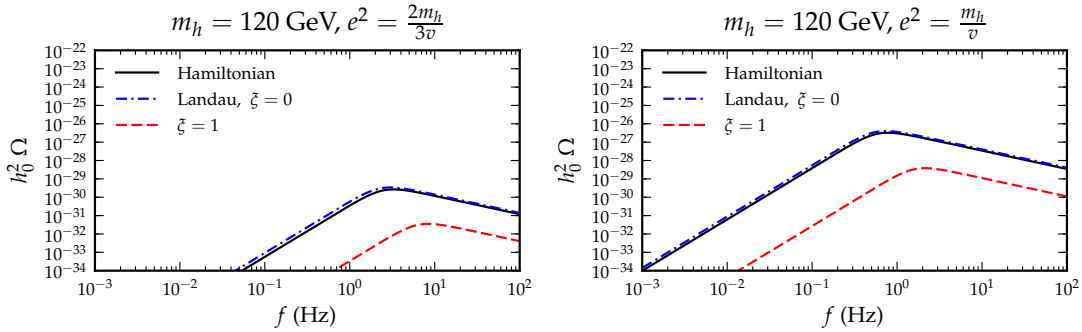

Figure 4.7: Expected gravitational wave spectrum for a Higgs mass of 120 GeV, calculated in Landau gauge ($\xi = 0$), a high-ξ gauge ($\xi = 1$), and the gauge-invariant Hamiltonian formalism.

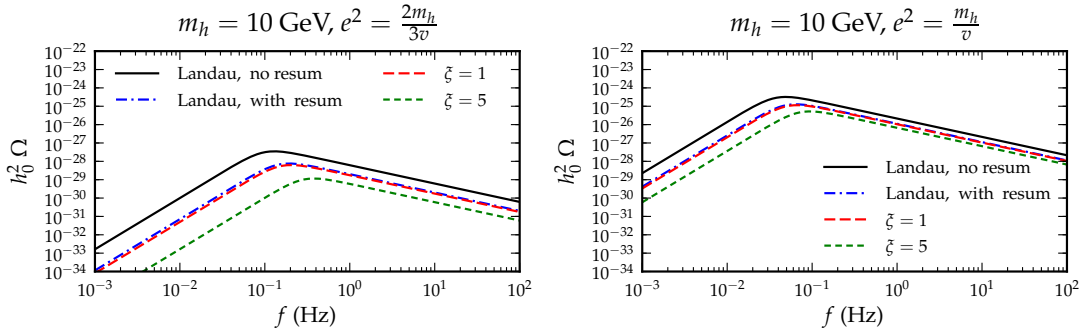

Figure 4.8: Comparison of gravitational wave spectra calculated without daisy resummation in Landau gauge, and with resummation (dashed lines) in Landau gauge and two other R_ξ gauges.

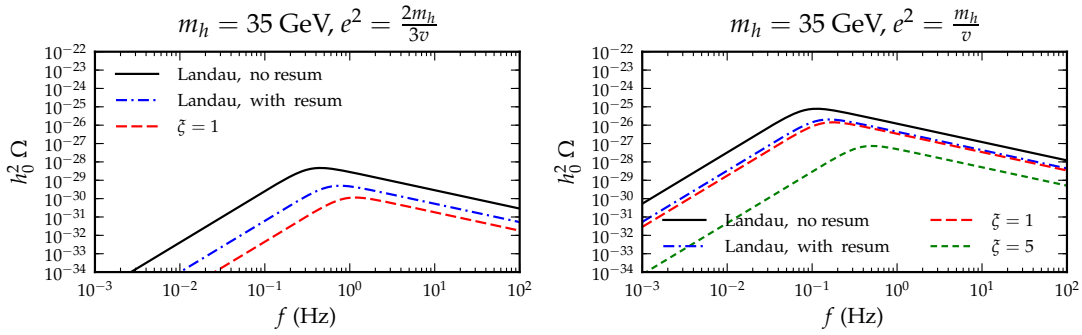

Figure 4.9: Comparison of gravitational wave spectra calculated without daisy resummation in Landau gauge, and with resummation (dashed lines) in Landau gauge and one or two other R_ξ gauges.

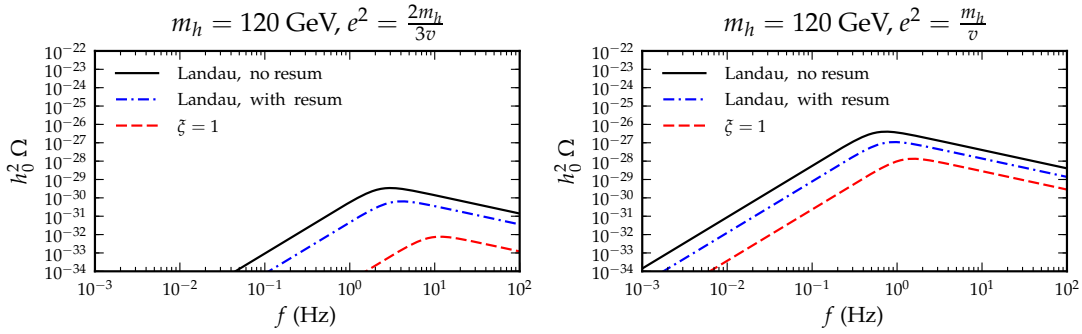

Figure 4.10: Comparison of gravitational wave spectra calculated without daisy resummation in Landau gauge, and with resummation (dashed lines) in Landau gauge and one other R_ξ gauge.

Chapter 5

Phase Transitions and Gauge Artifacts in an Abelian Higgs Plus Singlet Model

Cosmological phase transitions related to the spontaneous breaking of symmetries in fundamental physics are believed to be potentially connected with the deepest questions concerning the early evolution of the universe [54]. They may pertain to such diverse topics as the origin of seed intergalactic magnetic fields (see e.g. [132]), the excess of baryons over anti-baryons (e.g. [133]) and a possible isotropic background of gravitational waves (see e.g. [134]). These topics are highly timely, especially in view of the recent claimed detection of small but non-vanishing intergalactic magnetic fields [135, 136], progress in electric dipole moment searches [137, 68], dark matter [138] and direct collider searches [139] for signatures of electroweak baryogenesis [29], and, finally, with a new generation of experiments looking for gravity waves [100], that will soon boost the already significant results of current detectors [98].

The possibility of an electroweak phase transition (EWPT) associated with electroweak symmetry breaking (EWSB) is especially relevant. In the Standard Model (SM), EWSB entails the Higgs field acquiring a non-vanishing vacuum expectation value (vev) that breaks the $\mathrm{SU}(2)\times\mathrm{U}(1)_Y$ gauge group down to $\mathrm{U}(1)_{\mathrm{e.m.}}$ and generates masses of the weak gauge bosons and the SM fermions. The nature of EWSB is governed by the interplay of SM gauge interactions and the Higgs quartic self-coupling, which also determines the value of the Higgs boson mass, m_H. The results of lattice simulations indicate that for $m_H \lesssim 70 - 80$ GeV, EWSB occurs via a first order EWPT, while for a heavier Higgs, the transition is a cross-over [73]. Given the present lower bounds on M_H obtained from LEP, Tevatron, and LHC searches [140, 76, 141, 142], one would conclude that an EWPT would not have occurred in a SM universe. On the other hand, extensions of the SM scalar sector

can readily lead to a first order EWPT as well as associated phenomenology for collider searches. In the context of electroweak baryogenesis the EWPT must be strongly first order in order to prevent excessive washout of the baryon asymmetry by sphaleron processes. Paradigmatic extensions to the Standard Model Higgs sector yielding a strongly first order EWPT include the minimal supersymmetric extension to the Standard Model (MSSM) with a light stop [143, 30], and theories (supersymmetric or not) that include one or more extra gauge-singlet fields [144, 145, 19, 59] (other scenarios are also possible, see e.g. [146]). These models typically predict distinctive collider signatures in regions of parameter space associated with a strong first order EWPT. Consequently, rapid progress in searches for the SM Higgs at the Large Hadron Collider [141, 142] will soon impact our understanding of a possible EWPT, elucidating whether or not the transition was strongly enough first-order for successful electroweak baryogenesis [139], whether it could have impacted thermal relic densities [70, 71], and whether it could have left any detectable imprint in the diffuse background of gravitational radiation [86, 92].

Once the field content of a theory is specified, the character of resulting phase transitions relies on the computation of an effective potential, $V_{\rm eff}$, while its dynamics follows from the associated effective action, $S_{\rm eff}$. Although the most robust techniques for computing these quantities employ non-perturbative methods, such as discretizing the theory on a lattice [147, 73, 75], in practice the resulting computational cost makes a perturbative calculation by far more feasible and, historically, preferentially pursued for phenomenology. However, perturbative calculations of the effective potential generically lead to gauge-dependent results, as pointed out long ago by Dolan and Jackiw [113] (see also Ref. [148]

for early work on gauge-dependence and symmetries at high temperature). Although it is straightforward to maintain gauge-invariance when carrying out calculations in the symmetric phase (where the vev is gauge-independent), such as computing the temperature of a second-order phase transition [149, 150, 151], it is doing so for the broken phase requires additional care. The generic dependence of the effective action on the gauge choice is described by the so-called Nielsen identities [116] and their generalizations [117]. In practice, the gauge invariance of the effective action is guaranteed when the background field $\varphi(x)$ is an extremal configuration, i.e. one that satisfies the equations of motion (in the case of the effective potential, $\varphi(x) = \varphi_{\min}$ is the value of the field corresponding to a minimum of the potential)[1]. Typically, gauge dependence stems from an inconsistent truncation of the perturbative expansion [118]. This leads, in turn, to effects in the critical temperature [114], in the bubble nucleation rate [115], and in the sphaleron transition rate [118] for a first order phase transition, ultimately resulting in unphysical gauge dependence in observable quantities such as the spectrum of gravity waves produced by bubble collision or turbulence [92].

The problem of gauge dependence as it relates to the description of cosmological phase transitions has recently attracted renewed attention. Following earlier studies [119, 120, 121], Ref. [118] addressed the possibility of producing a consistent, order-by-order gauge-invariant result in the perturbative expansion of the V_{eff} and S_{eff}. In the SM, this approach yields a gauge-invariant critical temperature T_C at one-loop order in a straightforward manner, and it can be refined to reproduce leading terms in the "daisy resummation"

[1]More generally, all background fields must be in extremal configurations. For example, the electroweak sphaleron involves non-vanishing scalar and gauge fields at the saddle point of the effective action.

in a gauge invariant manner. Doing so reproduces trends with model parameters that are observed in lattice studies, including the dependence of T_C on the top squark soft mass parameters in the MSSM. Application to computation of a gauge invariant sphaleron rate is also feasible. On the other hand, a gauge-invariant computation of the bubble nucleation rate in the SM requires going beyond one-loop order.

As an alternative to the SM, the Abelian Higgs model provides a theoretically attractive "laboratory" in which to assess various approaches to obtaining gauge-invariant quantities associated with symmetry-breaking. Apart from calculational ease, this model allows for the computation of a gauge-invariant effective potential using a Hamiltonian approach [122], making a comparison with results obtained with other methods possible. In Ref. [92], we explicitly addressed the case of an Abelian Higgs model, and calculated for a full set of R_ξ gauge choices the impact of gauge-dependence on physical observables. Doing so allowed us to directly compare the results of the computation for a generic R_ξ gauge choice with the gauge-independent calculation [123, 122].

While computationally tractable, the Abelian Higgs model arguably carries limited phenomenological interest. Among the more relevant SM extensions mentioned above – such as MSSM with a light stop or a gauge-singlet extension to the Higgs sector – it is possible to make the electroweak phase transition strongly first order via interactions that are gauge independent (though the full $V_{\rm eff}$ remains gauge-dependent). The simplest cases involve introduction of tree-levels term in the potential of the type $SH^\dagger H$ or $S^2H^\dagger H$ in the case of the real singlet extension. The tree-level cubic operator can produce a large potential barrier between the broken and unbroken phase at the electroweak phase transition, while

the quartic interaction may allow for a lowering of T_C in a manner compatible with collider constraints on m_H. As these operators are manifestly gauge-invariant, one may inquire as to whether perturbative computations of the EWPT properties in the associated models are quantitatively less susceptible to gauge-dependent artifacts than in either the SM or in the Abelian Higgs model. Indeed, Refs. [152, 139] have recently suggested that such a situation may occur.

In what follows, we study the issues described above in some detail. For the sake of comparing with a known, simple gauge-independent result, we shall again use the Abelian Higgs model, supplemented with a gauge-singlet real scalar field (which does not impact the gauge-dependence structure of the theory) and retaining only the tree-level cubic operator, $SH^\dagger H$. Arguably, this model is the simplest prototypical electroweak-like theory that can exhibit a strongly first order phase transition driven by tree-level cubic terms. In view of the recent LHC results pointing to a relatively heavy Higgs mass, singlet extensions to the electroweak scalar sector have additionally become phenomenologically more appealing, making an assessment of the gauge artifacts in the effective potential even more timely. We show that such gauge artifacts may arise even in the presence of a large tree-level singlet-Higgs cubic coupling. However, we also find that the gauge-dependence is less pronounced when the tree-level and loop-induced cubic interactions conspire to generate a sizeable barrier between the broken and unbroken phases at low temperatures.

The remainder of this paper is organized as follows: the next section describes in detail the theory we study, including explicit calculations of the gauge dependent terms in the effective potential. The following Section 5.2 gives an outline of the possible patterns

of spontaneous symmetry breaking, and describes the effects of gauge choices on various quantities of interest (including the critical temperature, the latent heat, and a measure of the strength of the phase transition). Finally, Section 5.3 summarizes and concludes.

5.1 The Abelian Higgs Model plus a Singlet Scalar

We examine the gauge dependence of a simple Abelian Higgs model containing a single complex scalar Φ charged under a local U(1) gauge group, and a real scalar singlet field s. For our purposes here, we consider only a cubic coupling between the two fields, as the latter can generate a tree-level barrier between the broken and unbroken phases and, thus, can increase the strength of the phase transition. The effect of the quartic operator discussed above is more subtle, so for simplicity we focus on the cubic interaction. At tree-level, the potential is

$$V_0(\Phi, s) = \tfrac{1}{4}\lambda_1(\Phi^\dagger\Phi)^2 + \tfrac{1}{2}\mu_1^2\Phi^\dagger\Phi + \tfrac{1}{4}\lambda_2 s^4 + \tfrac{1}{2}\mu_2^2 s^2 + \tfrac{1}{2}Es\Phi^\dagger\Phi. \tag{5.1}$$

It is useful to separate Φ into real and imaginary parts ($\Phi = h + ih'$) and then rotate into a basis such that only the real part gets a vev.

Rather than specifying the 5 coefficients explicitly, we find it more convenient to specify the vevs, the tree-level mass eigenstates, and the mixing of the mass eigenstates,

and use this to set the tree-level potential. The tree-level mass-squared matrix is

$$M_{ij}^2 = \begin{pmatrix} 3\lambda_1 h^2 + \mu_1^2 + Es & Eh \\ Eh & 3\lambda_2 s^2 + \mu_2^2 \end{pmatrix} \tag{5.2}$$

$$= \begin{pmatrix} \cos\theta & -\sin\theta \\ \sin\theta & \cos\theta \end{pmatrix} \begin{pmatrix} m_1^2 & 0 \\ 0 & m_2^2 \end{pmatrix} \begin{pmatrix} \cos\theta & \sin\theta \\ -\sin\theta & \cos\theta \end{pmatrix} \quad , \tag{5.3}$$

where the rotation angle θ gives the mass eigenstate mixing:

$$\tan(2\theta) = \frac{2M_{12}^2}{M_{11}^2 - M_{22}^2}. \tag{5.4}$$

The quantities m_1, m_2, and θ are most relevant to collider phenomenology, as they determine production cross sections and decay branching ratios. In particular, a non-zero mixing angle θ can weaken the collider constraints on the lightest mass eigenstate since its effective coupling to gauge bosons is reduced by $\cos\theta$. This effect opens up the possibility of a (stronger) first order phase transition by allowing for a smaller Higgs quartic self-coupling, although we do not study this effect in detail here. The corresponding minimization conditions are given by

$$\frac{\partial V_0}{\partial h} = (\lambda_1 h^2 + \mu_1^2 + Es)h = 0, \tag{5.5}$$

$$\frac{\partial V_0}{\partial s} = \lambda_2 s^3 + \mu_2^2 s + \tfrac{1}{2} E h^2 = 0. \tag{5.6}$$

From these we solve for $\lambda_1, \lambda_2, \mu_1^2, \mu_2^2$ and E in terms of vacuum expectation values of h and s, masses m_1 and m_2, and the angle θ, assuming that both h and s are non-zero. Note that for $E < 0$ (so that the $\langle s \rangle > 0$) and $m_1 < m_2$, we require $0 \leq \theta < 90°$. Also, λ_2 is negative for sufficiently large E, so not all values of θ lead to stable potentials.

For $h = 0$, extrema occur at $s = 0$ and — for $\mu_2^2 < 0$ — at $s = \pm|\mu_2|/\sqrt{\lambda_2}$. An additional three extrema can occur for $h > 0$, whose locations are trivially determined by

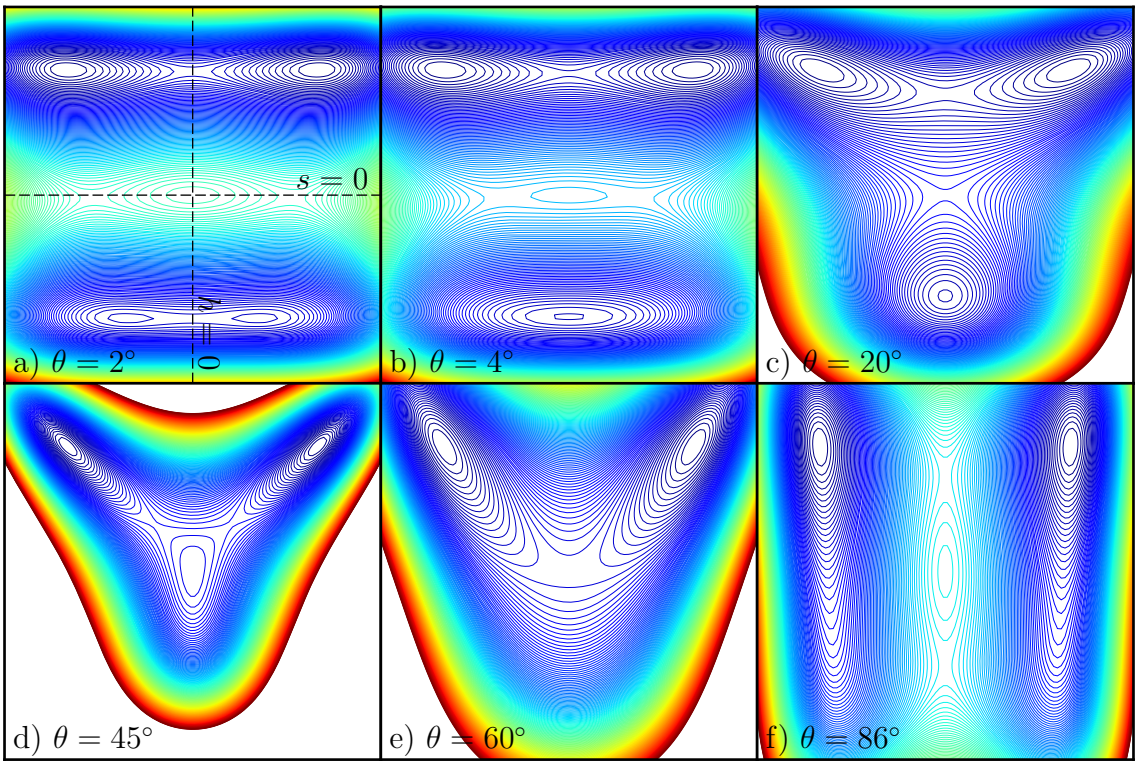

Figure 5.1: Contours of the tree-level potential for $m_1/m_2 = 0.4$ and six different values of θ. Red (blue) contour lines denote higher (lower) values of the potential. The Higgs and singlet fields vary along the horizontal and vertical axes, respectively. The origin, which is in the center of each plot, is a maximum in (a), (b), and (f), a saddle point in (c) and (e), and a minimum in (d).

solving the cubic equation in s obtained from from combining Eqs. (5.5) and (5.6):

$$\lambda_2 s^3 + (\mu_2^2 - \frac{E^2}{2\lambda_1})s - \frac{E}{2\lambda_1} = 0. \tag{5.7}$$

Since Eq. (5.7) has no term proportional to s^2, at most two of the extrema can be in any one quadrant. Also, since there are no linear or cubic terms in h, all maxima must lie along the s-axis. Using this knowledge, one can enumerate all of the different combinations of minima, maxima, and saddle points to obtain all of the different possible potential types.

From Eqs. (5.5,5.6) we observe that the location and character of the extrema depend on four independent parameters. For example, by scaling out a factor of λ_1 we may

take these parameters to be μ_1^2/λ_1, μ_2^2/λ_1, λ_2/λ_1, and E/λ_1. We may trade two of these parameters for one each of the non-zero vacuum expectation values of s and h, respectively. The remaining two parameters then determine θ and the ratio of masses m_1/m_2. The depth of the potential at one of the minima is then fixed by the fifth remaining parameter in the potential, which we can trade off for one of the masses. Therefore, we can keep two vevs and one of the masses fixed and just vary θ and the ratio m_1/m_2 to explore all potentials that are not related by an overall rescaling. Fig. 5.1 shows six different representative potentials with constant m_1/m_2.

Panel (a) shows the potential with a small positive value of θ, corresponding to a small negative E. There is a minimum in each quadrant of the h-s plane separated by four saddle points with a maximum at the origin. Increasing the angle θ (panels (b) and (c)) merges some of these features onto the s-axis. First, the two minima at $s < 0$ merge, then the two saddle points near $s = 0$ merge onto the origin such that the origin is no longer a maximum. Increasing θ further (panel (d)), pushes the minimum along the s-axis up to the origin. At this point there is a tree-level barrier between the broken and symmetric phases. In panel (e), this barrier disappears and there are only the two electroweak minima and a saddle point at the origin. Finally, panel (f) has a small value of $|E|$, but large enough to destroy the two metastable minima in panel (a). A further rotation to $\theta = 90^\circ$ would reproduce a potential of a type similar to what shown in panel (a). This basically exhausts all of the possibilities with symmetry-breaking minima: the only other potential type occurs at larger ratios of m_2/m_1. It is similar to type (d) except that the $h = 0$ minimum splits into two minima and a saddle point along the s-axis.

5.1.1 Quantum corrections

The one-loop corrections to the effective potential are given by

$$V_1 = \sum_i \frac{n_i}{64\pi^2} m_i^4 \left(\log \frac{m_i^2}{q^2} - c \right), \tag{5.8}$$

where n_i is the d.o.f. for each particle, m_i is the particle mass, q is the renormalization scale (which we set to 1 TeV), and $c = 1/2$ for transverse gauge boson polarizations and 3/2 for all other particles. The Higgs and scalar masses are given by the eigenvalues of the tree-level mass matrix (Eq. 5.2). The three gauge boson polarizations each contribute a mass $m_{gauge}^2 = g^2 h^2$. We focus on R_ξ gauge[2], in which there are gauge-dependent masses for the Goldstone boson and the ghost: $m_{gold}^2 = \lambda_1 h^2 + \mu_1^2 + Es + \xi g^2 h^2$ and $m_{ghost}^2 = \xi g^2 h^2$, with $n_{ghost} = -2$. There is an additional degree of freedom from the gauge boson's unphysical time-like polarization which exactly cancels one ghost degree of freedom. In all of our models the first derivatives ($\partial V_1/\partial h$ and $\partial V_1/\partial s$) are negative at the tree-level minimum. This pushes the vevs further away from the origin than they were at tree-level.

At finite temperature, the one-loop corrections are

$$V_{1,T\neq 0} = \frac{T^4}{2\pi^2} \sum_i n_i J\left[\frac{m_i^2(\phi)}{T^2} \right], \tag{5.9}$$

where

$$J(x^2) \equiv \int_0^\infty dy\, y^2 \log\left(1 - e^{-\sqrt{y^2+x^2}}\right). \tag{5.10}$$

In the high-temperature (low-x) limit,

$$J(x^2) \approx -\frac{\pi^4}{45} + \frac{\pi^2}{12}x^2 - \frac{\pi}{6}x^3 - \frac{x^4}{32}\log\frac{x^2}{a_b} - \mathcal{O}(x^6) \tag{5.11}$$

[2] In a previous study [92], we compared R_ξ gauge to the gauge-independent potential in Ref. [122] which uses a Hamiltonian formalism. The latter is more computationally intensive, and it tends to closely resemble Landau gauge ($\xi = 0$) in the Abelian Higgs model.

where $\log a_b = \frac{3}{2} - 2\gamma_E + 2\log(4\pi)$ and γ_E is the Euler constant [33]. $J(x^2)$ is not analytic at $x^2 = 0$, and it is complex for $x^2 < 0$. In our calculations, we approximate $J(x^2)$ with a cubic spline, taking only the real component for $x^2 < 0$.

At high temperature, the validity of the perturbative expansion of the effective potential breaks down. Quadratically divergent contributions from non-zero Matsubara modes must be re-summed through inclusion of thermal masses in the one-loop propagators [96, 97]: $m^2(\phi) \to m^2_{eff}(\phi) = m^2(\phi) + m^2_{therm}(T)$. This amounts to adding thermal masses to the scalars and gauge boson longitudinal polarizations:

$$M^2_{ij} \to M^2_{ij} + T^2 \begin{pmatrix} \lambda_1/3 + g^2/4 & 0 \\ 0 & \lambda_2/4 \end{pmatrix} \tag{5.12}$$

$$m^2_{gold} \to m^2_{gold} + T^2(\lambda_1/3 + g^2/4) \tag{5.13}$$

$$m^2_{long-gauge} \to m^2_{gauge} + T^2 g^2/3. \tag{5.14}$$

Note that the coefficients of the T^2 terms are ξ-independent.

When the phase transition is second-order or very weakly first-order, or when the temperature is very high, even the re-summed potential may not be reliable. Loops that are either infrared divergent or dominated by the infrared regime contribute linearly in temperature and can ruin the perturbative expansion (see, e.g., Ref [125]). Each additional such loop contributes roughly $\tilde{\lambda}T/M$, where $\tilde{\lambda}$ is the relevant coupling and M is the relevant mass scale. Substituting the gauge boson mass for M and g^2 for $\tilde{\lambda}$, we see that the perturbative expansion should hold as long as $h/T \gtrsim g$. We warn the Reader that for certain parameters in what follows this criterion breaks down. As a result, the one-loop expansion might have limited validity in those cases. This is particularly true for cases 1

and 2 with $g = 0.5$ and case 3 with $\theta \gtrsim 70°$. However, it is important to note that one could lower the phase transition temperature by e.g. extending the gauge group and adding extra gauge bosons. Extra degrees of freedom enhance the finite-temperature contributions relative to the tree-level potential, so symmetry breaking happens at lower temperatures. This in turn would make the one-loop perturbative expansion more reliable, without qualitatively changing the nature of the explicit gauge dependence. Since the appearance of the one-loop gauge dependence is not tied directly to the perturbative validity, and since our primary interest is in providing proof of existence for the gauge-dependence issues, we leave the perturbative breakdown problem to future studies.

5.2 Patterns of spontaneous symmetry breaking

We now study the gauge dependence in a few representative models with different qualitative features. In particular, we examine the gauge dependence of the nucleation temperature T_* and various measures of the phase transition strength. Nucleation occurs when the three-dimensional action S_3 of a nucleated bubble satisfies $S_3/T_* \approx 140$ (see Refs. [35, 36, 37] for original work on cosmological phase transitions), and we use this criterion to define T_*. The phase transition strength has often been characterized by $\Delta\phi$, the jump between the vevs of the two phases. However, as noted above, this quantity is ξ-dependent. Alternate, physically meaningful measures include (a) α, the difference in energy densities at the two vevs , and (b) a measure of the phase transition duration β^{-1}, defined as $\beta/H_* = T_*(d/dT)(S_3/T)$ where H_* is the Hubble parameter at the time of the transition. When the phases are degenerate and there is no supercooling, α is equivalent

to the transition's latent heat. The quantity β^{-1} effectively measures the strength of the transition, with $\beta = \infty$ for a second-order transition.

We use the CosmoTransitions package [153] to determine the phase structures and calculate the nucleation rates.

Table 5.1: Model parameters for three illustrative cases.

	$\langle h_{tree} \rangle$	$\langle s_{tree} \rangle$	m_1	m_2	θ	E
Case 1	240 GeV	48 GeV	120 GeV	35 GeV	$-1°$	-0.96 GeV
Case 2	240 GeV	48 GeV	120 GeV	180 GeV	$45°$	-37.5 GeV
Case 3	174 GeV	174 GeV	30 GeV	75 GeV	$60°$	-11.8 GeV

5.2.1 Gauge fields driving transitions

First, we examine two cases in which the transition would be second-order without the inclusion of massive gauge fields. Table 5.1 contains the corresponding model parameters. The two cases are quite similar: they have the same vevs, and they both have a saddle point at $h = s = 0$ with no other extrema along the s-axis (see Fig. 5.1(e)). However, case 1 has a very small cubic term while in the second case E is of the same order as the mass scale of the theory. The gauge dependence exhibited in case 1 is therefore unsurprising: since it has relatively weak coupling between the Higgs and the scalar singlet, we expect it to show the same sort of gauge dependence as an uncoupled Abelian Higgs model [92]. This is indeed the case, as seen in Fig. 5.2 (green lines).

For low values of the gauge coupling g, the gauge dependence is quite pronounced. The initial symmetry breaking (solid lines for the two cases) is weakly first-order (*e.g.*, $\alpha/T_*^4 \ll 1$) from $\xi = 0$ to $\xi \approx 1.5$. At higher ξ, a second-order transition initially breaks

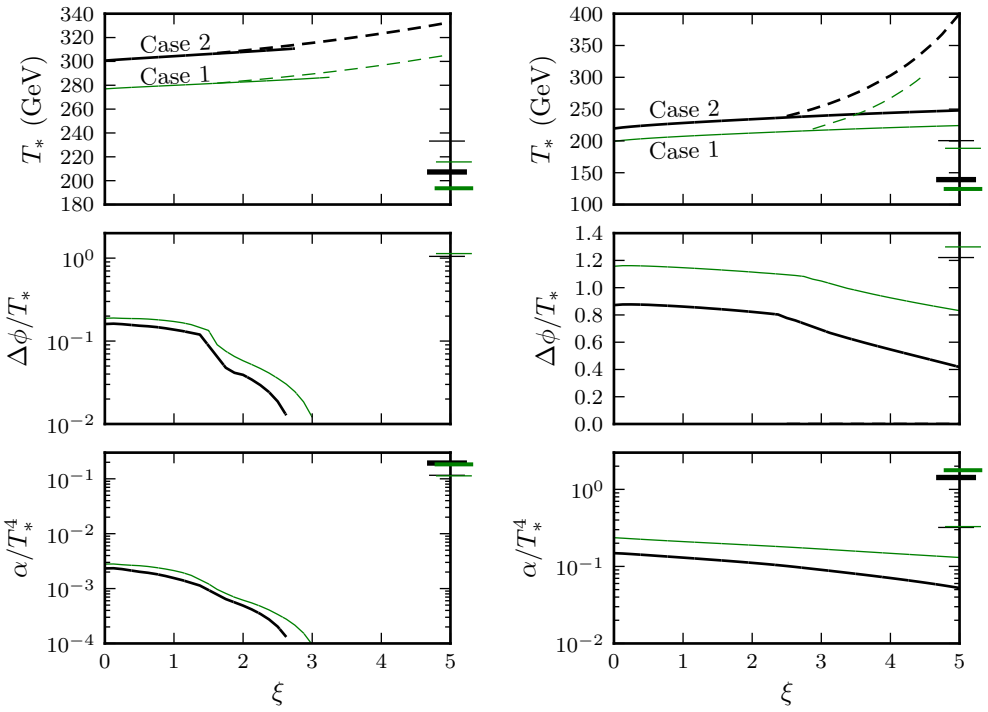

Figure 5.2: Gauge dependence in cases 1 (thin green lines) and 2 (black lines) as a function of the gauge parameter ξ. The left panels have a small gauge coupling $g = 0.5$, while the right have $g = 1.0$. Dashed lines represent second-order symmetry breaking transitions, which may be followed by a first-order transition at lower temperature. The marks along the right side of each panel show the corresponding quantity calculated using the gauge-invariant method of Ref. [118]. The thicker marks include a gauge-invariant treatment of the thermal masses; the thin marks ignore them.

the symmetry (dashed lines in Fig. 5.2). The first-order transition then proceeds from a high-temperature broken phase to the low-temperature broken phase at larger values of h and s. Above $\xi \approx 3$, the barrier between the two broken phases disappears and there is no first-order phase transition at all.

For higher values of g, the gauge dependence is not as pronounced. The phase transition is much more strongly first-order, with α/T_*^4 roughly a factor of 10 higher than it is for low g. The initial symmetry-breaking still turns second-order at high ξ, but the

subsequent first-order transition persists up to $\xi = 5$ with about a factor of 2 drop in α.

In all cases, the appearance of a strong first-order phase transition is associated with a large ratio of field-dependent heavy degrees of freedom (in this case, gauge bosons) to the Higgs mass. A small Higgs mass decreases the depth of potential (that is, $V_0(0) - V_0(v)$ decreases), while heavy additional field-dependent masses yield larger contributions to the thermal effective potential (increasing $V_1(v,T) - V_1(0,T)$). Both effects decrease the critical temperature and increase $\Delta\phi$. The presence of the additional field-dependent masses decreases the critical temperature because, for a given value of T, $V_1(v,T) - V_1(0,T)$ is larger for larger gauge couplings and the two minima are degenerate at lower temperatures. It increases the value of $\Delta\phi$ because $dJ/dx \to 0^+$ as $x \to \infty$, so when $x = m/T = gh/T$ is large, $\partial V_1/\partial h$ is small and the vev does not decrease much from its tree-level value. An increase in $\Delta\phi$ tends to increase both α (a larger separation between phases implies a larger difference in mass spectrums, entropy, and therefore latent heat) and β^{-1} (since S_3 scales as $(\Delta\phi)^3$). One can achieve a strongly first-order phase transition even for a heavy Higgs, as long as it is somewhat light compared to the other field-dependent masses.

Interestingly, case 2 (thick black lines) shows almost exactly the same gauge dependence as case 1, even though it has a non-trivial cubic term. The important point is that, although large, the cubic term is not large enough to cause a first-order phase transition without additional bosons that have large couplings to the Higgs field.

We compare the gauge-dependent calculations to explicitly gauge-independent calculations (denoted by marks along the right side of each panel in Fig. 5.2). At one-loop order and without the added thermal masses, the gauge-independent calculation is simply

the value of the potential evaluated at the tree-level minimum Φ_0, where ghost and goldstone degrees of freedom exactly cancel. Thermal masses spoil the cancellation, but one can still obtain a gauge-invariant result by evaluating the cubic terms in the ring-improved effective potential at the tree-level high-temperature minimum, where the tree-level high-temperature potential is the same as $V_0(\Phi)$ but with thermal masses added to μ_1^2 and μ_2^2. This is the lowest-order approximation used by Ref. [118]. Since the potential is evaluated at two different minima, a gauge-invariant ring-improved $\Delta\phi$ is not well-defined and is not plotted in Fig. 5.2.

Ignoring thermal masses, one can see that the gauge-invariant critical temperature must be lower than the gauge-dependent critical temperature for any value of ξ: the gauge-dependent critical temperature is defined as the temperature at which $V(\Phi_{min}, T) = V(\Phi = 0, T)$, but since Φ_{min} is the minimum of the potential, $V(\Phi_0, T) > V(\Phi_{min}, T) = V(\Phi = 0, T)$ and the gauge-invariant critical temperature must be lower. Conversely, the latent heat tends to be larger in the gauge-invariant method. The energy density decreases with increasing particle masses, so, as long as the masses are larger at Φ_0 than at Φ_{min} (which is the case for weakly first-order transitions), the difference in energy densities between the symmetric and broken phases will be larger when evaluated at Φ_0 than at Φ_{min}. The addition of thermal masses tends to enhance both of these effects.

The gauge-invariant method produces quite different results from the gauge-dependent calculation when the latter predicts a very weakly first-order transition. This is to be expected: the two methods perform calculations at very different field values when the gauge-dependent $\Delta\phi$ is small. When $g = 1$ and the transition is more strongly first-order, the two

methods agree much more closely. However, including thermal masses worsens the agreement. When $m_{gauge}/T \gtrsim 1$, higher-order terms in the effective potential dominate and using only the cubic term for ring-improvement is unreliable. The ring-improved gauge-invariant calculation should not be trusted in this case.

Fig. 5.3 explicitly shows the (non-)importance of the cubic term (*via* θ) in these scenarios. Regardless of whether the cubic term is large or small, the basic pattern of gauge-dependence is about the same. The phase transition grows more weakly first-order (α decreases) for increasing ξ for all values of θ. At $\xi \geq 3$, there is only a second-order transition. Note that the transition is most strongly first-order when $\tan\theta = \langle h_{tree}\rangle/\langle s_{tree}\rangle$, but still second-order for $\xi \geq 3$.

5.2.2 Tree-level terms driving transitions

Here we examine a scenario in which the cubic term is critical in determining the strength of the phase transition. Superficially, case 3 appears similar to case 2. Both have relatively large cubic terms, and both have the topology shown in Fig. 5.1e. However, a small change in model parameters can turn the saddle point in case 3 into a tree-level minimum (Fig. 5.1(d)), thus creating a potential barrier at zero temperature for which the tunneling rate may never be large enough to penetrate. Even without a tree-level barrier, the cubic term is sufficiently prominent to create a barrier at relatively low temperature: there is no barrier at $T = 0$, but there is a barrier by $T \approx 100$ GeV for $\theta = 60°$. Slightly smaller values of θ decrease this temperature drastically. The crucial distinction between cases 2 and 3 is that, even though both have large cubic terms, only in case 3 is the lowest eigevalue of the mass-squared matrix both negative and sufficiently small in magnitude (i.e.,

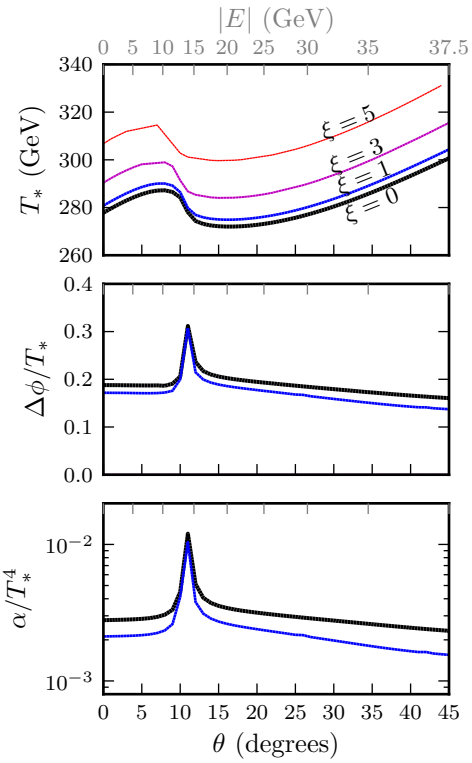

Figure 5.3: Gauge dependence in case 2 with $g = 0.5$, but with θ (or equivalently E) varied and ξ held fixed. The transition is second-order for $\xi \geq 3$ for all values of θ.

a small negative value of μ_1^2) that the origin can become a minimum at low temperature with the cubic term providing the separation between the symmetric and broken phases.

Since the phase transition is strongly first-order even for $g = 0$ (that is, without any gauge bosons at all), the gauge dependence is not nearly as severe as in cases 1 and 2. It is still present though. For example, at $\theta = 60°$, T_* increases by 1.6% from $\xi = 0$ to $\xi = 5$, and α increases by only 0.1%.

By increasing θ from 55° up to 90°, one moves successively through topologies (d), (e), (f), and (a) in Fig. 5.1. At around $\theta = 70°$ and $|E| = 9$ GeV, the cubic term is small enough so that a first-order phase transition requires $g > 0$. At this point, the gauge dependence becomes much more obvious, as is seen in Fig. 5.4. At high enough θ and low

enough E, the symmetry-breaking transition is second-order for all plotted values of ξ.

5.3 Summary

The main conclusion of the present study is that the inclusion of a singlet scalar degree of freedom does not generally alleviate the gauge-dependence problem in the electroweak phase transition, even when it has large couplings to the Higgs. Moreover, a significant, tree-level cubic singlet-Higgs interaction does not in itself guarantee a strongly first-order phase transition. On the other hand, when the phase transition is strongly first order, the gauge-dependence appears to be less pronounced than in the generic case. Such a situation occurs either when the gauge coupling is relatively large or when the tree-level singlet-Higgs cubic term acts in concert with small negative mass-squared values at $h = s = 0$ to create a potential barrier at low temperature. Otherwise, when the phase transition is only weakly first-order, or borderline strongly first-order, the gauge-dependence can be drastic regardless of the presence of a cubic term. This dependence may change not only the strength of the phase transition, but also its overall character. In such circumstances, one cannot make a gauge-independent determination of whether the transition is first or second-order, nor can one even determine whether or not the transition comes from a symmetry-preserving vacuum. The explicitly gauge-independent calculation of the critical temperature T_C using the lowest-order result in Ref. [118] can give a rough estimate of the transition temperature T_*, but only when the amount of super-cooling is small[3], which is hard to achieve with a tree-level barrier. A similar gauge-independent calculation of α is

[3]In this case, the onset of nucleation occurs for T very close to T_C

only reasonable when the transition is already known to be strongly first-order.

As emphasized in our earlier work [92], the appearance of gauge-dependence in physical quantities such as T_*, α, and β should engender caution when attempting to draw phenomenological conclusions from computations performed in a specific gauge. In the ideal situation, a gauge-invariant computation using non-perturbative methods would be used to explore various Standard Model extensions that may lead to a first order electroweak phase transition, though a comprehensive exploration is at present prohibitively expensive. In the meantime, various gauge-invariant perturbative techniques, such as the loop expansion [118] or Hamiltonian formulation [122], may at least point to regions of parameter space in a given model where transitions of different character occur. If, as we find for the Abelian Higgs plus singlet model (and as, perhaps, maybe speculatively be a more general pattern) the gauge-dependence of conventional perturbative computations is mitigated by a strongly first order transition triggered by gauge-independent terms, one might expect to find rough agreement with the results of manifestly gauge-invariant analyses. The present study shows, however, that such a conclusion should be carefully qualified on a case-by-case basis.

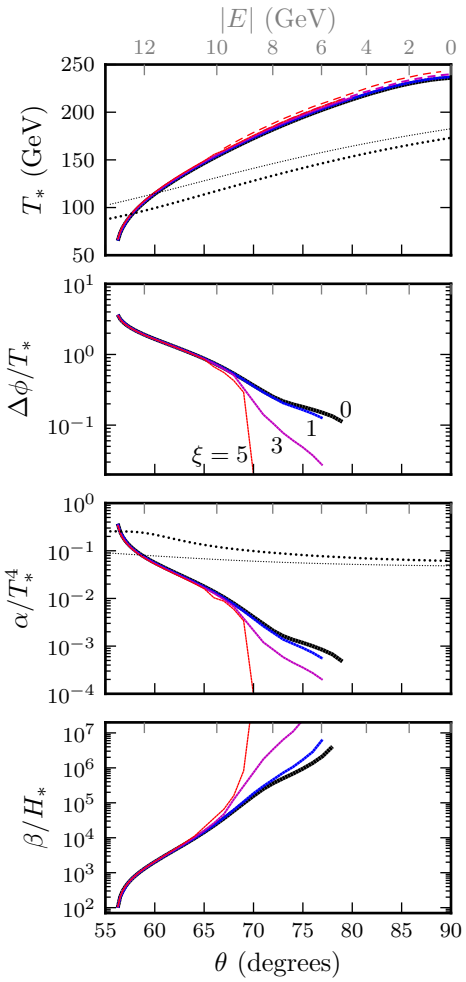

Figure 5.4: Similar to Fig. 5.3, but for case 3 with $g = 0.3$. At $\theta \gtrsim 70°$, the symmetry-breaking transition is second-order for $\xi = 3$ and 5 (dashed lines), followed by a weakly first-order transition. At $\theta \gtrsim 80°$, the symmetry-breaking transition is second order for all plotted values of ξ and the first-order transitions have disappeared. The thick/thin black dotted lines show the gauge-invariant critical temperature and latent heat calculations with/without thermal mass corrections.

Chapter 6

Electroweak Baryogenesis And The Fermi Gamma-Ray Line

In the search for signatures from the annihilation (or the decay) of dark matter particles, a gamma-ray line in the multi-GeV energy range has long been considered a Holy Grail. Given that, in the weakly interacting massive particle (WIMP) paradigm, Galactic dark matter is virtually at rest, the pair annihilation of two particles into a final state consisting of two photons would produce a monochromatic line with an energy exactly corresponding to the particle dark matter mass (or to half its mass in the case of decay). The advent of the Fermi gamma-ray Large Area Telescope (LAT) heralded promise of potentially delivering this smoking gun signal, which would then serve as a beacon for further searches to close in on a well-defined particle dark matter mass.

Despite a null result presented by the LAT collaboration in Ref. [154], independent scholars analyzed the Fermi data employing optimized signal-to-noise regions, unveiling a tantalizing excess localized around 130 GeV[1] and originating from regions including the Galactic center [156, 157]. Subsequent independent analyses confirmed the original claim, typically attributing an even larger level of confidence to the discovery of a monochromatic line in the Fermi-LAT data from the center of the Galaxy [158].

Understandably, the discovery of the line spurred a great deal of interest in the community: a feature in the Earth limb photon events at the same energy was found, albeit with a much lower statistical significance [158]; despite significant efforts in pinpointing possible instrumental or environmental effects that could explain the excess (see e.g. Ref. [159]), at present the line feature appears statistically significant enough to deserve serious consideration.

[1]Recent re-analyses with reprocessed data using "Pass 7 Clean" events put the line at 135 GeV [155], but nothing qualitative changes in the present discussion, where we will assume the line is at 130 GeV.

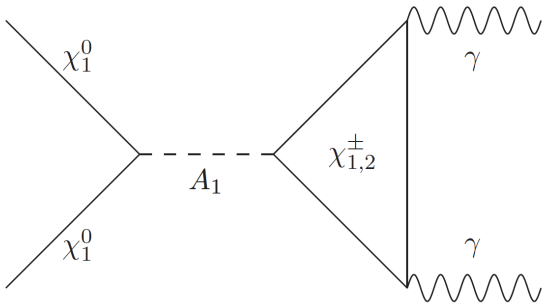

Figure 6.1: The dominant diagram leading to the two-photon pair-annihilation of neutralinos in the NMSSM scenario under consideration in this study.

From a model-building and phenomenological standpoint, the 130 GeV line poses interesting challenges: with default choices for the dark matter density profile in the Galaxy, the required pair-annihilation cross section for dark matter (at rest, i.e. at "zero temperature") into two photons is about $\langle \sigma v \rangle_{\gamma\gamma} \sim 10^{-27} cm^3/s$, much larger than would be expected by suppressing by a factor α^2 the pair annihilation cross section expected for WIMP thermal production in the early universe. Even more problematic is the absence of a continuum gamma-ray signal accompanying the line in the region where the line is detected. This poses the question of how to suppress final states that would generously produce e.g. neutral pions from hadronization showers of strongly interacting particles, or inverse Compton or bremsstrahlung photons from charged leptons.

Simple paradigms for WIMP dark matter fail at explaining the needed features of the 130 GeV line. For example, neutralinos within the minimal supersymmetric extension of the Standard Model (MSSM) feature large suppressions in the pair annihilation into two photons with respect to any other final state, and the required large rate for neutralino pair-annihilation into two photons cannot be accommodated with the right thermal relic abundance [160].

A simple extension to the field content of the MSSM, however, allows for an interesting caveat to both shortcomings mentioned above, as first realized in Ref. [161]: within the next-to-MSSM (or NMSSM, hereafter), an s-channel resonant contribution exists to the annihilation cross section arising from the diagram shown in Fig. 6.1, where two approximately 130 GeV bino-like neutralinos annihilate into a singlet-like pseudoscalar A_1, which then decays into photons via a chargino loop. For $m_{A_1} \sim 260$ GeV, the process is resonant and the resulting cross-section can easily satisfy $\langle \sigma v \rangle_{\gamma\gamma} \sim 10^{-27} cm^3/s$ as required to produce the observed line [156].

The NMSSM possesses the interesting additional possibility of naturally realizing a mechanism known as *electroweak baryogenesis* to produce the observed baryon asymmetry of the universe (BAU) at the electroweak phase transition (EWPT) (for a recent review, see Ref. [162]). The NMSSM framework, in fact, accommodates tree-level cubic couplings entering the relevant scalar effective potential driving the EWPT needed to produce a sufficiently strongly first-order phase transition (this is in turn needed to prevent wash-out of the generated baryon asymmetry in regions of broken electroweak phase), as realized a long time ago [163, 164] and reinforced in recent analyses [165] (see Refs. [144, 145] for similar arguments in related models). Additionally, the NMSSM, like the MSSM, possesses enough room to host the level of CP violation needed for baryogenesis while being consistent with constraints from the non-observation of electric dipole moments (EDMs).

In the present study, we argue that the NMSSM can simultaneously accommodate:

1. a thermal dark matter candidate that can produce the 130 GeV line while being consistent with constraints from other gamma-ray observations and direct detection

searches;

2. a Higgs sector consistent with the recent LHC findings [166, 167];

3. a strongly first-order phase transition as needed by electroweak baryogenesis (for which we calculate in detail the effective finite temperature potential);

4. the generation of the observed baryon asymmetry of the universe at the EWPT, while being consistent with constraints from EDMs.

Requiring all four conditions above forces us to very special corners of the theory's parameter space: the goal of our study is not to explore exhaustively the NMSSM parameter space but, rather, to outline the general implications for the theory parameter space of the four requirements above, and to draw predictions from the regions of parameter space that do satisfy these requirements. As a result, we do not concern ourselves with issues of fine-tuning but, rather, we produce a detailed set of predictions that put this framework for the origin of baryonic and dark matter on very testable grounds. At the same time, we provide benchmarks for corners of the NMSSM theory parameter space where all conditions listed above may be fulfilled.

This paper is organized as follows: in Sec. 6.1 we outline the NMSSM parameter space, detail the neutralino and Higgs sectors, and discuss the phenomenological constraints we implement; Sec. 6.2 discusses the nature of the electroweak phase transition and the constraints that a strongly first-order transition places upon the parameter space; in Sec. 6.3 we discuss the computation of the baryon asymmetry; we conclude in Sec. 6.4

6.1 A 130 GeV Line in the NMSSM

To begin, we review the NMSSM setup, and show how it is possible to hone in on parameters consistent with the 130 GeV gamma-ray signal and with a broad set of additional phenomenological constraints. We follow closely the strategy outlined in Refs. [161, 168] and consider the simplest incarnation of the NMSSM with a scale-invariant, $\mathbb{Z}_3$-symmetric superpotential:

$$W = W_{\rm MSSM}|_{\mu=0} + \lambda \widehat{S}\widehat{H}_u\widehat{H}_d + \frac{\kappa}{3}\widehat{S}^3, \tag{6.1}$$

where hatted quantities denote the corresponding superfields, and where S is a gauge singlet. The soft supersymmetry-breaking Lagrangian is given by

$$-\mathcal{L}^{soft} = -\mathcal{L}^{soft}_{\rm MSSM} + m_S^2\,|S|^2 + \left(\lambda A_\lambda S H_u H_d + \frac{1}{3}\kappa A_\kappa S^3\right) + \text{h.c.} \tag{6.2}$$

After electroweak symmetry breaking (EWSB), the Higgs and singlet fields obtain vacuum expectation values (vevs) of $\langle H_u\rangle \equiv v_u$, $\langle H_d\rangle \equiv v_d$, and $\langle S\rangle \equiv v_s$. As in the MSSM, we denote the ratio of the $SU(2)$ Higgs vevs as $\tan\beta \equiv v_u/v_d$. The singlet vev generates an effective μ-term in the superpotential given by $\mu \equiv \lambda v_s$. We assume that $\lambda, v_s \in \mathbb{R}$ so that μ is real and there is no CP-violation at tree level in the Higgs sector. While CP-violating effects can enter at one-loop from gaugino interactions if we allow $M_{1,2}$ to carry a complex phase, we neglect these contributions when considering radiative corrections to the Higgs sector, since these effects are typically sub-dominant. The six parameters λ, κ, A_λ, A_κ, μ and $\tan\beta$ then determine the tree-level Higgs spectrum after minimizing the scalar potential and solving for the SUSY-breaking Higgs masses.

At this level, deviations from the spectrum of the MSSM originate from the singlet superfield in the superpotential, and are crucial in order to obtain a neutralino consistent

with the 130 GeV gamma-ray signal (without an associated continuum gamma-ray background), with a 125 GeV Higgs, and with successful electroweak baryogenesis. Specifically, the present set-up contains one each of additional neutral CP-even and CP-odd states which enter into the respective Higgs mixing matrices. Complete expressions for the various relevant mass matrices in the NMSSM which match our conventions can be found in, e.g., Ref. [169].

The pseudoscalar mass matrix will be of particular importance; its elements are given, to one-loop order, by [169]

$$\begin{aligned}
\mathcal{M}^2_{P,11} &= \lambda v_s \left(A_\lambda + \kappa v_s\right) \left(\frac{\tan\beta(Q)}{Z_{H_d}} + \frac{\cot\beta(Q)}{Z_{H_u}}\right) \\
\mathcal{M}^2_{P,22} &= 4\lambda\kappa v_u(Q) v_d(Q) + \lambda A_\lambda \frac{v_u(Q) v_d(Q)}{v_s} - 3\kappa A_\kappa v_s \\
\mathcal{M}^2_{P,12} &= \lambda \left(\frac{v_u(Q)^2}{Z_{H_d}} + \frac{v_d(Q)^2}{Z_{H_u}}\right)^{1/2} \left(A_\lambda - 2\kappa v_s\right),
\end{aligned} \tag{6.3}$$

where Q is the relevant SUSY energy scale; $v_{u,d}(Q)$ and $\tan\beta(Q)$ are the Higgs vevs and $\tan\beta$ at the scale Q; and $Z_{H_{u,d}}(Q)$ are wave-function renormalization factors. The matrix $\mathcal{M}_P$ can be diagonalized to obtain the pseudoscalar mass eigenstates A_1 and A_2. As we discuss below, in the present setup A_1 must be singlet-like; the state A_2 will therefore correspond to an MSSM-like pseudoscalar Higgs boson.

In addition to the new degrees of freedom in the Higgs sector, there is an additional Weyl fermion (the "singlino", $\widetilde{S}$), corresponding to the fermionic component of the singlet superfield $\widehat{S}$. This fermionic degree of freedom enters into the neutralino mixing matrix,

whose components are given at tree level by [169]

$$\mathcal{M}_{\chi^0} = \begin{pmatrix} M_1 & 0 & \frac{g_1 v_u}{\sqrt{2}} & -\frac{g_1 v_d}{\sqrt{2}} & 0 \\ . & M_2 & \frac{g_2 v_u}{\sqrt{2}} & \frac{g_2 v_d}{\sqrt{2}} & 0 \\ . & . & 0 & -\mu & -\lambda v_d \\ . & . & . & 0 & -\lambda v_u \\ . & . & . & . & 2\kappa v_s \end{pmatrix}. \tag{6.4}$$

Here, we shall consider the case in which the baryon asymmetry is sourced by CP-violation in the higgsino-gaugino sector [162]. The masses in Eq. (6.4) are therefore generically complex-valued. We will further restrict ourselves to the case of a single complex physical phase, in the wino mass M_2, with all other parameters real[2]. This results in CP-conservation at tree-level in the Higgs sector. Since in our construction the LSP is bino-like throughout all of the parameter space we consider, a CP-violating phase in M_1 would produce large effects on the calculation of the various dark matter properties; we therefore impose $M_1 \in \mathbb{R}$. Eq. (6.4) is diagonalized by the unitary complex matrix $\mathcal{N}$:

$$\mathcal{M}'_{\chi^0} = \mathcal{N}^* \mathcal{M}_{\chi^0} \mathcal{N}^\dagger \tag{6.5}$$

and the neutralino masses are given by

$$\text{diag}\left(m^2_{\chi^0_1},\, m^2_{\chi^0_2},\, m^2_{\chi^0_3},\, m^2_{\chi^0_4},\, m^2_{\chi^0_5}\right) = \mathcal{M}'^{\dagger}_{\chi^0} \mathcal{M}'_{\chi^0}. \tag{6.6}$$

The five neutralinos are admixtures of $\widetilde{B}$, $\widetilde{W}$, $\widetilde{H}_{u,d}$, and $\widetilde{S}$, the lightest of which will be the lightest supersymmetric particle (LSP) in our setup. The chargino mass matrix is simply that of the MSSM, again with a possible complex phase in the wino mass entry, yielding the mass eigenstates $\chi^{\pm}_{1,2}$.

[2]Note that the physical phase we consider here effectively corresponds we to the phase $\phi \equiv \arg(\mu M_2 b^*)$, see e.g. Ref. [170]

Motivated by the lack of a SUSY particle discovery at the LHC, we will typically assume that all sfermions are heavy[3], with $m_{sf} \gtrsim 1.5$ TeV. This effectively decouples them from any process of interest here. As a result, to determine the properties of neutralino dark matter, the electroweak phase transition, and the CP-violating sources for electroweak baryogenesis in the present set-up, one must specify the following nine NMSSM parameters:

$$\lambda, \quad \kappa, \quad A_\lambda, \quad A_\kappa, \quad \mu, \quad \tan\beta, \quad M_1, \quad |M_2| \quad \phi \equiv \arg(M_2). \tag{6.7}$$

As we argue below, many of these parameters are tightly constrained by the phenomenological and observational constraints we impose, in particular by requiring a 130 GeV gamma ray line from resonant neutralino annihilation consistent with other particle and dark matter searches.

Throughout this study, we will assume that the large required pair-annihilation cross-section into two photons, $\langle \sigma v \rangle_{\gamma\gamma} \geq 10^{-27}$ cm^3/s, arises from the on-resonance s-channel annihilation of neutralinos into A_1, which in turn couples to two photons through a chargino loop (see Fig. 6.1). The dominant contribution to the thermally averaged cross-section for this process at zero temperature is given by [160]

$$\langle \sigma v \rangle_{\gamma\gamma} = \frac{\alpha^2 m_{\chi_1^0}^2}{16\pi^3} \left| \sum_{i=1,2} \frac{M_{\chi_i^\pm} m_{\chi_1^0}}{4m_{\chi_1^0}^2 \left(4m_{\chi_1^0}^2 - m_{A_1}^2\right)} \; g_{A_1\chi_1^0} \; g_{A_1\chi_i^\pm} \; F\left(\frac{m_{\chi_1^0}}{m_{A_1}}, \frac{M_{\chi_i^\pm}}{m_{A_1}}\right) \right|^2 \tag{6.8}$$

where the function $F(a,b)$ is defined by

$$F(a,b) \equiv \int_0^1 \frac{dx}{x} \log\left(\left|\frac{4ax^2 - 4ax + b}{b}\right|\right) \tag{6.9}$$

[3]Note that the authors of Ref. [161] considered rather light sleptons to account for the possible discrepancy of the muon $g-2$ with the value predicted by the SM. However, in the present case, such light sleptons can result in large one-loop contributions to the electric dipole moments inconsistent with the constraints discussed in Sec. 6.3.3, barring cancellations.

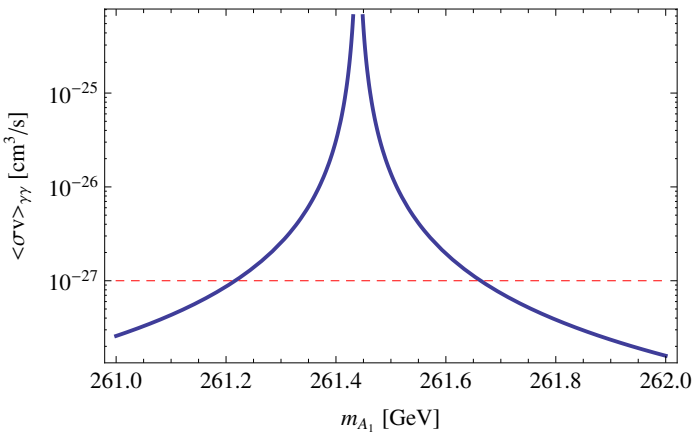

Figure 6.2: The zero-temperature thermally-averaged cross-section times velocity for neutralino annihilation into two photons as a function of the singlet-like pseudoscalar mass m_{A_1} for the EWPT benchmark point discussed in Sec. 6.2: $\lambda = 0.75$, $\kappa = 0.45$, $\tan\beta = 1.7$, $A_\lambda = 545$ GeV, $A_\kappa = -88$ GeV, $\mu = 275.8$ GeV, $M_1 = 143.5$ GeV, and $M_2 = 635.5$ GeV. The red dashed line indicates the lower bound on $\langle\sigma v\rangle_{\gamma\gamma}$ required to produce the 130 GeV Fermi line. Note that decreasing M_1 (thereby increasing μ) will narrow down the resonance.

and the couplings $g_{A_1\chi_1^0}$, $g_{A_1\chi_i^\pm}$ depend on the neutralino, chargino, and CP-odd Higgs diagonalizing matrices. To compute these couplings, we use the Feynman rules found in Ref. [169], appropriately modified to match our conventions for the neutralino and chargino matrices, which contain complex mass entries. This cross-section is plotted as a function of m_{A_1} for a particular choice of parameters, in Fig. 6.2, which clearly shows the narrow resonant structure.

6.1.1 Suitable Higgs and Neutralino Sectors

Given our set-up, we can elucidate the parameter space regions capable of producing the gamma-ray line while satisfying all other dark matter and particle physics constraints. As we show below, requiring a 130 GeV line from resonant neutralino annihilation restricts the NMSSM parameter space to a narrow region in which we can study electroweak

baryogenesis and the electroweak phase transition, in addition to producing unambiguous predictions for several experimentally observable quantities, such as electric dipole moments and dark matter detection rates.

In general, the properties associated with the neutralino LSP depend sensitively on the details of the various parameters involved; this can be appreciated by considering the different benchmark points discussed in Refs. [161, 168]. For example, the annihilation cross-section into photons, Eq. (6.8), is strongly affected by the mass splitting $\left|m_{A_1} - 2m_{\chi_1^0}\right|$, as shown in Fig. 6.2. Correspondingly, other resonant processes, such as the s-channel neutralino pair annihilation into $b\bar{b}$ through A_1, also depend on the mass difference. The details of the various resonant channels significantly affect both the zero-temperature and the finite-temperature annihilation cross sections (the latter being relevant for the calculation of the thermal relic density of dark matter). The amplitudes associated with these processes can however be tuned so that the neutralinos produce a 130 GeV gamma-ray line while satisfying all other indirect detection and relic density constraints, as we show here.

Since we will be concerned with properties of the electroweak phase transition and baryogenesis which do not depend sensitively on the details of the resonance, it is sufficient, for our purposes, to consider the simple parameter choice $A_1 = 2m_{\chi_1^0} = 260$ GeV and proceed to consider the implications for electroweak baryogenesis (a slightly off-resonance value would not at all affect the electroweak phase transition or the resulting baryon asymmetry). From this starting point, we shall dial in the various parameters point-by-point to satisfy all of the phenomenological and observational constraints we describe below.

First and foremost, besides requiring the desired neutralino annihilation structure, demanding a 130 GeV LSP neutralino and the associated 260 GeV singlet-like A_1, we require a 125 GeV SM-like Higgs, in accordance with recent experimental findings from the LHC collaborations [166, 167]. Given our parameter space, the requirements on the bino-like LSP and on A_1 lead us to vary M_1 and A_λ in the range

$$\begin{aligned} 135\text{GeV} &\leq M_1 \leq 145\text{GeV} \\ 150\text{GeV} &\leq A_\lambda \leq 600\text{GeV}. \end{aligned} \tag{6.10}$$

For each point in the M_1, A_λ parameter space, we use the following strategy to choose values for the seven remaining parameters:

1. To obtain a Higgs mass of 125 GeV in the NMSSM without excessive tuning in the stop sector requires relatively large λ and small $\tan\beta$, as seen from the tree-level inequality:

$$m_{h_1}^2 \leq \left(\cos^2 2\beta + \frac{2\lambda^2 \sin^2 2\beta}{g_1^2 + g_2^2}\right) m_Z^2. \tag{6.11}$$

   We take $\tan\beta$ in the range $1.7 \leq \tan\beta \leq 1.8$. In principle λ can be either positive or negative. We focus on positive λ and consider $0.6 \leq \lambda \leq 0.8$ (see, e.g. Ref. [168] for a discussion of the case of $\lambda < 0$). For $|\lambda|$ much smaller than this value, one must rely heavily on stop loops to raise the Higgs mass. Also, λ determines the coupling of neutralinos to A_1, as well as the coupling of A_1 to photons, and so for much smaller $|\lambda|$ the neutralino annihilation cross-section into photons is suppressed. For values $\lambda \gtrsim 0.7$, λ becomes non-perturbative below the GUT scale; this can be remedied by including higher-dimension operators resulting from integrating out new physics which enters below the GUT scale[4] (see e.g. Refs. [171, 172] for explicit implementations of

[4]We will in fact assume that this is the case for our benchmark EWPT point which features $\lambda = 0.75$.

this strategy in similar contexts).

2. The pseudoscalar A_1 must be predominantly singlet-like to be compatible with indirect detection results. The amount of mixing between A_1 and the MSSM-like CP-odd Higgs A_2 is governed by $\mathcal{M}_{P,12}$ in Eq. (6.3) and is minimized for

$$\kappa \approx \frac{\lambda A_\lambda}{2\mu}. \tag{6.12}$$

Given the relatively large values of λ we consider, we take $\kappa \geq 0.3$. For a given choice of κ, the $A_1 - A_2$ mixing will vary point-by-point in the parameter space under consideration. Therefore in some regions of parameter space the lightest pseudoscalar can obtain a large branching ratio into fermions and be incompatible with indirect detection constraints for a given mass difference $\left|m_{A_1} - 2m_{\chi_1^0}\right|$. As mentioned above (and discussed in more detail in Sec. 6.1.2), one can typically dial in the details of the resonance to satisfy these constraints for a given point, however the BAU does not depend sensitively on this tuning.

3. To obtain a lightest neutralino mass of 130 GeV, we must fix μ and M_2 or, equivalently, μ and Δ appropriately, where we define the quantity Δ via

$$M_2 \equiv (|\mu| + \Delta)e^{i\phi}. \tag{6.13}$$

When considering CP-violation in Sec. 6.3, we will typically set the CP-violating phase ϕ to its maximal value, $\sin\phi = 1$, in our calculations to show the maximum extent of the EWB parameter space, although viable regions will typically have phases of $\mathcal{O}(10^{-1})$. In calculating the baryon asymmetry, Δ will govern the strength of the resonant CP-violating source. In considering the higgsino-gaugino CP-violating

sources we will typically take $\Delta = 0$ as an optimistic EWB scenario. Given a particular choice of Δ and ϕ, we fix μ by diagonalizing Eq. (6.4) and solving for μ such that $m_{\chi_1^0} = 130$ GeV (note that we can rewrite $v_s = \mu/\lambda$). This procedure fixes all the relevant parameters in the neutralino and chargino sectors.

4. Finally, to obtain a large photon annihilation cross-section, we need the annihilation channel $\chi_1^0\chi_1^0 \to A_1$ to be near resonance at $T = 0$, which implies $m_{A_1} \approx 260$ GeV. As discussed above and shown in Fig. 6.2, there is a narrow ($\lesssim 1$ GeV) window for which $\langle\sigma v\rangle_{\gamma\gamma}$ is large enough to be compatible with the line. Since the properties of the electroweak phase transition and baryogenesis are not sensitive to the precise value of m_{A_1}, we choose to sit exactly on top of the resonance, i.e. enforce $m_{A_1} = 260$ GeV, by diagonalizing Eq. (6.3) and solving for the appropriate value of A_κ. Therefore, at each point in the parameter space, $\langle\sigma_{\gamma\gamma} v\rangle > 10^{-27}\text{cm}^3/\text{s}$. Once again, the precise mass splitting between A_1 and the LSP can typically be tuned point-by-point to produce the line while providing the correct relic density and satisfying the other indirect detection constraints as described below.

The strategy outlined above is useful to automatically select the regions in the NMSSM producing the tentatively observed 130 GeV gamma-ray line, and provides an efficient way to study the properties of electroweak baryogenesis in these regions by exploring the remainder of the parameter space. Note that we are not concerned with tuning or naturalness in this scenario, since we have narrowed in on this region by demanding consistency with the (tentative!) observation of a gamma-ray line which we postulate to be associated with dark matter pair annihilation.

We shall now use our suitably selected Higgs and neutralino sectors to close in onto electroweak baryogenesis in regions of the NMSSM producing a 130 GeV line. However, we first comment further on the impact of various other dark matter and particle physics constraints on the parameter space under consideration.

6.1.2 Phenomenological Constraints

The NMSSM parameter space of interest features relatively light neutralino, chargino, and Higgs sectors and is thus quite constrained on multiple fronts. Here we highlight the most important constraints on the parameter space and consider their impact on our current set-up. We use `NMSSMTools 3.2.1`[169, 173] and `MicrOmegas 2.4.5`[174, 175] to calculate the various cross-sections and quantities of interest. We summarize in Fig. 6.3 the impact of the constraints we consider here (and that we discuss in detail below) on the relevant parameter space, for the particular choice $\lambda = 0.6$, $\kappa = 0.32$, and $\tan\beta = 1.8$ as an illustrative example. In these calculations, we take M_2 to be real; since the LSP has only a very small wino component across the parameter space, and since the other neutralinos and charginos are significantly heavier than the lightest neutralino, the DM constraints will be largely unaffected by allowing M_2 to be complex. The Higgs couplings are also insensitive to ϕ.

Indirect Dark Matter Detection and Thermal Relic Density

Indirect detection places important constraints on the parameter space in question. In considering $m_{A_1} \approx 2m_{\chi_1^0}$, there will also be a resonant tree-level neutralino annihilation channel into quark-antiquark, and especially $b\bar{b}$, final states, eventually leading to

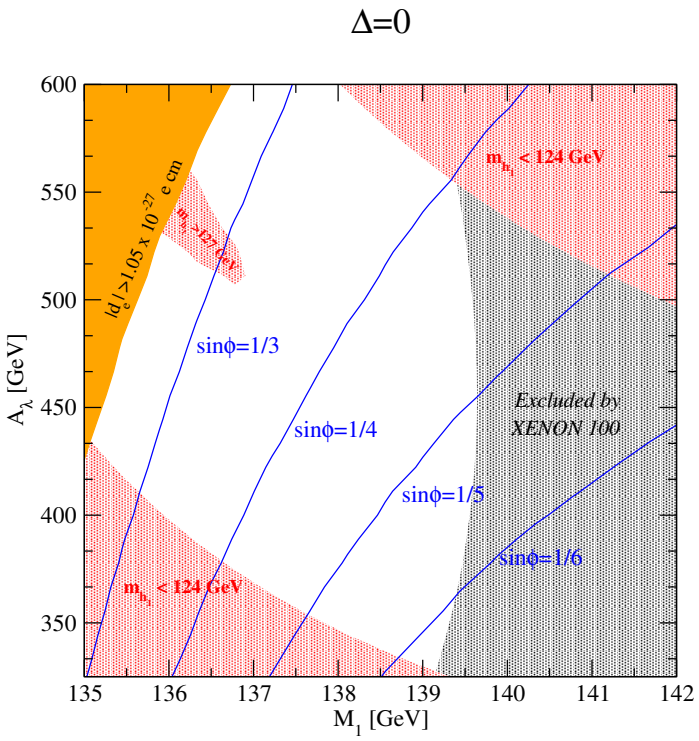

Figure 6.3: An example of the NMSSM parameter space for successful electroweak baryogenesis and a 130 GeV gamma-ray line. Here we take $\lambda = 0.6$, $\kappa = 0.32$, $\tan\beta = 1.8$ and $\Delta = 0$ (so that the CP-violating sources are on resonance), while the rest of the parameters are chosen as described in Sec. 6.1.1 to be consistent with the Fermi line. The gray shaded region is excluded by the XENON100 225 live day results, calculated with the default settings in `MicrOmegas`. Red shaded regions are excluded by measurements of the Higgs mass (although these regions can be shifted around by changing e.g. the squark masses). The orange shaded region is excluded by the non-observation of an electric dipole moment of the electron. The blue contours correspond to points consistent with the observed baryon-to-entropy ratio of the universe for different values of the CP-violating phase ϕ.

gamma rays via hadronization producing neutral ions. The lack of an excess of gamma-rays associated with this emission puts constraints on the branching ratio for neutralino pair-annihilation into, e.g., $b\bar{b}$ [176]. As mentioned above, however, one can generally dial in the mass splitting $\left|m_{A_1} - 2m_{\chi_1^0}\right|$ to obtain both $\langle\sigma_{\gamma\gamma}v\rangle \gtrsim 10^{-27}$ cm^3/s and $\langle\sigma_{b\bar{b}}v\rangle \lesssim 10^{-24}$ cm^3/s as required by Fermi observations [176] of the diffuse gamma ray background (see e.g. the benchmark point in Table 6.1). Additionally, neutralino annihilation into W^+W^-

will receive a contribution at tree-level from the pseudoscalar channel; however, this contribution also typically falls well beneath the 10^{-24} cm^3/s bound from Fermi by adjusting m_{A_1}. Consequently, this tuning allows one to satisfy all continuum gamma-ray constraints [177] while reproducing the observed intensity of the 130 GeV line, something that cannot be done in the MSSM. The parameter space we consider for electroweak baryogenesis can thus be dialed in to agree with indirect detection results without drastically affecting the details of the electroweak phase transition or the generation of the baryon asymmetry.

Similar reasoning applies to the DM thermal relic abundance. For χ_1^0 to be a suitable thermally-produced dark matter candidate, it must be compatible with the bounds on the relic density from WMAP7 [178]: $\Omega_{DM}h^2 = 0.112 \pm .011$. While at zero-temperature the neutralino sits very close to the pseudoscalar resonance, at the freeze-out temperature $T_{\text{f.o.}} \sim m_{\chi_1^0}/20 \approx 6.5$ GeV, the resonance is shifted higher by about 10 GeV for the case of $m_{A_1} = 260$ GeV. This can be seen by evaluating the thermally-averaged center-of-mass (C.O.M.) energy, $\langle s \rangle$, at $T = T_{\text{f.o.}}$, given by

$$\langle s \rangle \simeq 4m_{\chi_1^0}^2 + 6m_{\chi_1^0}T_{\text{f.o.}} \simeq 270 \text{ GeV}. \tag{6.14}$$

However, in evaluating $\langle \sigma v \rangle$ at $T_{\text{f.o.}}$, one integrates over center-of-mass energies, and hence effectively picks up contributions from the resonances, which decrease as one moves $\langle s \rangle$ further away from $4m_{\chi_1^0}^2$. Therefore, as is the case for the zero-temperature cross-sections, by dialing in the detailed neutralino and pseudoscalar masses, as well as the $A_1 - A_2$ mixing, one can typically achieve a total annihilation thermally averaged cross-section of $\langle \sigma v \rangle \sim 3 \times 10^{-26}$ cm^3/s required to obtain the correct relic density.

Previous studies [161, 168] have relied on a sizable higgsino component in the LSP

to drive the relic density down. However, this requires small values of μ which are difficult to reconcile with the most recent direct detection constraints, except in the case of cancellations which can occur for negative μ as exploited in Ref. [168] (we have found it difficult to achieve a strongly first-order EWPT consistent with the 130 GeV line for the $\mu < 0$ case, but it may still be possible). Another possibility is to open a co-annihilation channel by e.g. allowing a light stau [5] with mass near 130 GeV to drive the relic density down. Light staus are not yet significantly constrained by LHC searches and, interestingly, they could provide an explanation of the enhanced Higgs diphoton rate as observed by ATLAS, albeit for large $\tan\beta$ (see e.g. Ref. [179]). We do not pursue these avenues further, but emphasize that we find that the relic density (and the zero-temperature neutralino annihilation cross-sections) can be made to agree with observations in this scenario by tuning or other mechanisms that do not significantly affect the properties of the EWPT nor the calculation of the baryon asymmetry. Consequently, we do not focus on the detailed bounds from indirect detection or the thermal relic abundance point-by-point in our present study of EWB in this scenario, but we do emphasize that these constraints can all be met in principle, as illustrated by a worked-out example in the EWPT benchmark point we show explicitly in Table 6.1.

Direct Detection

Unlike the case of indirect detection and relic density constraints, the bounds from DM direct detection (i.e. the scattering of the lightest neutralino off of nucleons) do not depend sensitively on the details of the resonance, but rather on the composition of the lightest neutralino. This in turn depends on M_1: larger values of M_1 require smaller values

[5] Of course with CP-violation in the gaugino sector one must verify that such a light slepton satisfies constraints from EDMs.

of μ to obtain $m_{\chi_1^0} = 130$ GeV and consequently enhance the spin-independent neutralino-proton cross section.

We require that the LSP satisfy the current upper bound from XENON100 for a 130 GeV WIMP for the spin-independent cross-section[6], $\sigma_{SI} \lesssim 3 \times 10^{-9}$ pb [180]. We show the impact of this constraint on our parameter space in Fig. 6.3: points excluded by XENON100 are shown in the gray shaded region. These bounds are computed assuming default values for the various underlying parameters, such as the quark content of the nucleon, local distribution of dark matter, etc. We employ the `MicrOmegas 2.4.5`[174, 175] package for the calculation of the relevant scattering cross section, and employ the default parameters thereof. As expected, points with smaller μ values, and hence a larger higgsino component in χ_1^0, are ruled out.

We note here that the exclusions are somewhat stronger than those reported in Ref. [161] due to the release of the 2012 XENON results (and consequently the window for m_{A_1} is somewhat more constrained than that in Ref. [161]). Since these limits depend on parameters affected by significant uncertainty, they should also be taken with a grain of salt. For example, by considering the strange quark content of the nucleons near the end of the error bars from Ref. [181] ($\sigma_{\pi N} = 39$ MeV, $\sigma_0 = 43$ MeV), one can push the XENON limits out to allow M_1 up to ~ 145 GeV consistent with the 2012 XENON100 results (see e.g. the EWPT benchmark point in Table 6.1).

[6]We also consider the bound on the spin-dependent cross-section, but the corresponding constraints are much weaker than those on σ_{SI} in our scenario

Higgs Constraints

The lightest CP-even Higgs in our scenario is SM-like. We require that 124 GeV $< m_{h_1} <$ 127 GeV, in agreement with results from ATLAS [167] and CMS [166]. The region of parameter space incompatible with these results is shown in Fig. 6.3 by points within the red shaded regions. We have also checked against constraints from $h_1 \to b\bar{b}$, $\tau\tau$, etc. as implemented in `NMSSMTools 3.2.1`[169, 173]. The couplings of h_1 to the various SM fermions and gauge bosons all fall within $\sim 3\%$ of the corresponding SM predictions, hence well within experimental limits.

The lightest CP-odd Higgs must also be compatible with collider searches. In particular, we verified that the couplings of A_1 to $b\bar{b}$, $\tau\tau$ are small compared to that of the SM-like Higgs for compatibility with LHC results. In the parameter space under consideration, we find that the couplings of A_1 are at most of order 1% of the SM Higgs couplings.

Other Considerations

There are several other constraints which are in fact satisfied over nearly all of the parameter space we consider. Constraints from LEP on light charginos are everywhere satisfied, since charginos are always heavier than the 130 GeV LSP. Also, constraints from B-physics, as implemented in `NMSSMTools 3.2.1`, do not constrain the parameter space since we consider small values of $\tan\beta$. Finally, we have also verified the absence of unphysical global minima of the effective potential for all points we consider, as well as the absence of Landau poles below the GUT scale, with the exception of the EWPT benchmark point, for which we take $\lambda = 0.75$. As discussed above, this issue can be remedied with the modest

assumption of new physics entering below the GUT scale.

In summary, Fig. 6.3 shows that there exist regions of NMSSM parameter space consistent with a 130 GeV gamma-ray line, a 125 GeV SM-like Higgs, and which can satisfy all relevant dark matter and experimental particle physics constraints. We can now proceed to investigate the phenomenology and properties of electroweak baryogenesis in these regions.

6.2 The Electroweak Phase Transition

Successful electroweak baryogenesis requires a strongly first-order electroweak phase transition. In the absence of a strongly first-order transition, $SU(2)$ sphaleron processes, which provide the necessary baryon number violation, are unsuppressed in the broken electroweak phase and tend to wash out any existing generated baryon asymmetry. The strength of the phase transition can be parametrized by the order parameter $\varphi(T_c)/T_c$, where T_c is the critical temperature, defined as the temperature for which the symmetric and broken phases are degenerate[7]. To prevent sphaleron washout requires $\varphi(T_c)/T_c \gtrsim 1$, which we take as the definition of a "strongly first-order" transition[8]. As we will show in this section, this requirement can be readily satisfied in the region of the NMSSM compatible with the 130 GeV gamma-ray line and without relying on a light stop squark, as is instead typically required in the MSSM [183, 30].

The strength of the electroweak phase transition is governed by the finite-temperature

[7]Note that this quantity is not gauge invariant, see e.g. the discussion in Ref. [118, 182].

[8] More precisely, one should actually consider the system at the nucleation temperature, T_n. However, the amount of supercooling in this model is small, and for simplicity we assume that $T_n \approx T_c$ as in previous work.

effective potential, which comprises several parts: the tree-level scalar potential, zero-temperature quantum corrections, finite-temperature quantum corrections, and thermal mass terms. The tree-level potential comes directly from the superpotential (Eq. (6.1)) and the soft supersymmetry-breaking terms (Eq. (6.2)):

$$V_0(h_u, h_d, s) = \frac{1}{32}(g_1^2 + g_2^2)\left(h_u^2 - h_d^2\right)^2 + \frac{1}{4}\kappa^2 s^4 - \frac{1}{2}\lambda\kappa s^2 h_u h_d + \frac{1}{4}\lambda^2\left(h_d^2 h_u^2 + s^2\left(h_d^2 + h_u^2\right)\right) + \frac{\sqrt{2}}{6}\kappa A_\kappa s^3 - \frac{\sqrt{2}}{2}\lambda A_\lambda s h_u h_d + \frac{1}{2}m_d^2 h_d^2 + \frac{1}{2}m_u^2 h_u^2 + \frac{1}{2}m_s^2 s^2. \quad (6.15)$$

The fields h_u, h_d, and s are defined by

$$H_u = \frac{1}{\sqrt{2}}\begin{pmatrix} 0 \\ \\ h_u \end{pmatrix};\ H_d = \frac{1}{\sqrt{2}}\begin{pmatrix} h_d \\ \\ 0 \end{pmatrix};\ S = \frac{1}{\sqrt{2}}s. \quad (6.16)$$

We assume that the scalar fields are real at all temperatures, and we do not consider charged vacua (although we do ensure that the potential is stable in the charged and imaginary directions).

Using $\overline{MS}$ renormalization, the one-loop zero-temperature quantum corrections are

$$V_1(T=0) = \sum_i \frac{\pm n_i}{64\pi^2} m_i^4 \left[\log\left(\frac{m_i^2}{\Lambda^2}\right) - c\right], \quad (6.17)$$

where m_i^2 are the (possibly negative) field-dependent mass-squared values, n_i are their associated number of degrees of freedom, Λ is the renormalization scale, and $c = \frac{1}{2}$ for the transverse polarizations of gauge bosons while $c = \frac{3}{2}$ for their longitudinal polarizations and for all other particles. The plus and minus signs are for bosons and fermions, respectively. The sum over the relevant particles i include all standard model particles (although we ignore fermions lighter than the bottom quark), the physical Higgs and other scalar particles,

their associated Goldstone bosons, the neutralinos and the charginos. We work in Landau gauge where the ghost bosons decouple and need not be included in the spectrum. The one-loop potential contains explicit gauge-dependence which cancels with the implicit gauge-dependence of the vevs at every order in $\hbar$ (for recent discussions of gauge dependence in effective potentials, see e.g. Refs. [118, 92, 182, 184]). As is common practice, we do not consider the effects of the implicit gauge-dependence, and therefore our results will contain gauge artifacts. However, our primary purpose in examining the effective potential is to estimate whether or not a first-order phase transition is possible, and for this purpose a rough calculation with gauge-dependence is acceptable.

We calculate the neutralino masses from Eq. (6.4) above. The scalar mass matrix is given by taking the second derivative of the tree-level potential, but including CP-odd and charged directions. This yields a block-diagonal 10×10 matrix, with blocks consisting of CP-even states (3 degrees of freedom), CP-odd states (3 degrees of freedom), and two blocks of charged Higgses (4 degrees of freedom) (see Appendix 6.5 for details).

The finite-temperature contributions are

$$V_1(T>0) = V_1(T=0) + \frac{T^2}{2\pi^2} \sum_i n_i J_\pm \left(\frac{m_i^2}{T^2} \right), \tag{6.18}$$

where

$$J_\pm(x^2) \equiv \pm \int_0^\infty dy\, y^2 \log \left(1 \mp e^{-\sqrt{y^2+x^2}} \right) \tag{6.19}$$

and again the upper (lower) signs correspond to bosons (fermions). At high temperature, the validity of the perturbative expansion of the effective potential breaks down. Quadratically divergent contributions from non-zero Matsubara modes must be re-summed through

inclusion of thermal masses in the one-loop propagators [96, 97]. This amounts to adding thermal masses to the longitudinal gauge boson degrees of freedom and to all of the scalars (see Appendix 6.5).

The full one-loop effective potential is

$$V(h_u, h_d, s, T) = V_0(h_u, h_d, s) + V_1(T=0) + \frac{T^2}{2\pi^2} \sum_i n_i J_\pm \left(\frac{m_i^2}{T^2} \right) \tag{6.20}$$

where the masses m_i^2 are field-dependent and include thermal mass corrections.

The important qualitative feature of the finite-temperature contribution is that it lowers the effective potential anywhere m_i^2/T^2 is small. To get a strongly first-order phase transition, we need to sharply lower the potential near the symmetric phase without significantly lowering it in the broken phase so that the two phases may be degenerate with a sizable barrier. Therefore, a strongly first-order transition demands either numerous heavy field-dependent particles (such that they are massless in the symmetric phase and heavy in the broken phase), or a tree-level contribution to the barrier separating the two phases. In the standard model, the electroweak phase transition is not strongly first-order. There are no heavy bosons (relative to the Higgs, which sets the relevant scale), and at high temperature the contribution of heavy fermions (top quarks) does not increase the barrier since $J_-(x^2)$ does not contain any cubic terms.

The particle spectrum in the NMSSM may seem somewhat promising, since there are additional heavy masses in the Higgs sector and field-dependent neutralino masses, but these are not enough to guarantee a strong transition. Since many more particles couple to the Higgs than to the singlet, finite-temperature effects drive $\langle h_u \rangle$ and $\langle h_d \rangle$ to zero at temperatures well below the point at which they drive $\langle s \rangle$ to zero. Therefore, s can be large

on either side of electroweak symmetry breaking, and some of the new particle masses that depend on s can be heavy even in the symmetric phase.

However, the NMSSM can succeed in producing a strongly first-order transition through its tree-level contributions. If the transition occurs both in the Higgs and singlet directions simultaneously, and if the singlet vev is non-zero in the electroweak symmetric phase just above the transition, then terms like s^2h^2 and sh^2 both contribute effective cubic terms to the potential which can increase the barrier between the the symmetric and broken phases.

We calculate the phase transition using the software package `CosmoTransitions` [153]. We input the above definition of the effective potential, find the necessary soft-breaking masses that produce desired values for $\tan\beta$ and μ via a minimization procedure, and choose a renormalization scale Λ such that the one-loop minimum does not drastically differ from its tree-level value. This last point requires a certain amount of finesse since the top-quark contribution to the zero-temperature one-loop potential tends to be fairly large. The `CosmoTransitions` package traces the broken electroweak phase up in temperature until it disappears, and then traces the symmetric phase down and checks for an overlap. If there is one, it calculates the temperature of degeneracy (the critical temperature) and the separation between the phases. If there is no overlap, then the transition is necessarily second-order.

The region of the NMSSM consistent with the 130 GeV Fermi line can in fact accommodate a strongly first-order phase transition. The barrier has large tree-level contributions and in particular does not require an additional light scalar. As a proof of principle,

λ	0.75	m_{A_1} [GeV]	261.26
κ	0.45	$m_{\chi_1^0}$ [GeV]	130.72
$\tan\beta$	1.7	$\langle\sigma v\rangle_{b\bar{b}}$ $[cm^3/s]$	3.07×10^{-26}
A_λ [GeV]	545.0	$\langle\sigma v\rangle_{\gamma\gamma}$ $[cm^3/s]$	1.54×10^{-27}
A_κ [GeV]	-88. 0	$\sigma_P^{\rm SI}$ [pb]	2.8×10^{-9}
μ [GeV]	275.8	$\sigma_P^{\rm SD}$ [pb]	1.4×10^{-6}
M_1 [GeV]	143.5	EWPT Properties:	
M_2 [GeV]	635.5	T_c [GeV]	72.3
m_{h_1} [GeV]	126.4	$\varphi(T_c)/T_c$	1.14

Table 6.1: Benchmark Point in the NMSSM with a strongly first-order EWPT and a 130 GeV line. We use a renormalization scale of $\Lambda = 100$ GeV in the effective potential.

we outline a benchmark point consistent with a 125 GeV Higgs, 130 GeV Fermi line, and a strongly first-order electroweak phase transition in Table 6.1. This point has an EWPT at $T_c = 72.3$ GeV with order parameter $\varphi(T_c)/T_c = 1.14$ and is consistent with all other relevant phenomenological constraints [9]. The spin-dependent and –independent neutralino-proton scattering cross-section for the point in Table 6.1 is computed taking $\sigma_{\pi N} = 39$ MeV, $\sigma_0 = 43$ MeV for the strange quark content of the proton and is thus rather optimistic. Also, note that we do not show the relic density for the specified point. Since we are near a resonance, as discussed in Sec. 6.1.2, the relic density calculation should be performed to loop level – something which is not implemented in `MicrOmegas` [10]. However, the asymptotic values of Ωh^2 computed by `MicrOmegas` away from the resonance and the trend of the relic density approaching the pole give us confidence that the correct value of the relic density is achieved in the vicinity of the resonance. Simple analytic estimates also corrob-

[9] As mentioned previously, we can invoke some higher-dimension operators to render λ perturbative below the GUT scale.

[10] We have also found a suspected numerical issue with the `MicrOmegas 2.4.5` calculation of the relic density near the resonance. There is a very sharp increase in the annihilation cross section right above $m_{A_1} = 2m_{\chi_1^0}$ which we believe is unphysical. Since the zero-temperature total-annihilation cross section is of order $\langle\sigma v\rangle \sim 10^{-26}$ cm^3/s, by the arguments in Sec. 6.1.2 the thermally averaged cross-section at freeze-out should be smaller than this since the resonance is effectively shifted. Instead, we find a drop of four orders of magnitude in the relic density which is quite suspect.

orate this conclusion. The total zero-temperature annihilation cross-section (at tree-level) for our benchmark point is $\langle \sigma v \rangle \sim 3 \times 10^{-26}$ cm^3/s, dominated by the resonant $A_1 \to b\bar{b}$ channel. The resonant peak is smoothed out and suppressed at $T_{\text{f.o.}}$ (see Eq. (6.14)), and so one may be concerned that the relic density for this point will be too large. However, we have computed the corresponding finite-temperature thermally-averaged cross-section, and found that adjusting the splitting $|m_{A_1} - 2m_{\chi_0}|$ can indeed provide $\mathcal{O}(10^{-26})$ cm^3/s contributions to $\langle \sigma v \rangle_{T=T_{\text{f.o.}}}$ while still conforming to indirect detection constraints. This adjustment should therefore be sufficient to dial in $\Omega h^2 = 0.11$. If, despite this tuning, the relic density remains too large, one can also introduce e.g. a moderately light stau with $M_{R_3} \sim 200$ GeV to reduce Ωh^2 to its canonical value through co-annihilation. Since $\tan\beta$ is small, the presence of such a light slepton will not affect the properties of the EWPT. Thus, we are confident that a proper one-loop calculation of the relic density for the benchmark point in Table 6.1 will yield a relic density compatible with observation, albeit with some possible minor changes to the parameters or the introduction of a co-annihilation channel which will not substantially affect the EWPT.

Fig. 6.4 shows the field evolution as a function of temperature for the benchmark point in Table 6.1. This makes the location of the phase transitions obvious: first-order phase transitions can happen anywhere there is a discontinuous jump in the vacuum expectation values. A second-order transition, if there were one, would be distinguished by a continuous line of vacuum expectation values with discontinuous first derivatives.

Fig. 6.5 shows the field configuration at the critical temperature of electroweak symmetry breaking. All three fields — s, h_u and h_d — change values when tunneling

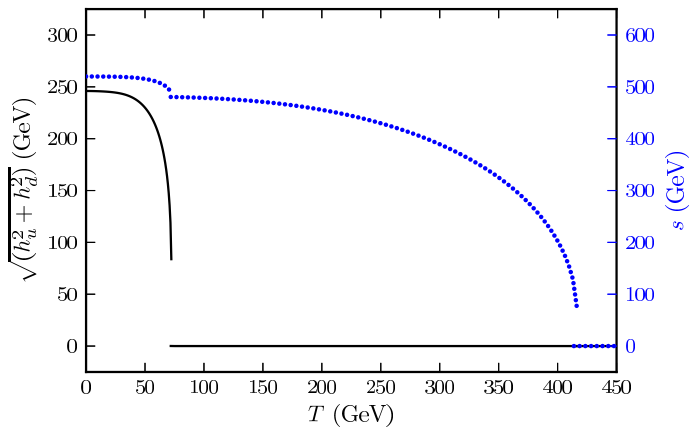

Figure 6.4: The phase structure for the benchmark point with first-order phase transitions. The dotted line gives the temperature-dependent singlet field values, and the solid line gives the temperature-dependent Higgs doublet field values.

from the high-temperature to the low-temperature minimum. We calculate the tunneling direction (denoted by a thick black line) using the `CosmoTransitions` package, where by "tunneling direction" we mean the path through field space that one would travel when crossing a bubble wall. The path is curved in the $s - h_u$ and $s - h_d$ planes, but is approximately straight in the $h_u - h_d$ plane ($\Delta\beta \ll 1$).

While we did not perform a systematic study of the NMSSM parameter space compatible with a strongly first-order transition (see e.g. Refs. [164, 163] for previous work in this direction), there are some common traits between the viable points we have found. Restricting ourselves to the case of positive λ, κ, μ, and A_λ, we find that a strongly first-order phase transition typically requires $\lambda \gtrsim 0.6$, $\kappa \lesssim 0.6$, $A_\lambda \gtrsim 500$ GeV, and $\mu \lesssim 350$ GeV. This seems to be consistent with our intuition: increasing the strength of the cubic terms in the effective potential and decreasing the singlet vev tends to strengthen the transition. Note that, for all the points we considered, the transition tends to happen in two steps: the system transitions away from $\langle s \rangle = 0$ at a high temperature, around 300–400 GeV; while

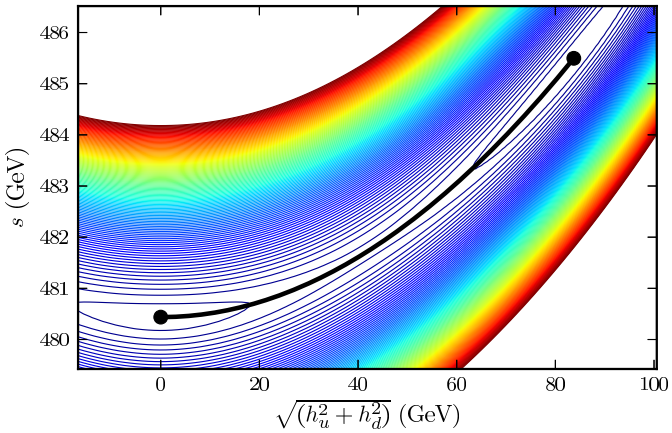

Figure 6.5: A contour plot of the effective potential just below the critical temperature. The electroweak broken minimum is represented by the dot on the upper-right, while the symmetric minimum is on the lower left. The actual tunneling happens along the curved solid black line.

electroweak symmetry breaking happens much later, at a temperature around or below 100 GeV.

6.3 Computing the Baryon Asymmetry

The discussion in the previous section makes it clear that a strongly first-order EWPT can occur in the NMSSM region of parameter space compatible with the Fermi 130 GeV line. We now turn our attention to the CP-violating sources also required for electroweak baryogenesis, and to the detailed requirement of producing the correct amount of baryon asymmetry in the early universe, parametrized by the baryon-to-entropy ratio[11], $Y_B \sim 10^{-10}$. As we show in this section, CP-violating higgsino-gaugino sources can be very efficient in the NMSSM regions of interest and potentially source the observed baryon asymmetry of the universe.

[11]For concreteness and consistency with previous studies, we take $Y_B = 9.1 \times 10^{-11}$

In electroweak baryogenesis, the baryon asymmetry is produced by $SU(2)$ sphalerons acting on a net left-handed chiral density, n_L. To determine n_L, we must solve a set of quantum transport equations for each of the relevant particle densities contributing to the LH charge density. For each of these charge densities, n_i, the Schwinger-Dyson equations yield the continuity equations [66]

$$\frac{\partial n_i}{\partial x_0} + \nabla \cdot j_i(x) = S_i(x). \tag{6.21}$$

The RHS of the above equation contains both CP-conserving and CP-violating contributions. For the case of Dirac fermions, the sources are given by

$$\begin{aligned} S_i(x) = \int d^3z \int_{-\infty}^{x_0} dz_0 \, \mathrm{Tr} \left[\Sigma^{>}(x,z) G^{<}(z,x) - G^{>}(x,z) \Sigma^{<}(z,x) \right. \\ \left. + G^{<}(x,z) \Sigma^{>}(z,x) - \Sigma^{<}(x,z) G^{>}(z,x) \right] \end{aligned} \tag{6.22}$$

where $G^{<,>}$, $\Sigma^{<,>}$ are Green's functions and self-energies, respectively, in the closed time path formalism (see e.g. Ref. [66] for details). We focus here on the case of gaugino-higgsino sources, and compute the quantities $S_{\tilde{H}^{0,\pm}}$ in the Higgs vev-insertion approximation, which we describe in more detail below (see e.g. Ref. [185] for a recent discussion on scalar sources in the MSSM).

6.3.1 The VEV-Insertion Approximation

The CP-violating interactions we consider involve the scattering of higgsinos and gauginos with the spacetime-dependent Higgs vevs in the bubble wall. In what follows we parallel the derivations for the corresponding quantities in the MSSM found in Ref. [66]. We will assume that the necessary CP-violating phase ϕ is that of the wino soft SUSY-breaking mass M_2 (in fact, the relevant phase is the relative phase between $M_{1,2}$ and μ, however

as discussed previously we take μ, M_1 to be real to avoid large spontaneous CP-violating effects in the computation of the various dark matter properties). The part of the NMSSM Lagrangian giving rise to the relevant CP-violating interactions is then given, in terms of four-component spinors, by:

$$\mathcal{L}_{\rm int} \supset -\frac{g_2}{\sqrt{2}}\bar{\Psi}_{\widetilde{H}^0}\left[v_d(x)P_L + e^{i\phi}v_u(x)P_R\right]\Psi_{\widetilde{W}^0} - g_2\bar{\Psi}_{\widetilde{H}^+}\left[v_d(x)P_L + e^{i\phi}v_u(x)P_R\right]\Psi_{\widetilde{W}^+} + h.c. \tag{6.23}$$

where $P_{L,R}$ are the usual projection operators.

The spinors $\Psi_{\widetilde{H}^{0,\pm}}$ satisfy Dirac equations with a spacetime-varying mass $\mu(x)$. As discussed in Sec. 6.2, the profile $\mu(x)$ depends on the detailed properties of the phase transition at each point in parameter space. In the region of interest, however, the singlet vev does not change very significantly during the EWPT. Consequently, even though the variation of the singlet vev was crucial for achieving a strongly first-order phase transition, we ignore its space-dependence here[12] and approximate $\mu(x)$ by its value after the EWPT, $\mu(x) \simeq \mu$. Then the mode expansions for the operators in the Lagrangian Eq. (6.23) are the same as in the MSSM case and so the resulting source from Eq. (6.22) matches that of the MSSM in the vev-insertion approximation:

$$\begin{aligned} S_{\widetilde{H}^\pm}(x) = \int d^4z \sum_{j=A,B} \Big\{ &[g_j(x,z) + g_j(z,x)]\,\mathrm{Re\,Tr}\left[G^{>}_{\widetilde{W}^\pm}(x,z)G^{<}_{\widetilde{H}^\pm}(z,x) - G^{<}_{\widetilde{W}^\pm}(x,z)G^{>}_{\widetilde{H}^\pm}(z,x)\right]_j \\ &+ i\,[g_j(x,z) - g_j(z,x)]\,\mathrm{Im\,Tr}\left[G^{>}_{\widetilde{W}^\pm}(x,z)G^{<}_{\widetilde{H}^\pm}(z,x) - G^{<}_{\widetilde{W}^\pm}(x,z)G^{>}_{\widetilde{H}^\pm}(z,x)\right]_j \Big\} \end{aligned} \tag{6.24}$$

where the sum over A, B is over contributions arising from momentum and mass terms in

[12] The spacetime-dependence of μ can introduce novel sources of CP-violation in the NMSSM; see e.g. Ref. [145]

the spectral function, respectively, and where

$$g_A(x,y) \equiv \frac{g_2^2}{2}\left[v_d(x)v_d(y) + v_u(x)v_u(y)\right] \tag{6.25}$$

$$g_B(x,y) \equiv \frac{g_2^2}{2}\left[v_d(x)e^{-i\phi}v_u(y) + e^{i\phi}v_u(x)v_d(y)\right]. \tag{6.26}$$

The rest of the derivation proceeds as in the MSSM case, i.e. by performing a derivative expansion in $g_{A,B}(x,z)$ around $z = x$. The CP-conserving sources arise from the terms in Eq. (6.24) symmetric under the interchange of $x \leftrightarrow z$ and so appear at zeroth order in this expansion, while the CP-violating sources arise at first-order. In particular, performing the integration for the CP-violating contribution yields

$$S^{\not{C}\not{P}}_{\widetilde{H}^\pm} = \frac{g_2^2}{\pi^2}v(x)^2\dot{\beta}(x)M_2\mu\sin\phi\int_0^\infty \frac{dkk^2}{\omega_{\widetilde{H}}\omega_{\widetilde{W}}}\,\mathrm{Im}\left\{\frac{n_F(\mathcal{E}_{\widetilde{W}}) - n_F(\mathcal{E}^*_{\widetilde{H}})}{(\mathcal{E}_{\widetilde{W}} - \mathcal{E}^*_{\widetilde{H}})^2} - \frac{n_F(\mathcal{E}_{\widetilde{W}}) + n_F(\mathcal{E}_{\widetilde{H}})}{(\mathcal{E}_{\widetilde{W}} + \mathcal{E}_{\widetilde{H}})^2}\right\} \tag{6.27}$$

where $\omega^2_{\widetilde{H},\widetilde{W}} \equiv |\mathbf{k}|^2 + M^2_{\widetilde{H},\widetilde{W}}$ (the masses here include thermal contributions, $\delta_{\widetilde{H},\widetilde{W}}$), $\mathcal{E}_{\widetilde{H},\widetilde{W}} \equiv \omega_{\widetilde{H},\widetilde{W}} - i\Gamma_{\widetilde{H},\widetilde{W}}$ (here the $\Gamma_{\widetilde{H},\widetilde{W}}$ are the thermal widths of the higgsinos and winos in the plasma), and n_F is the Fermi distribution function. The corresponding expressions for the CP-conserving (and neutral higgsino CP-violating) sources can be found in Ref. [66] with the appropriate replacements.

The CP-violating source in Eq. (6.27) exhibits several important properties. The first term of the integrand in Eq. (6.27) is resonant for $M_2 \sim \mu$ as can be appreciated by rewriting the denominator as

$$\mathcal{E}_{\widetilde{W}} - \mathcal{E}^*_{\widetilde{H}} = \sqrt{|\mathbf{k}|^2 + \mu^2 + \delta^2_{\widetilde{H}}} - \sqrt{|\mathbf{k}|^2 + (\mu+\Delta)^2 + \delta^2_{\widetilde{W}}} - i(\Gamma_{\widetilde{W}} + \Gamma_{\widetilde{H}}). \tag{6.28}$$

Thus for a given choice of μ the parameter Δ determines the strength of the resonance, and hence the resulting baryon asymmetry. At finite temperature, $\mu(T)$ will generally be

different from $\mu(T=0)$, since the singlet vev varies with temperature. This can be thought of as providing a finite temperature correction to Δ; we neglect this effect in calculating the baryon asymmetry across the parameter space, as this difference depends sensitively on the finite-temperature effective potential at each point. Note also that the Fermi distribution functions in the numerator result in a suppression of the baryon asymmetry for masses much larger than the electroweak phase transition temperature. As an optimistic estimate, we take $T_c = 140$ GeV in calculating the BAU across the parameter space; the $SU(2)$ sphaleron rate (and hence the overall baryon asymmetry) decreases for lower temperatures. For example, taking $T_c = 100$ GeV will decrease the overall baryon asymmetry by a factor of about 0.7 across the parameter space (i.e. the CP-violating phase $\sin\phi$ at each point would increase by a factor of about 1.4). For our particular benchmark point in Table 6.1, we found a transition around $T_c = 72$ GeV, but the phase transition temperature generally depends quite sensitively on the parameter space point in question and so we do not believe it is necessary for all points to have such low transition temperatures. We encourage the Reader to bear this in mind while interpreting our results.

Other important quantities determining the strength of the CP-violating source are the bubble wall width (L_w), velocity (v_w), and the variation of Higgs vevs across the wall ($\Delta\beta$). This can be seen by approximating the bubble wall profile by a step-function, whence $\dot{\beta} \approx \Delta\beta v_w / L_w$. For the wall width and velocity we choose the canonical MSSM values $L_w = 10/T$ and $v_w = .05$. Previous studies of the bubble wall in singlet extensions of the MSSM suggest typically thinner walls [145], and so we expect that this choice for L_w is a conservative one. Additionally, these parameters will vary depending on the particular

point in the parameter space under consideration. Uncertainties in v_w and L_w are generally expected to induce $\mathcal{O}(1)$ uncertainties in the calculation of the baryon asymmetry [138], which we encourage the Reader to bear in mind. Regarding the quantity $\Delta\beta$, since there is only a small degree of mixing between A_1 and A_2 in our current set-up, we expect $\Delta\beta$ to scale approximately as in the MSSM, i.e. roughly $\Delta\beta \propto 1/m_{A_2}^2$ (in our calculation of $\Delta\beta$ we use the full two-loop results of Ref. [186]). Since m_{A_2} will vary across the parameter space, $\Delta\beta$ will have an important effect on the parameter space available for EWB. For the values of m_{A_2} we consider, $\Delta\beta$ falls in the range $\Delta\beta \sim 10^{-3} - 10^{-4}$. A more detailed study of the bubble wall profile in the NMSSM is required to go beyond the approximations and assumptions here, which we leave for future work.

The other relevant particle number-changing processes (including the triscalar, Yukawa, and CP-conserving relaxation interactions) are also computed in the vev-insertion approximation; expressions for these rates can be found in Refs. [66, 67, 187, 188]. In addition to these MSSM processes, there are new interactions in the NMSSM arising from the singlet and singlino degrees of freedom. In particular, there is a resonant relaxation term (and possible CP-violating source [165]) arising from higgsino-singlino interactions with the Higgs vevs. The relevant part of the Lagrangian is

$$\mathcal{L}_{\rm int}^{\widetilde{S}} = \lambda \left[v_u(x) \widetilde{H}_d^0 \widetilde{S} + v_d(x) \widetilde{H}_u^0 \widetilde{S} \right] \quad + \quad h.c. \tag{6.29}$$

where $\widetilde{H}_{u,d}^0$ and $\widetilde{S}$ correspond to the two-component higgsino and singlino fields. We can rewrite Eq. (6.29) in terms of four-component spinors as

$$\mathcal{L}_{\rm int}^{\widetilde{S}} = \lambda \bar{\Psi}_{\widetilde{H}^0} \left[v_u(x) P_L - v_d(x) P_R \right] \Psi_{\widetilde{S}} \quad + \quad h.c.. \tag{6.30}$$

and follow the methods of Ref. [66] to compute the source. Since we assume that there is

no CP-violation in the singlino sector, Eq. (6.30) results in a resonant chiral relaxation rate for the higgsino chemical potential $\Gamma_{\widetilde{H}^0\widetilde{S}} \equiv \Gamma^{+}_{\widetilde{H}^0\widetilde{S}} + \Gamma^{-}_{\widetilde{H}^0\widetilde{S}}$ where

$$\Gamma^{\pm}_{\widetilde{H}^0\widetilde{S}} = \frac{1}{T}\frac{\lambda^2}{2\pi^2}v(x)^2\int_0^\infty \frac{dkk^2}{\omega_{\widetilde{H}}\omega_{\widetilde{S}}}\,\mathrm{Im}\left\{\left[\mathcal{E}_{\widetilde{S}}\mathcal{E}^*_{\widetilde{H}} - k^2 - M_{\widetilde{S}}\,|\mu|\sin 2\beta\right]\frac{h_F(\mathcal{E}_{\widetilde{S}}) \mp h_F(\mathcal{E}^*_{\widetilde{H}})}{\mathcal{E}_{\widetilde{S}} - \mathcal{E}^*_{\widetilde{H}}}\right.$$
$$\left. + \left[\mathcal{E}_{\widetilde{S}}\mathcal{E}_{\widetilde{H}} + k^2 + M_{\widetilde{S}}\,|\mu|\sin 2\beta\right]\frac{h_F(\mathcal{E}_{\widetilde{S}}) \mp h_F(\mathcal{E}_{\widetilde{H}})}{\mathcal{E}_{\widetilde{S}} + \mathcal{E}_{\widetilde{H}}}\right\} \tag{6.31}$$

and where the various quantities are defined analogously to those in Eq. (6.27). The singlino mass given by

$$M^2_{\widetilde{S}} = 4\kappa^2\mu^2/\lambda^2 + \delta^2_{\widetilde{S}} \tag{6.32}$$

(here $\delta_{\widetilde{S}}$ is the singlino thermal mass), and the quantity h_F is defined as

$$h_F(x) = \frac{e^{x/T}}{\left(e^{x/T}+1\right)^2}. \tag{6.33}$$

Since we consider moderate values of λ, we take $\Gamma_{\widetilde{S}} \simeq 0.001T$ for the singlino width. The denominator of the first term in Eq. (6.31) has the same resonant structure as in Eq. (6.28) and is the most significant contribution to the transport equations from the singlino, tending to reduce the resulting charge density. Given our choices for λ and κ in Fig. 6.3, the relaxation rate $\Gamma_{\widetilde{H}^0\widetilde{S}}$ is near resonance in this region since $M_{\widetilde{S}} \sim \mu$. We account for this higgsino-singlino resonant relaxation in our computation of the baryon asymmetry, but do not consider the other non-resonant singlet/singlino interactions, as they are subdominant.

6.3.2 Solving the Transport Equations

With the sources contributing to the RHS of Eq. (6.21) for the various charged current densities in place, we compute the baryon asymmetry point-by-point across the 130 GeV line parameter space described in Sec. 6.1.1 for $\lambda = 0.6$, $\kappa = 0.32$, and $\tan\beta = 1.8$ as

an example. We do so by solving the system of transport equations to determine the LH charge density n_L, assuming a strongly first-order EWPT and that the $SU(2)$ sphaleron rate Γ_{ws} is slow compared to the other particle number-changing rates. Then, given $n_L(z)$, the baryon number density results from the integral of n_L over the unbroken phase,

$$n_B = \frac{-3\Gamma_{ws}}{v_w}\int_{-\infty}^{0} dz\ n_L(z) e^{\frac{15\Gamma_{ws}}{4v_w}z}, \tag{6.34}$$

where z is the comoving distance away from the bubble wall (neglecting the curvature of the wall and taking $z<0$ to be the symmetric phase).

To determine n_L, we work under the set of assumptions detailed in Refs. [66, 138], and in particular assuming "super-equilibrium" (i.e. the equality of the chemical potentials) for the Higgs and higgsino densities [67], allowing us to define a common charge density for both. Given the condition of Higgs-higgsino super-equilibrium and assuming that the sfermions are heavy, one can show that the relevant charge densities we must keep track of are those corresponding to the Higgs/higgsinos (H), the right-handed tops (T), and the left-handed third-generation quarks (Q). The transport equations then read

$$\partial_\mu Q^\mu = -\Gamma_{yt}\left(\frac{Q}{k_Q}-\frac{T}{k_T}+\frac{H}{k_H}\right)-\Gamma_{mt}\left(\frac{Q}{k_Q}-\frac{T}{k_T}\right)-2\Gamma_{ss}\left(2\frac{Q}{k_Q}-\frac{T}{k_T}+9\frac{Q+T}{k_B}\right) \tag{6.35}$$

$$\partial_\mu T^\mu = \Gamma_{yt}\left(\frac{Q}{k_Q}-\frac{T}{k_T}+\frac{H}{k_H}\right)+\Gamma_{mt}\left(\frac{Q}{k_Q}-\frac{T}{k_T}\right)+\Gamma_{ss}\left(2\frac{Q}{k_Q}-\frac{T}{k_T}+9\frac{Q+T}{k_B}\right) \tag{6.36}$$

$$\partial_\mu H^\mu = -\Gamma_{yt}\left(\frac{Q}{k_Q}-\frac{T}{k_T}+\frac{H}{k_H}\right)-\Gamma_h\frac{H}{k_H}+S_{\tilde{H}}^{C\!\!\!/P}. \tag{6.37}$$

Here, $\Gamma_{mt,h}$ are chiral relaxation rates (including the contribution from the higgsino-singlino-vev interaction), active only in the bubble wall[13] and broken EW phase, Γ_{yt} are Yukawa

[13]For simplicity, in solving the transport equations we assume a step-function profile for the Higgs vevs in the bubble wall.

interaction rates [188], Γ_{ss} is the $SU(3)$ sphaleron rate (responsible for generating densities of first- and second-generation quarks), and the k_is are statistical factors relating the charge densities n_i to the corresponding chemical potential μ_i. We solve Eqs. (6.35)-(6.37) utilizing the diffusion approximation discussed in Ref. [66]. The LH charge density entering into Eq. (6.34) is then given to good approximation by the relation

$$n_L(z) = 5Q(z) + 4T(z). \tag{6.38}$$

While we are primarily concerned with heavy sfermions to avoid large EDM contributions, in solving the transport equations numerically we take the RH stop to be moderately light (~ 200 GeV, and hence also in super-equilibrium) to show the maximum extent of the compatible parameter space before encountering a sizable "Shaposhnikov suppression" [189] that arises from the $SU(3)$ sphalerons when both T and Q correspond entirely to densities of SM fermions (see Refs. [29, 138, 190] for previous work also implementing this strategy). As long as it is not too light, the RH stop mass is not crucial to the phenomenology (in fact, Ref. [161] assumed a RH stop around 300 GeV), whereas this suppression depends quite sensitively on the mass of the stops. In calculating the EDM limits below, however, we assume both stops are heavy, again to show the maximal extent of the parameter space under consideration. Of course a light stop would introduce sizable one-loop contributions to the various EDMs and so one cannot take the stop to be too light without also significantly reducing the CP-violating phase in M_2, or without relying on cancellations. This means that our results for the baryon asymmetry and EDMs will be idealized, while a more realistic stop spectrum will likely tighten the EDM constraints, either by increasing the one-loop stop contribution to the EDMs or by increasing the CP-violating phase to

account for the suppressed baryon asymmetry.

We show contours corresponding to the observed value of the baryon-to-entropy ratio across the 130 GeV line parameter space on the resonance ($\Delta = 0$) for different values of the CP-violating phase ϕ in Fig. 6.3, calculated as described above. We have checked that even in solving the transport equations with both stops heavy (~ 1.5 TeV), and hence substantial Shaposhnikov suppression, there remain regions compatible with the observed baryon asymmetry of the universe, a 130 GeV gamma-ray line, and all other relevant constraints.

In interpreting our results, the reader should bear in mind that there are several uncertainties present in our calculation of the baryon asymmetry. As mentioned, the micro-physical properties of the EW bubble wall and details of the electroweak phase transition (L_w, v_w, $\Delta\beta$, T_c, etc) can significantly affect the calculation of n_L and Y_B (see e.g. Ref. [138] and references therein for a more detailed discussion of these effects). Also, there are several other frameworks for calculating the baryon asymmetry [191, 27, 192, 58, 193, 194], with results that can differ by up to an order of magnitude from one another (for a review of these different approaches, see Ref. [162]). Additionally, there are other possible sources of CP-violation in the NMSSM that could contribute to the BAU in this scenario. For example, allowing a relative phase between λ and κ would allow resonant CP-violating singlino sources arising from Eq. (6.30) which in fact would be close to resonant (see Ref.[165] for a discussion of singlino-driven EWB in the NMSSM).

Despite these issues and caveats, Fig. 6.3 suggests that resonant CP-violating higgsino-gaugino sources can be very efficient in the region of the NMSSM consistent with

a 130 GeV gamma-ray line. Even if we had over-estimated the baryon asymmetry by an order of magnitude, there could still be regions consistent with both the Fermi line, the observed BAU, constraints from electric dipole moments (which we discuss below), and DM direct detection, provided more optimistic choices for the strange quark content of the proton or the local distribution of dark matter. For example, taking the values of σ_0, $\sigma_{\pi N}$ we considered for the EWPT benchmark point pushes out the allowed values of M_1 in Fig. 6.3 out to about 145 GeV, which would allow a factor of ten over-estimation of the BAU consistent with EDM constraints.

6.3.3 EDM Constraints

The NMSSM contains several possible sources of CP-violation beyond those in the MSSM: CP-violation in tree-level parameters λ, κ, and μ; CP-violation in soft-breaking terms A_λ and A_κ; and additional effects coming from the mixing between the two CP-odd eigenstates A_1 and A_2. However, in our setup we assume no CP-violation in the tree-level Higgs sector and very little mixing between A_1 and A_2 (A_1 must be mostly singlet-like, as explained above). Therefore, the electric dipole moment calculations reduce to those in the MSSM.

We use the package `CPSuperH` [195] to calculate the electric dipole moments of the electron, the neutron, and the mercury atom, which have current experimental limits of $|d_e| < 1.05 \times 10^{-27} e$ cm [196] (via the YbF molecule), $|d_n| < 2.9 \times 10^{-26} e$ cm [197], and $|d_{Hg}| < 3 \times 10^{-29} e$ cm [198]. The neutron and the Mercury atom generally provide extremely strong limits on CP-violating physics, but they are most sensitive to chromo-EDMs and CP-violation involving colored particles. We have no chromo-EDMs in this

model, so the electron EDM provides, here, the strongest constraint. All one-loop EDMs are suppressed by the heavy sfermion masses. The dominant two-loop contribution comes from the Barr–Zee diagram containing a chargino loop.

For each point in the parameter space of Fig. 6.3, we calculate the EDMs using the value of ϕ that produces the proper baryon abundance. Except for ϕ, most of the parameters necessary for calculating the EDMs vary little over the plotted region, so the EDMs are most sensitive to ϕ and the corresponding iso-level curves follow similar trajectories. The small region in the upper-left with $\sin\phi \gtrsim 0.37$ has $|d_e| > 1.05 \times 10^{-27} e$ cm, and is thus ruled out by experiment. The smallest EDM in this region, corresponding to $\sin\phi \approx \frac{1}{6}$, is $|d_e| = 5.1 \times 10^{-28}$. This is well within the anticipated sensitivity of next-generation EDM experiments (for a review, see, *e.g.*, Ref. [199]), which have the potential to either rule out or lend credence to this baryogenesis scenario.

6.4 Summary

The present study reaffirms that the NMSSM framework (and indeed other singlet-extensions of the Higgs sector [200]) can provide a viable explanation of the 130 GeV Fermi gamma-ray line in terms of resonant neutralino annihilation through a pseudoscalar into photons. Agreement with observation and with the relevant constraints is realized in the NMSSM for a bino-like LSP (dictating that $M_1 \sim 130$ GeV), with relatively large λ, moderate μ, and with A_1 predominantly singlet-like to avoid indirect detection constraints on continuum photons. While there are many independent constraints on this scenario, currently there remains a substantial amount of parameter space consistent with the gamma-

ray line and in agreement with the various dark matter and particle physics constraints.

Here we have shown that the parameter space consistent with the Fermi line in the NMSSM is also promising for electroweak baryogenesis. In particular, the relatively large values of λ typically considered tend to bolster the cubic term in the finite-temperature effective potential in the direction of electroweak symmetry breaking, leading to a strongly first-order electroweak phase transition in parts of the parameter space. Additionally, the moderate values of μ ensure that the singlet vev is not too far from the EW scale, again tending towards a strongly first-order transition. We illustrated this in Sec. 6.2 by providing a benchmark point consistent with the 130 GeV line and a strongly first-order EWPT, and in agreement with all other relevant phenomenological constraints. While we only studied in detail one particular point as a proof of principle, we expect a more systematic study of the NMSSM parameter space to uncover many other regions consistent with the line and a strongly first-order EWPT.

Not only does the parameter space consistent with the line support the possibility of a strongly first-order transition, it can also provide an efficient source for CP-violation that gives rise to the observed baryon-to-entropy ratio of the universe. Resonant higgsino-gaugino sources can be very efficient here due to the moderate values of $M_{1,2}$ and μ required to produce the line. In particular, allowing for a CP-violating phase in M_2 does not strongly affect the line or the dark matter phenomenology, but it can produce the observed BAU with $\sin\phi$ small enough to be consistent with electric dipole measurements, as shown in Sec. 6.3 and Fig. 6.3. While we focused on the higgsino-wino sources in the present study for the sake of illustration, similar resonant CP-violating sources arising from other interactions

can be active in the same regions of parameter space by similar reasoning. For example, if one allows for M_1 to carry a complex phase, resonant bino-higgsino sources can be very efficient as well. This may be of particular interest in the case of negative μ whereby $|\mu|$ can be taken as low as 140 – 150 GeV (and thus potentially very close to this resonance) while in agreement with direct detection constraints [168]. A careful study of the effect of a CP-violating phase in M_1 on the line and dark matter properties would be necessary to assess whether such a scenario is possible, but we expect it is since EDM measurements dictate that the CP-violating phase is necessarily small. Also, singlino-higgsino sources can in principle be efficient in this region as well, provided a relative phase between λ and κ [165], again due to the moderate values of the singlino mass (see Eq. (6.32)) and μ in this scenario. These other sources would be especially important for points such as our EWPT benchmark which features a rather heavy wino but lighter bino and singlino[14].

An interesting feature of our scenario is that the relevant parameter space will be conclusively tested in the near future by modest improvements in various experimental efforts. The moderate values of μ we consider result in rather large spin-independent neutralino-nucleon cross-sections which continue to be probed by direct detection experiments. The relatively large values of λ, as required for a large $\langle\sigma v\rangle_{\gamma\gamma}$, combined with the large A_λ and moderate values of κ necessary for a strongly first-order EWPT, tend towards a significant coupling of A_1 to e.g. $b\bar{b}$ and so will be tested by modest improvements in indirect detection experiments. Additionally, the CP-violating phase(s), required to source the left-handed charge density for the $SU(2)$ sphalerons, will be well within reach of various

[14]Note that non-resonant wino-higgsino sources, such as those considered in Refs. [191, 27, 190] can also potentially provide the necessary CP-violation for our particular EWPT benchmark point.

future EDM experiments (see e.g. Ref. [185] for a related discussion). The whole scenario will also continue to be tested by ongoing measurements of Higgs couplings and searches for other particles at the LHC.

Of course the viability of the 130 GeV line scenario in the NMSSM or any other SM extension hinges on the persistence of the line in the Fermi data and on a dark matter interpretation of these results. If the line is indeed due to resonant dark matter annihilation, this work shows that the NMSSM framework can potentially explain the origin of both the baryonic and dark matter in our universe.

6.5 Appendix: Scalar Mass Terms

We present here the scalar mass terms used in the calculation of the finite-temperature effective potential. These are simply the second-derivatives of the full 10-parameter potential, but simplified such that only 3 of the parameters (h_u, h_d and s) are non-zero. Each subscript denotes a partial derivative with respect to that field. Primed subscripts are derivatives with respect to the imaginary field components, and $\tilde{u}$ and $\tilde{d}$ denote derivatives in the up- and down-type charged directions. The tree-level masses are just the mass eigenvalues of the following matricies.

$$M_{uu}^2 = \tfrac{1}{2}\lambda(h_d^2 + s^2) + \tfrac{1}{8}(g_1^2 + g_2^2)(3h_u^2 - h_d^2) + m_u^2 \tag{6.39}$$

$$M_{dd}^2 = \tfrac{1}{2}\lambda(h_u^2 + s^2) + \tfrac{1}{8}(g_1^2 + g_2^2)(3h_d^2 - h_u^2) + m_d^2 \tag{6.40}$$

$$M_{ss}^2 = \tfrac{1}{2}\lambda(h_u^2 + h_d^2) + 3\kappa^2 s^2 - \lambda\kappa h_u h_d + m_s^2 + \sqrt{2}\kappa A_\kappa s \tag{6.41}$$

$$M_{ud}^2 = \lambda^2 h_u h_d - \tfrac{1}{2}\lambda\kappa s^2 - \tfrac{1}{4}(g_1^2 + g_2^2)h_u h_d - \tfrac{1}{\sqrt{2}}\lambda A_\lambda s \tag{6.42}$$

$$M_{us}^2 = \lambda^2 h_u s - \lambda\kappa h_d s - \tfrac{1}{\sqrt{2}}\lambda A_\lambda h_d \tag{6.43}$$

$$M_{ds}^2 = \lambda^2 h_d s - \lambda\kappa h_u s - \tfrac{1}{\sqrt{2}}\lambda A_\lambda h_u \tag{6.44}$$

$$M_{u'u'}^2 = \tfrac{1}{2}\lambda(h_d^2 + s^2) + \tfrac{1}{8}(g_1^2 + g_2^2)(h_u^2 - h_d^2) + m_u^2 \tag{6.45}$$

$$M_{d'd'}^2 = \tfrac{1}{2}\lambda(h_u^2 + s^2) + \tfrac{1}{8}(g_1^2 + g_2^2)(h_d^2 - h_u^2) + m_d^2 \tag{6.46}$$

$$M_{s's'}^2 = \tfrac{1}{2}\lambda(h_u^2 + h_d^2) + \kappa^2 s^2 + \lambda\kappa h_u h_d + m_s^2 - \sqrt{2}\kappa A_\kappa s \tag{6.47}$$

$$M_{u'd'}^2 = \tfrac{1}{2}\lambda\kappa s^2 + \tfrac{1}{\sqrt{2}}\lambda A_\lambda s \tag{6.48}$$

$$M_{u's'}^2 = -\lambda\kappa h_d s + \tfrac{1}{\sqrt{2}}\lambda A_\lambda h_d \tag{6.49}$$

$$M_{d's'}^2 = -\lambda\kappa h_u s + \tfrac{1}{\sqrt{2}}\lambda A_\lambda h_u \tag{6.50}$$

$$M_{\tilde{u}\tilde{u}}^2 = \tfrac{1}{2}\lambda^2 s^2 + \tfrac{1}{8}(g_1^2 + g_2^2)(h_u^2 - h_d^2) + \tfrac{1}{4}g_2^2 h_d^2 + m_u^2 \tag{6.51}$$

$$M_{\tilde{d}\tilde{d}}^2 = \tfrac{1}{2}\lambda^2 s^2 + \tfrac{1}{8}(g_1^2 + g_2^2)(h_d^2 - h_u^2) + \tfrac{1}{4}g_2^2 h_u^2 + m_d^2 \tag{6.52}$$

$$M_{\tilde{u}\tilde{d}}^2 = -\tfrac{1}{2}\lambda^2 h_u h_d + \tfrac{1}{2}\lambda\kappa s^2 + \tfrac{1}{4}g_2^2 h_u h_d + \tfrac{1}{\sqrt{2}}\lambda A_\lambda s \tag{6.53}$$

There is a second matrix for the charged Higgs, but the two are identical except for a change of sign in the off-diagonal term which does not affect its eigenvalues.

In the high-temperature approximation, the thermal mass terms come from the quadratic piece of the one-loop finite-temperature contributions to the effective potential. The scalar thermal masses include contributions from all particles with field dependent masses, and they get added to each of the diagonal terms in the mass matrix. They are:

$$\Pi_u = T^2 \left[\tfrac{1}{8}\left(g_1^2 + 3g_2^2\right) + \tfrac{1}{4}\lambda^2 + \tfrac{1}{4}y_t^2\right] \tag{6.54}$$

$$\Pi_d = T^2 \left[\tfrac{1}{8}\left(g_1^2 + 3g_2^2\right) + \tfrac{1}{4}\lambda^2 + \tfrac{1}{4}y_b^2\right] \tag{6.55}$$

$$\Pi_s = \tfrac{1}{2}T^2\left(\lambda^2 + \kappa^2\right). \tag{6.56}$$

The longitudinal polarizations of the gauge bosons also receive thermal mass corrections. At finite temperature, the gauge boson mass mixing is

$$M^2_{gauge-long} = \frac{h_u^2 + h_d^2}{4}\begin{pmatrix} g_2^2 & & & \\ & g_2^2 & & \\ & & g_2^2 & g_1 g_2 \\ & & g_1 g_2 & g_1^2 \end{pmatrix} + T^2 \begin{pmatrix} \frac{5}{2}g_2^2 & & & \\ & \frac{5}{2}g_2^2 & & \\ & & \frac{5}{2}g_2^2 & \\ & & & \frac{13}{6}g_1^2 \end{pmatrix}. \tag{6.57}$$

Again, we have ignored the contributions from the sfermions, because they are much too heavy to factor into the high-temperature corrections. For more information on thermal masses in the supersymmetric theories, see ref. [201].

Chapter 7

Conclusion

In this dissertation I have explored finite-temperature phase transitions in the early universe, with a focus on the theory and phenomenology of the electroweak phase transition. The key findings are as follows:

- Chapter 2 described the thermodynamics of strongly first-order phase transitions and the possible effect that one would have on the abundance of thermal relics. A very strongly first-order transition, driven by, e.g., a large number of extra heavy degrees of freedom coupled to the Higgs, would have caused a large amount of reheating at the end of the phase transition and/or a long period of phase coexistence at constant temperature. The Universe's scale factor would have increased without an associated drop in temperature, so thermal relics would have effectively been diluted. In the most optimistic scenario, the dilution is of order 100 (that is, the Universe's volume increases by a factor of 100 without decreasing in temperature). In more reasonable scenarios, the dilution could be a factor of a few. An analysis of MSSM neutralino

dark matter models showed that a large class of models which would have otherwise overproduced the Universe's dark matter content can be salvaged by the dilution from a strongly first-order phase transition.

- Chapter 3 presented a numerical package (CosmoTransitions) which computes various aspects of phase transitions given a tree-level potential and mass spectrum. It calculates the minima of a one-loop effective potential as a function of temperature, determines the critical temperature of any phase transitions (the temperature at which two phases have equal free energy), finds the bubble wall profiles which describe nucleated pockets of stable vacuum at different temperatures, and from this finds the nucleation rates and the amount of supercooling in the high-temperature phases. Importantly, CosmoTransitions presents a novel way for calculating the bubble wall solution in multiple field dimensions using a method of path deformation. Note that this aspect of the package can be used at both zero and finite temperature.

- Chapter 4 demonstrated the significant gauge problem in finite-temperature effective potentials. Finite-temperature effective potentials contain both explicit and implicit gauge dependence. The explicit gauge dependence is removed by working to fixed loop-order in the effective potential, but the residual gauge dependence of the vacuum expectation value remains. We calculated expected gravitational wave spectrums created during the electroweak phase transition from a simple toy Abelian-Higgs model in different gauges, and showed that the gauge choice can have dramatic effect upon the calculation of physical observables. The gauge choice itself is, of course, not physical, so this should be thought of as an extra source of theoretical uncertainty.

- Chapter 5 directly extended the work in chapter 4 to include effects from an extra scalar singlet. A cubic term in the singlet-Higgs interaction can lead to a more strongly first-order phase transition at tree level, and thus mitigate the gauge-dependence problem. However, we found that the gauge dependence remains significant except in very special circumstances.

- Chapter 6 showed how the NMSSM can simultaneously explain the baryon asymmetry of the universe via electroweak baryogenesis, provide a dark matter particle which matches the 130 GeV gamma-ray line seen by the Fermi space telescope in the galactic center, and produce a Standard Model-like Higgs in the observed mass range. The singlet contribution to the effective potential allows for the strongly first-order phase transition, while production of a 130 GeV gamma-ray line is possible by virtue of both a relatively light pseudoscalar Higgs sector with a small degree of mixing (which yields efficient s-channel resonant neutralino annihilation consistent with indirect detection constraints) and the moderate values of μ required to obtain a bino-like LSP consistent with the line.

In addition to the work presented in this document, I worked on several other projects during my graduate studies. I published one paper with Lorenzo Ubaldi and Stefano Profumo on scalar singlet dark matter and the possibility of vacuum decay [91]; and I published two further papers on supersymmetric baryogenesis with Stefano Profumo and Jonathan Kozaczuk [185, 190] (the first of which also included Michael Ramsey-Musolf as a coauthor). More recently, I have started working on inflationary cosmology. With Anthony Aguirre, Matt Johnson and Hiranya Peiris, I am simulating collisions between bubble

universes in an eternal inflation paradigm. I use a modified version of the CosmoTransitions package (now including gravitational effects) to calculate the initial conditions for the bubbles, and a custom code to evolve the bubbles forward in time. The grand goal of the project is to accurately predict how a collision will appear on the cosmic microwave background radiation. I will be continuing this work next year as post-doctoral fellow. With Tom Banks and TJ Torres, I have been trying to calculate two- and three-point scalar and tensor correlation functions in a de Sitter Universe using only the de Sitter symmetries. The goal here is to compare predictions of Holographic Space Time with generic slow-roll inflation models. Finally, I plan to continue studying the electroweak phase transition in the NMSSM with Stefano, Jonathan, and Laurel Stephenson-Haskins (a new addition to our group). We would like to do a more systematic analysis of the phase transition in a broad range of parameter space and gain a better understanding of how the bubble wall profiles evolve after the initial nucleation events.

Bibliography

[1] **Planck Collaboration** Collaboration, P. Ade *et al.*, "Planck 2013 results. XVI. Cosmological parameters," arXiv:1303.5076 [astro-ph.CO].

[2] G. Steigman, "Primordial Nucleosynthesis in the Precision Cosmology Era," *Ann. Rev. Nucl. Part. Sci.* **57** (2007) 463–491, arXiv:0712.1100 [astro-ph].

[3] H. Baer and X. Tata, *Weak scale supersymmetry: From superfields to scattering events*. Cambridge University Press, 2006.

[4] **WMAP Collaboration** Collaboration, E. Komatsu *et al.*, "Five-Year Wilkinson Microwave Anisotropy Probe (WMAP) Observations: Cosmological Interpretation," *Astrophys. J. Suppl.* **180** (2009) 330–376, arXiv:0803.0547 [astro-ph].

[5] **WMAP Collaboration** Collaboration, J. Dunkley *et al.*, "Five-Year Wilkinson Microwave Anisotropy Probe (WMAP) Observations: Likelihoods and Parameters from the WMAP data," *Astrophys. J. Suppl.* **180** (2009) 306–329, arXiv:0803.0586 [astro-ph].

[6] S. Profumo and C. E. Yaguna, "A Statistical analysis of supersymmetric dark

matter in the MSSM after WMAP," *Phys. Rev.* **D70** (2004) 095004, arXiv:hep-ph/0407036 [hep-ph].

[7] G. Gelmini, P. Gondolo, A. Soldatenko, and C. E. Yaguna, "The Effect of a late decaying scalar on the neutralino relic density," *Phys. Rev.* **D74** (2006) 083514, arXiv:hep-ph/0605016 [hep-ph].

[8] P. Salati, "Quintessence and the relic density of neutralinos," *Phys. Lett.* **B571** (2003) 121–131, arXiv:astro-ph/0207396 [astro-ph].

[9] S. Profumo and P. Ullio, "SUSY dark matter and quintessence," *JCAP* **0311** (2003) 006, arXiv:hep-ph/0309220 [hep-ph].

[10] T. Moroi and L. Randall, "Wino cold dark matter from anomaly mediated SUSY breaking," *Nucl. Phys.* **B570** (2000) 455–472, arXiv:hep-ph/9906527 [hep-ph].

[11] M. Fujii and K. Hamaguchi, "Nonthermal dark matter via Affleck-Dine baryogenesis and its detection possibility," *Phys. Rev.* **D66** (2002) 083501, arXiv:hep-ph/0205044 [hep-ph].

[12] D. H. Lyth and E. D. Stewart, "Thermal inflation and the moduli problem," *Phys. Rev.* **D53** (1996) 1784–1798, arXiv:hep-ph/9510204 [hep-ph].

[13] L. Knox and M. S. Turner, "Inflation at the electroweak scale," *Phys. Rev. Lett.* **70** (1993) 371–374, arXiv:astro-ph/9209006 [astro-ph].

[14] G. Nardini, M. Quiros, and A. Wulzer, "A Confining Strong First-Order Electroweak Phase Transition," *JHEP* **0709** (2007) 077, arXiv:0706.3388 [hep-ph].

[15] M. Fukugita and C. Hogan, "Quark soup: Do not boil," *Nature* **354** (1991) 17–18.

[16] G. Jungman, M. Kamionkowski, and K. Griest, "Supersymmetric dark matter," *Phys. Rept.* **267** (1996) 195–373, arXiv:hep-ph/9506380 [hep-ph].

[17] K. Rummukainen, M. Tsypin, K. Kajantie, M. Laine, and M. E. Shaposhnikov, "The Universality class of the electroweak theory," *Nucl. Phys.* **B532** (1998) 283–314, arXiv:hep-lat/9805013 [hep-lat].

[18] D. O'Connell, M. J. Ramsey-Musolf, and M. B. Wise, "Minimal Extension of the Standard Model Scalar Sector," *Phys. Rev.* **D75** (2007) 037701, arXiv:hep-ph/0611014 [hep-ph].

[19] S. Profumo, M. J. Ramsey-Musolf, and G. Shaughnessy, "Singlet Higgs phenomenology and the electroweak phase transition," *JHEP* **0708** (2007) 010, arXiv:0705.2425 [hep-ph].

[20] V. Barger, P. Langacker, M. McCaskey, M. J. Ramsey-Musolf, and G. Shaughnessy, "LHC Phenomenology of an Extended Standard Model with a Real Scalar Singlet," *Phys. Rev.* **D77** (2008) 035005, arXiv:0706.4311 [hep-ph].

[21] R. Schabinger and J. D. Wells, "A Minimal spontaneously broken hidden sector and its impact on Higgs boson physics at the large hadron collider," *Phys. Rev.* **D72** (2005) 093007, arXiv:hep-ph/0509209 [hep-ph].

[22] B. Patt and F. Wilczek, "Higgs-field portal into hidden sectors," arXiv:hep-ph/0605188 [hep-ph].

[23] M. Bowen, Y. Cui, and J. D. Wells, "Narrow trans-TeV Higgs bosons and H —¿; hh decays: Two LHC search paths for a hidden sector Higgs boson," *JHEP* **0703** (2007) 036, arXiv:hep-ph/0701035 [hep-ph].

[24] J. R. Espinosa and M. Quiros, "Novel Effects in Electroweak Breaking from a Hidden Sector," *Phys. Rev.* **D76** (2007) 076004, arXiv:hep-ph/0701145 [hep-ph].

[25] J. Espinosa, T. Konstandin, J. No, and M. Quiros, "Some Cosmological Implications of Hidden Sectors," *Phys. Rev.* **D78** (2008) 123528, arXiv:0809.3215 [hep-ph].

[26] M. Quiros, "Finite temperature field theory and phase transitions," arXiv:hep-ph/9901312 [hep-ph].

[27] M. S. Carena, M. Quiros, M. Seco, and C. Wagner, "Improved results in supersymmetric electroweak baryogenesis," *Nucl. Phys.* **B650** (2003) 24–42, arXiv:hep-ph/0208043 [hep-ph].

[28] T. Konstandin, T. Prokopec, M. G. Schmidt, and M. Seco, "MSSM electroweak baryogenesis and flavor mixing in transport equations," *Nucl. Phys.* **B738** (2006) 1–22, arXiv:hep-ph/0505103 [hep-ph].

[29] V. Cirigliano, S. Profumo, and M. J. Ramsey-Musolf, "Baryogenesis, Electric Dipole Moments and Dark Matter in the MSSM," *JHEP* **0607** (2006) 002, arXiv:hep-ph/0603246 [hep-ph].

[30] M. Carena, G. Nardini, M. Quiros, and C. Wagner, "The Baryogenesis Window in the MSSM," *Nucl. Phys.* **B812** (2009) 243–263, arXiv:0809.3760 [hep-ph].

[31] E. A. Baltz, M. Battaglia, M. E. Peskin, and T. Wizansky, "Determination of dark matter properties at high-energy colliders," *Phys. Rev.* **D74** (2006) 103521, arXiv:hep-ph/0602187 [hep-ph].

[32] A. Megevand and A. D. Sanchez, "Supercooling and phase coexistence in cosmological phase transitions," *Phys. Rev.* **D77** (2008) 063519, arXiv:0712.1031 [hep-ph].

[33] G. W. Anderson and L. J. Hall, "The Electroweak phase transition and baryogenesis," *Phys. Rev.* **D45** (1992) 2685–2698.

[34] J. Ignatius, K. Kajantie, H. Kurki-Suonio, and M. Laine, "The growth of bubbles in cosmological phase transitions," *Phys. Rev.* **D49** (1994) 3854–3868, arXiv:astro-ph/9309059 [astro-ph].

[35] S. R. Coleman, "The Fate of the False Vacuum. 1. Semiclassical Theory," *Phys. Rev.* **D15** (1977) 2929–2936.

[36] J. Callan, Curtis G. and S. R. Coleman, "The Fate of the False Vacuum. 2. First Quantum Corrections," *Phys. Rev.* **D16** (1977) 1762–1768.

[37] A. D. Linde, "Fate of the False Vacuum at Finite Temperature: Theory and Applications," *Phys. Lett.* **B100** (1981) 37.

[38] E. W. Kolb and M. S. Turner, "The Early universe," *Front. Phys.* **69** (1990) 1–547.

[39] P. Gondolo, J. Edsjo, P. Ullio, L. Bergstrom, M. Schelke, *et al.*, "DarkSUSY:

Computing supersymmetric dark matter properties numerically," *JCAP* **0407** (2004) 008, arXiv:astro-ph/0406204 [astro-ph].

[40] P. Gondolo and G. Gelmini, "Cosmic abundances of stable particles: Improved analysis," *Nucl. Phys.* **B360** (1991) 145–179.

[41] V. Silveira and A. Zee, "SCALAR PHANTOMS," *Phys. Lett.* **B161** (1985) 136.

[42] J. McDonald, "Gauge singlet scalars as cold dark matter," *Phys. Rev.* **D50** (1994) 3637–3649, arXiv:hep-ph/0702143 [HEP-PH].

[43] D. E. Holz and A. Zee, "Collisional dark matter and scalar phantoms," *Phys. Lett.* **B517** (2001) 239–242, arXiv:hep-ph/0105284 [hep-ph].

[44] J. McDonald, "Thermally generated gauge singlet scalars as selfinteracting dark matter," *Phys. Rev. Lett.* **88** (2002) 091304, arXiv:hep-ph/0106249 [hep-ph].

[45] C. Burgess, M. Pospelov, and T. ter Veldhuis, "The Minimal model of nonbaryonic dark matter: A Singlet scalar," *Nucl. Phys.* **B619** (2001) 709–728, arXiv:hep-ph/0011335 [hep-ph].

[46] M. Cirelli, N. Fornengo, and A. Strumia, "Minimal dark matter," *Nucl. Phys.* **B753** (2006) 178–194, arXiv:hep-ph/0512090 [hep-ph].

[47] J. March-Russell, S. M. West, D. Cumberbatch, and D. Hooper, "Heavy Dark Matter Through the Higgs Portal," *JHEP* **0807** (2008) 058, arXiv:0801.3440 [hep-ph].

[48] M. Cvetic and P. Langacker, "Implications of Abelian extended gauge structures from string models," *Phys. Rev.* **D54** (1996) 3570–3579, arXiv:hep-ph/9511378 [hep-ph].

[49] G. Giudice and R. Rattazzi, "Theories with gauge mediated supersymmetry breaking," *Phys. Rept.* **322** (1999) 419–499, arXiv:hep-ph/9801271 [hep-ph].

[50] A. Hebecker and J. March-Russell, "The Ubiquitous throat," *Nucl. Phys.* **B781** (2007) 99–111, arXiv:hep-th/0607120 [hep-th].

[51] H. E. Haber and Y. Nir, "MULTISCALAR MODELS WITH A HIGH-ENERGY SCALE," *Nucl. Phys.* **B335** (1990) 363.

[52] J. R. Espinosa and R.-J. Zhang, "Complete two loop dominant corrections to the mass of the lightest CP even Higgs boson in the minimal supersymmetric standard model," *Nucl. Phys.* **B586** (2000) 3–38, arXiv:hep-ph/0003246 [hep-ph].

[53] R. Fok and G. D. Kribs, "Four Generations, the Electroweak Phase Transition, and Supersymmetry," *Phys. Rev.* **D78** (2008) 075023, arXiv:0803.4207 [hep-ph].

[54] E. Witten, "Cosmic Separation of Phases," *Phys. Rev.* **D30** (1984) 272–285.

[55] **Committee for a Decadal Survey of Astonomy and Astrophysics** Collaboration, R. Blanford *et al.*, *New Worlds, New Horizons in Astronomy and Astrophysics*. National Academies Press, Washington, D.C., 2010.

[56] A. Sakharov, "Violation of CP Invariance, c Asymmetry, and Baryon Asymmetry of the Universe," *Pisma Zh. Eksp. Teor. Fiz.* **5** (1967) 32–35. Reprinted in *Kolb, E.W.

(ed.), Turner, M.S. (ed.): The early universe* 371-373, and in *Lindley, D. (ed.) et al.: Cosmology and particle physics* 106-109, and in Sov. Phys. Usp. 34 (1991) 392-393 [Usp. Fiz. Nauk 161 (1991) No. 5 61-64].

[57] M. S. Carena, M. Quiros, and C. Wagner, "Opening the window for electroweak baryogenesis," *Phys. Lett.* **B380** (1996) 81–91, arXiv:hep-ph/9603420 [hep-ph].

[58] S. Huber, P. John, and M. Schmidt, "Bubble walls, CP violation and electroweak baryogenesis in the MSSM," *Eur.Phys.J.* **C20** (2001) 695–711, arXiv:hep-ph/0101249 [hep-ph].

[59] J. Kang, P. Langacker, T.-j. Li, and T. Liu, "Electroweak baryogenesis in a supersymmetric U(1)-prime model," *Phys. Rev. Lett.* **94** (2005) 061801, arXiv:hep-ph/0402086 [hep-ph].

[60] K. Funakubo and E. Senaha, "Electroweak phase transition, critical bubbles and sphaleron decoupling condition in the MSSM," *Phys. Rev.* **D79** (2009) 115024, arXiv:0905.2022 [hep-ph].

[61] C.-W. Chiang and E. Senaha, "Electroweak phase transitions in the secluded U(1)-prime-extended MSSM," *JHEP* **1006** (2010) 030, arXiv:0912.5069 [hep-ph].

[62] A. Ahriche and S. Nasri, "Electroweak Phase Transition in the U(1)'-MSSM," *Phys. Rev.* **D83** (2011) 045032, arXiv:1008.3106 [hep-ph].

[63] D. J. Chung and A. J. Long, "Electroweak Phase Transition in the munuSSM," *Phys. Rev.* **D81** (2010) 123531, arXiv:1004.0942 [hep-ph].

[64] A. Ahriche, "What is the criterion for a strong first order electroweak phase transition in singlet models?," *Phys. Rev.* **D75** (2007) 083522, arXiv:hep-ph/0701192 [hep-ph].

[65] S. Ham, S.-A. Shim, and S. Oh, "Electroweak phase transition in an extension of the standard model with scalar color octet," *Phys. Rev.* **D81** (2010) 055015, arXiv:1002.0237 [hep-ph].

[66] C. Lee, V. Cirigliano, and M. J. Ramsey-Musolf, "Resonant relaxation in electroweak baryogenesis," *Phys. Rev.* **D71** (2005) 075010, arXiv:hep-ph/0412354 [hep-ph].

[67] D. J. Chung, B. Garbrecht, M. J. Ramsey-Musolf, and S. Tulin, "Yukawa Interactions and Supersymmetric Electroweak Baryogenesis," *Phys. Rev. Lett.* **102** (2009) 061301, arXiv:0808.1144 [hep-ph].

[68] V. Cirigliano, Y. Li, S. Profumo, and M. J. Ramsey-Musolf, "MSSM Baryogenesis and Electric Dipole Moments: An Update on the Phenomenology," *JHEP* **1001** (2010) 002, arXiv:0910.4589 [hep-ph].

[69] D. J. Chung, B. Garbrecht, M. Ramsey-Musolf, and S. Tulin, "Supergauge interactions and electroweak baryogenesis," *JHEP* **0912** (2009) 067, arXiv:0908.2187 [hep-ph].

[70] C. Wainwright and S. Profumo, "The Impact of a strongly first-order phase transition on the abundance of thermal relics," *Phys. Rev.* **D80** (2009) 103517, arXiv:0909.1317 [hep-ph].

[71] D. Chung, A. Long, and L.-T. Wang, "Probing the Cosmological Constant and Phase Transitions with Dark Matter," *Phys. Rev.* **D84** (2011) 043523, arXiv:1104.5034 [astro-ph.CO].

[72] D. J. Chung and A. J. Long, "Cosmological Constant, Dark Matter, and Electroweak Phase Transition," arXiv:1108.5193 [astro-ph.CO]. * Temporary entry *.

[73] K. Kajantie, M. Laine, K. Rummukainen, and M. E. Shaposhnikov, "Is there a hot electroweak phase transition at m(H) larger or equal to m(W)?," *Phys. Rev. Lett.* **77** (1996) 2887–2890, arXiv:hep-ph/9605288 [hep-ph].

[74] F. Csikor, Z. Fodor, and J. Heitger, "Endpoint of the hot electroweak phase transition," *Phys. Rev. Lett.* **82** (1999) 21–24, arXiv:hep-ph/9809291 [hep-ph].

[75] Y. Aoki, F. Csikor, Z. Fodor, and A. Ukawa, "The Endpoint of the first order phase transition of the SU(2) gauge Higgs model on a four-dimensional isotropic lattice," *Phys. Rev.* **D60** (1999) 013001, arXiv:hep-lat/9901021 [hep-lat].

[76] **LEP Working Group for Higgs boson searches, ALEPH Collaboration, DELPHI Collaboration, L3 Collaboration, OPAL Collaboration** Collaboration, R. Barate *et al.*, "Search for the standard model Higgs boson at LEP," *Phys. Lett.* **B565** (2003) 61–75, arXiv:hep-ex/0306033 [hep-ex].

[77] N. Turok and J. Zadrozny, "Electroweak baryogenesis in the two doublet model," *Nucl. Phys.* **B358** (1991) 471–493.

[78] K. Funakubo, A. Kakuto, and K. Takenaga, "The Effective potential of electroweak

theory with two massless Higgs doublets at finite temperature," *Prog. Theor. Phys.* **91** (1994) 341–352, arXiv:hep-ph/9310267 [hep-ph].

[79] A. Davies, C. froggatt, G. Jenkins, and R. Moorhouse, "Baryogenesis constraints on two Higgs doublet models," *Phys. Lett.* **B336** (1994) 464–470.

[80] J. M. Cline, K. Kainulainen, and A. P. Vischer, "Dynamics of two Higgs doublet CP violation and baryogenesis at the electroweak phase transition," *Phys. Rev.* **D54** (1996) 2451–2472, arXiv:hep-ph/9506284 [hep-ph].

[81] M. Laine and K. Rummukainen, "Two Higgs doublet dynamics at the electroweak phase transition: A Nonperturbative study," *Nucl. Phys.* **B597** (2001) 23–69, arXiv:hep-lat/0009025 [hep-lat].

[82] L. Fromme, S. J. Huber, and M. Seniuch, "Baryogenesis in the two-Higgs doublet model," *JHEP* **0611** (2006) 038, arXiv:hep-ph/0605242 [hep-ph].

[83] J. M. Cline, K. Kainulainen, and M. Trott, "Electroweak Baryogenesis in Two Higgs Doublet Models and B meson anomalies," arXiv:1107.3559 [hep-ph].

[84] G. D. Moore and K. Rummukainen, "Electroweak bubble nucleation, nonperturbatively," *Phys. Rev.* **D63** (2001) 045002, arXiv:hep-ph/0009132 [hep-ph].

[85] G. D. Moore, K. Rummukainen, and A. Tranberg, "Nonperturbative computation of the bubble nucleation rate in the cubic anisotropy model," *JHEP* **0104** (2001) 017, arXiv:hep-lat/0103036 [hep-lat].

[86] R. Apreda, M. Maggiore, A. Nicolis, and A. Riotto, "Gravitational waves from electroweak phase transitions," *Nucl. Phys.* **B631** (2002) 342–368, arXiv:gr-qc/0107033 [gr-qc].

[87] J. M. Cline, G. D. Moore, and G. Servant, "Was the electroweak phase transition preceded by a color broken phase?," *Phys. Rev.* **D60** (1999) 105035, arXiv:hep-ph/9902220 [hep-ph].

[88] P. John, "Bubble wall profiles with more than one scalar field: A Numerical approach," *Phys. Lett.* **B452** (1999) 221–226, arXiv:hep-ph/9810499 [hep-ph].

[89] T. Konstandin and S. J. Huber, "Numerical approach to multi dimensional phase transitions," *JCAP* **0606** (2006) 021, arXiv:hep-ph/0603081 [hep-ph].

[90] J.-h. Park, "Constrained potential method for false vacuum decays," *JCAP* **1102** (2011) 023, arXiv:1011.4936 [hep-ph].

[91] S. Profumo, L. Ubaldi, and C. Wainwright, "Singlet Scalar Dark Matter: monochromatic gamma rays and metastable vacua," *Phys. Rev.* **D82** (2010) 123514, arXiv:1009.5377 [hep-ph].

[92] C. Wainwright, S. Profumo, and M. J. Ramsey-Musolf, "Gravity Waves from a Cosmological Phase Transition: Gauge Artifacts and Daisy Resummations," *Phys. Rev.* **D84** (2011) 023521, arXiv:1104.5487 [hep-ph].

[93] J. Nelder and R. Mead, "A Simplex Method for Function Minimization," *Comput. J.* **7** (1965) 308–313.

[94] S. Weinberg, "New approach to the renormalization group," *Phys. Rev.* **D8** (1973) 3497–3509.

[95] G. 't Hooft, "Dimensional regularization and the renormalization group," *Nucl. Phys.* **B61** (1973) 455–468.

[96] D. J. Gross, R. D. Pisarski, and L. G. Yaffe, "QCD and Instantons at Finite Temperature," *Rev. Mod. Phys.* **53** (1981) 43.

[97] R. R. Parwani, "Resummation in a hot scalar field theory," *Phys. Rev.* **D45** (1992) 4695, `arXiv:hep-ph/9204216 [hep-ph]`.

[98] **LIGO Collaboration** Collaboration, B. Abbott *et al.*, "Searching for a Stochastic Background of Gravitational Waves with LIGO," *Astrophys. J.* **659** (2007) 918–930, `arXiv:astro-ph/0608606 [astro-ph]`.

[99] R. van Haasteren, Y. Levin, G. Janssen, K. Lazaridis, M. K. B. Stappers, *et al.*, "Placing limits on the stochastic gravitational-wave background using European Pulsar Timing Array data," `arXiv:1103.0576 [astro-ph.CO]`.

[100] F. Antonucci, M. Armano, H. Audley, G. Auger, M. Benedetti, *et al.*, "From laboratory experiments to LISA Pathfinder: achieving LISA geodesic motion," *Class. Quant. Grav.* **28** (2011) 094002, `arXiv:1012.5968 [gr-qc]`.

[101] C. for a Decadal Survey of Astronomy, Astrophysics, and N. R. Council, *New Worlds, New Horizons in Astronomy and Astrophysics*. National Academies Press, 2011.

[102] C. J. Hogan, "Gravitational radiation from cosmological phase transitions," *MNRAS* **218** (Feb., 1986) 629–636.

[103] M. S. Turner and F. Wilczek, "Relic gravitational waves and extended inflation," *Phys. Rev. Lett.* **65** (1990) 3080–3083.

[104] A. Kosowsky, M. S. Turner, and R. Watkins, "Gravitational waves from first order cosmological phase transitions," *Phys. Rev. Lett.* **69** (1992) 2026–2029.

[105] M. Maggiore, "Gravitational wave experiments and early universe cosmology," *Phys. Rept.* **331** (2000) 283–367, arXiv:gr-qc/9909001 [gr-qc].

[106] V. Rubakov and M. Shaposhnikov, "Electroweak baryon number nonconservation in the early universe and in high-energy collisions," *Usp. Fiz. Nauk* **166** (1996) 493–537, arXiv:hep-ph/9603208 [hep-ph].

[107] S. J. Huber and T. Konstandin, "Gravitational Wave Production by Collisions: More Bubbles," *JCAP* **0809** (2008) 022, arXiv:0806.1828 [hep-ph].

[108] C. Caprini, R. Durrer, T. Konstandin, and G. Servant, "General Properties of the Gravitational Wave Spectrum from Phase Transitions," *Phys. Rev.* **D79** (2009) 083519, arXiv:0901.1661 [astro-ph.CO].

[109] V. Kuzmin, V. Rubakov, and M. Shaposhnikov, "On the Anomalous Electroweak Baryon Number Nonconservation in the Early Universe," *Phys. Lett.* **B155** (1985) 36.

[110] S. M. Chung, A. H. Gonzalez, D. Clowe, D. Zaritsky, M. Markevitch, *et al.*,

"Impacts of a Supersonic Shock Front on Star Formation in the Bullet Cluster," *Astrophys. J.* **691** (2009) 963–970, arXiv:0810.1052 [astro-ph].

[111] M. Maggiore, "Stochastic backgrounds of gravitational waves," arXiv:gr-qc/0008027 [gr-qc].

[112] J. Kehayias and S. Profumo, "Semi-Analytic Calculation of the Gravitational Wave Signal From the Electroweak Phase Transition for General Quartic Scalar Effective Potentials," *JCAP* **1003** (2010) 003, arXiv:0911.0687 [hep-ph].

[113] L. Dolan and R. Jackiw, "Symmetry Behavior at Finite Temperature," *Phys. Rev.* **D9** (1974) 3320–3341.

[114] L. Dolan and R. Jackiw, "Gauge Invariant Signal for Gauge Symmetry Breaking," *Phys. Rev.* **D9** (1974) 2904.

[115] D. Metaxas and E. J. Weinberg, "Gauge independence of the bubble nucleation rate in theories with radiative symmetry breaking," *Phys. Rev.* **D53** (1996) 836–843, arXiv:hep-ph/9507381 [hep-ph].

[116] N. Nielsen, "On the Gauge Dependence of Spontaneous Symmetry Breaking in Gauge Theories," *Nucl. Phys.* **B101** (1975) 173.

[117] R. Fukuda and T. Kugo, "Gauge Invariance in the Effective Action and Potential," *Phys. Rev.* **D13** (1976) 3469.

[118] H. H. Patel and M. J. Ramsey-Musolf, "Baryon Washout, Electroweak Phase

Transition, and Perturbation Theory," *JHEP* **1107** (2011) 029, arXiv:1101.4665 [hep-ph].

[119] M. Laine, "Gauge dependence of the high temperature two loop effective potential for the Higgs field," *Phys. Rev.* **D51** (1995) 4525–4532, arXiv:hep-ph/9411252 [hep-ph].

[120] J. Baacke and S. Junker, "Quantum fluctuations around the electroweak sphaleron," *Phys. Rev.* **D49** (1994) 2055–2073, arXiv:hep-ph/9308310 [hep-ph].

[121] J. Baacke and S. Junker, "Quantum fluctuations of the electroweak sphaleron: Erratum and addendum," *Phys. Rev.* **D50** (1994) 4227–4228, arXiv:hep-th/9402078 [hep-th].

[122] D. Boyanovsky, D. Brahm, R. Holman, and D. Lee, "The Gauge invariant effective potential: Equilibrium and nonequilibrium aspects," *Phys. Rev.* **D54** (1996) 1763–1777, arXiv:hep-ph/9603337 [hep-ph].

[123] W. Fischler and R. Brout, "Gauge Invariance in Spontaneously Broken Symmetry," *Phys. Rev.* **D11** (1975) 905.

[124] C. Delaunay, C. Grojean, and J. D. Wells, "Dynamics of Non-renormalizable Electroweak Symmetry Breaking," *JHEP* **0804** (2008) 029, arXiv:0711.2511 [hep-ph].

[125] P. B. Arnold and O. Espinosa, "The Effective potential and first order phase transitions: Beyond leading-order," *Phys. Rev.* **D47** (1993) 3546, arXiv:hep-ph/9212235 [hep-ph].

[126] M. S. Turner, E. J. Weinberg, and L. M. Widrow, "Bubble nucleation in first order inflation and other cosmological phase transitions," *Phys. Rev.* **D46** (1992) 2384–2403.

[127] P. J. Steinhardt, "RELATIVISTIC DETONATION WAVES AND BUBBLE GROWTH IN FALSE VACUUM DECAY," *Phys. Rev.* **D25** (1982) 2074.

[128] G. Gogoberidze, T. Kahniashvili, and A. Kosowsky, "The Spectrum of Gravitational Radiation from Primordial Turbulence," *Phys. Rev.* **D76** (2007) 083002, arXiv:0705.1733 [astro-ph].

[129] T. Kahniashvili, A. Kosowsky, G. Gogoberidze, and Y. Maravin, "Detectability of Gravitational Waves from Phase Transitions," *Phys. Rev.* **D78** (2008) 043003, arXiv:0806.0293 [astro-ph].

[130] L.-s. Chen, M. Belloni, and K. Haller, "Gauss' law and gauge invariant operators and states in QCD," *Phys. Rev.* **D55** (1997) 2347–2366, arXiv:hep-ph/9609507 [hep-ph].

[131] K. Haller, "Using gauge-invariant variables in QCD," arXiv:hep-th/0307272 [hep-th].

[132] G. Baym, D. Bodeker, and L. D. McLerran, "Magnetic fields produced by phase transition bubbles in the electroweak phase transition," *Phys. Rev.* **D53** (1996) 662–667, arXiv:hep-ph/9507429 [hep-ph].

[133] M. Trodden, "Electroweak baryogenesis," *Rev. Mod. Phys.* **71** (1999) 1463–1500, arXiv:hep-ph/9803479 [hep-ph].

[134] R. Durrer, "Gravitational waves from cosmological phase transitions," *J. Phys.Conf.Ser.* **222** (2010) 012021, arXiv:1002.1389 [astro-ph.CO].

[135] A. Neronov and I. Vovk, "Evidence for strong extragalactic magnetic fields from Fermi observations of TeV blazars," *Science* **328** (2010) 73–75, arXiv:1006.3504 [astro-ph.HE].

[136] K. Dolag, M. Kachelriess, S. Ostapchenko, and R. Tomas, "Lower limit on the strength and filling factor of extragalactic magnetic fields," *Astrophys. J.* **727** (2011) L4, arXiv:1009.1782 [astro-ph.HE].

[137] S. J. Huber, M. Pospelov, and A. Ritz, "Electric dipole moment constraints on minimal electroweak baryogenesis," *Phys. Rev.* **D75** (2007) 036006, arXiv:hep-ph/0610003 [hep-ph].

[138] J. Kozaczuk and S. Profumo, "Closing in on Supersymmetric Electroweak Baryogenesis with Dark Matter Searches and the Large Hadron Collider," *JCAP* **1111** (2011) 031, arXiv:1108.0393 [hep-ph].

[139] S. Cohen and P. Kowalski, "Precision sbRIO-based Magnet Power Supply Annunciator and Control Interface for Accelerator Control Systems," *Conf.Proc.* **C1205201** (2012) 3668–3670.

[140] **TEVNPH (Tevatron New Phenomina and Higgs Working Group), CDF Collaboration, D0 Collaboration** Collaboration, "Combined CDF and D0 Upper Limits on Standard Model Higgs Boson Production with up to 8.6 fb^{-1} of Data," arXiv:1107.5518 [hep-ex].

[141] **CMS Collaboration** Collaboration, V. Khachatryan *et al.*, "Search for Supersymmetry in pp Collisions at 7 TeV in Events with Jets and Missing Transverse Energy," *Phys. Lett.* **B698** (2011) 196–218, arXiv:1101.1628 [hep-ex].

[142] **Atlas Collaboration** Collaboration, G. Aad *et al.*, "Search for supersymmetry using final states with one lepton, jets, and missing transverse momentum with the ATLAS detector in $\sqrt{s} = 7$ TeV pp," *Phys. Rev. Lett.* **106** (2011) 131802, arXiv:1102.2357 [hep-ex].

[143] G. F. Giudice, "The Electroweak phase transition in supersymmetry," *Phys. Rev.* **D45** (1992) 3177–3182.

[144] A. Menon, D. Morrissey, and C. Wagner, "Electroweak baryogenesis and dark matter in the nMSSM," *Phys. Rev.* **D70** (2004) 035005, arXiv:hep-ph/0404184 [hep-ph].

[145] S. J. Huber, T. Konstandin, T. Prokopec, and M. G. Schmidt, "Electroweak Phase Transition and Baryogenesis in the nMSSM," *Nucl. Phys.* **B757** (2006) 172–196, arXiv:hep-ph/0606298 [hep-ph].

[146] K. Blum and Y. Nir, "Beyond MSSM Baryogenesis," *Phys. Rev.* **D78** (2008) 035005, arXiv:0805.0097 [hep-ph].

[147] K. Farakos, K. Kajantie, K. Rummukainen, and M. E. Shaposhnikov, "3-d physics and the electroweak phase transition: A Framework for lattice Monte Carlo analysis," *Nucl. Phys.* **B442** (1995) 317–363, arXiv:hep-lat/9412091 [hep-lat].

[148] S. Weinberg, "Gauge and Global Symmetries at High Temperature," *Phys. Rev.* **D9** (1974) 3357–3378.

[149] Y. Ueda, "GAUGE DEPENDENCE OF MASSES IN THE GAUGE THEORY AT FINITE TEMPERATURE," *Phys. Rev.* **D23** (1981) 1383.

[150] P. B. Arnold, E. Braaten, and S. Vokos, "Resolving the unitary gauge puzzle of thermal phase transitions," *Phys. Rev.* **D46** (1992) 3576–3586.

[151] P. Kelly, R. Kobes, and G. Kunstatter, "Parameterization invariance and the resolution of the unitary gauge puzzle," *Phys. Rev.* **D50** (1994) 7592–7602, arXiv:hep-ph/9406298 [hep-ph].

[152] J. R. Espinosa, T. Konstandin, and F. Riva, "Strong Electroweak Phase Transitions in the Standard Model with a Singlet," *Nucl. Phys.* **B854** (2012) 592–630, arXiv:1107.5441 [hep-ph].

[153] C. L. Wainwright, "CosmoTransitions: Computing Cosmological Phase Transition Temperatures and Bubble Profiles with Multiple Fields," *Comput. Phys. Commun.* **183** (2012) 2006–2013, arXiv:1109.4189 [hep-ph].

[154] A. Abdo, M. Ackermann, M. Ajello, W. Atwood, L. Baldini, *et al.*, "Fermi LAT Search for Photon Lines from 30 to 200 GeV and Dark Matter Implications," *Phys. Rev. Lett.* **104** (2010) 091302, arXiv:1001.4836 [astro-ph.HE].

[155] A. Albert, "Search for Gamma-ray Spectral Lines in the Milky Way Diffuse with the Fermi Large Area Telescope." http://fermi.gsfc.nasa.gov/science/mtgs/symposia/2012/program/fri/AAlbert.pdf, 2012. Slides given at the Fermi Symposium. Accessed: 2013-05-02.

[156] C. Weniger, "A Tentative Gamma-Ray Line from Dark Matter Annihilation at the Fermi Large Area Telescope," *JCAP* **1208** (2012) 007, arXiv:1204.2797 [hep-ph].

[157] T. Bringmann, X. Huang, A. Ibarra, S. Vogl, and C. Weniger, "Fermi LAT Search for Internal Bremsstrahlung Signatures from Dark Matter Annihilation," *JCAP* **1207** (2012) 054, arXiv:1203.1312 [hep-ph].

[158] M. Su and D. P. Finkbeiner, "Strong Evidence for Gamma-ray Line Emission from the Inner Galaxy," arXiv:1206.1616 [astro-ph.HE].

[159] D. P. Finkbeiner, M. Su, and C. Weniger, "Is the 130 GeV Line Real? A Search for Systematics in the Fermi-LAT Data," *JCAP* **1301** (2013) 029, arXiv:1209.4562 [astro-ph.HE].

[160] L. Bergstrom and P. Ullio, "Full one loop calculation of neutralino annihilation into two photons," *Nucl. Phys.* **B504** (1997) 27–44, arXiv:hep-ph/9706232 [hep-ph].

[161] D. Das, U. Ellwanger, and P. Mitropoulos, "A 130 GeV photon line from dark matter annihilation in the NMSSM," *JCAP* **1208** (2012) 003, arXiv:1206.2639 [hep-ph].

[162] D. E. Morrissey and M. J. Ramsey-Musolf, "Electroweak baryogenesis," *New J. Phys.* **14** (2012) 125003, arXiv:1206.2942 [hep-ph].

[163] M. Pietroni, "The Electroweak phase transition in a nonminimal supersymmetric model," *Nucl. Phys.* **B402** (1993) 27–45, arXiv:hep-ph/9207227 [hep-ph].

[164] K. Funakubo, S. Tao, and F. Toyoda, "Phase transitions in the NMSSM," *Prog. Theor. Phys.* **114** (2005) 369–389, arXiv:hep-ph/0501052 [hep-ph].

[165] K. Cheung, T.-J. Hou, J. S. Lee, and E. Senaha, "Singlino-driven Electroweak Baryogenesis in the Next-to-MSSM," *Phys. Lett.* **B710** (2012) 188–191, arXiv:1201.3781 [hep-ph].

[166] **CMS Collaboration** Collaboration, S. Chatrchyan *et al.*, "Observation of a new boson at a mass of 125 GeV with the CMS experiment at the LHC," *Phys. Lett.* **B716** (2012) 30–61, arXiv:1207.7235 [hep-ex].

[167] **ATLAS Collaboration** Collaboration, G. Aad *et al.*, "Observation of a new particle in the search for the Standard Model Higgs boson with the ATLAS detector at the LHC," *Phys. Lett.* **B716** (2012) 1–29, arXiv:1207.7214 [hep-ex].

[168] G. Chalons, M. J. Dolan, and C. McCabe, "Neutralino dark matter and the Fermi gamma-ray lines," *JCAP* **1302** (2013) 016, arXiv:1211.5154 [hep-ph].

[169] U. Ellwanger, J. F. Gunion, and C. Hugonie, "NMHDECAY: A Fortran code for the Higgs masses, couplings and decay widths in the NMSSM," *JHEP* **0502** (2005) 066, arXiv:hep-ph/0406215 [hep-ph].

[170] Y. Li, S. Profumo, and M. Ramsey-Musolf, "Bino-driven Electroweak Baryogenesis with highly suppressed Electric Dipole Moments," *Phys. Lett.* **B673** (2009) 95–100, arXiv:0811.1987 [hep-ph].

[171] R. Harnik, G. D. Kribs, D. T. Larson, and H. Murayama, "The Minimal

supersymmetric fat Higgs model," *Phys. Rev.* **D70** (2004) 015002, arXiv:hep-ph/0311349 [hep-ph].

[172] E. Hardy, J. March-Russell, and J. Unwin, "Precision Unification in λ SUSY with a 125 GeV Higgs," *JHEP* **1210** (2012) 072, arXiv:1207.1435 [hep-ph].

[173] U. Ellwanger and C. Hugonie, "NMHDECAY 2.0: An Updated program for sparticle masses, Higgs masses, couplings and decay widths in the NMSSM," *Comput. Phys. Commun.* **175** (2006) 290–303, arXiv:hep-ph/0508022 [hep-ph].

[174] G. Belanger, F. Boudjema, C. Hugonie, A. Pukhov, and A. Semenov, "Relic density of dark matter in the NMSSM," *JCAP* **0509** (2005) 001, arXiv:hep-ph/0505142 [hep-ph].

[175] G. Belanger, F. Boudjema, P. Brun, A. Pukhov, S. Rosier-Lees, *et al.*, "Indirect search for dark matter with micrOMEGAs2.4," *Comput. Phys. Commun.* **182** (2011) 842–856, arXiv:1004.1092 [hep-ph].

[176] **LAT Collaboration** Collaboration, M. Ackermann *et al.*, "Fermi LAT Search for Dark Matter in Gamma-ray Lines and the Inclusive Photon Spectrum," *Phys. Rev.* **D86** (2012) 022002, arXiv:1205.2739 [astro-ph.HE].

[177] T. Cohen, M. Lisanti, T. R. Slatyer, and J. G. Wacker, "Illuminating the 130 GeV Gamma Line with Continuum Photons," *JHEP* **1210** (2012) 134, arXiv:1207.0800 [hep-ph].

[178] **WMAP Collaboration** Collaboration, E. Komatsu *et al.*, "Seven-Year Wilkinson

Microwave Anisotropy Probe (WMAP) Observations: Cosmological Interpretation," *Astrophys. J.Suppl.* **192** (2011) 18, arXiv:1001.4538 [astro-ph.CO].

[179] M. Carena, S. Gori, N. R. Shah, C. E. Wagner, and L.-T. Wang, "Light Stau Phenomenology and the Higgs $\gamma\gamma$ Rate," *JHEP* **1207** (2012) 175, arXiv:1205.5842 [hep-ph].

[180] **XENON100 Collaboration** Collaboration, E. Aprile *et al.*, "Dark Matter Results from 225 Live Days of XENON100 Data," *Phys. Rev. Lett.* **109** (2012) 181301, arXiv:1207.5988 [astro-ph.CO].

[181] A. Thomas, P. Shanahan, and R. Young, "Strangeness in the nucleon: what have we learned?," *Nuovo Cim.* **C035N04** (2012) 3–10, arXiv:1202.6407 [nucl-th].

[182] C. L. Wainwright, S. Profumo, and M. J. Ramsey-Musolf, "Phase Transitions and Gauge Artifacts in an Abelian Higgs Plus Singlet Model," *Phys. Rev.* **D86** (2012) 083537, arXiv:1204.5464 [hep-ph].

[183] C. Balazs, M. S. Carena, and C. Wagner, "Dark matter, light stops and electroweak baryogenesis," *Phys. Rev.* **D70** (2004) 015007, arXiv:hep-ph/0403224 [hep-ph].

[184] M. Garny and T. Konstandin, "On the gauge dependence of vacuum transitions at finite temperature," *JHEP* **1207** (2012) 189, arXiv:1205.3392 [hep-ph].

[185] J. Kozaczuk, S. Profumo, M. J. Ramsey-Musolf, and C. L. Wainwright, "Supersymmetric Electroweak Baryogenesis Via Resonant Sfermion Sources," *Phys. Rev.* **D86** (2012) 096001, arXiv:1206.4100 [hep-ph].

[186] J. Moreno, M. Quiros, and M. Seco, "Bubbles in the supersymmetric standard model," *Nucl. Phys.* **B526** (1998) 489–500, arXiv:hep-ph/9801272 [hep-ph].

[187] D. J. Chung, B. Garbrecht, M. J. Ramsey-Musolf, and S. Tulin, "Lepton-mediated electroweak baryogenesis," *Phys. Rev.* **D81** (2010) 063506, arXiv:0905.4509 [hep-ph].

[188] V. Cirigliano, M. J. Ramsey-Musolf, S. Tulin, and C. Lee, "Yukawa and tri-scalar processes in electroweak baryogenesis," *Phys. Rev.* **D73** (2006) 115009, arXiv:hep-ph/0603058 [hep-ph].

[189] G. Giudice and M. E. Shaposhnikov, "Strong sphalerons and electroweak baryogenesis," *Phys. Lett.* **B326** (1994) 118–124, arXiv:hep-ph/9311367 [hep-ph].

[190] J. Kozaczuk, S. Profumo, and C. L. Wainwright, "Accidental Supersymmetric Dark Matter and Baryogenesis," *JCAP* **1301** (2013) 027, arXiv:1208.5166 [hep-ph].

[191] M. S. Carena, J. Moreno, M. Quiros, M. Seco, and C. Wagner, "Supersymmetric CP violating currents and electroweak baryogenesis," *Nucl. Phys.* **B599** (2001) 158–184, arXiv:hep-ph/0011055 [hep-ph].

[192] J. M. Cline and K. Kainulainen, "A New source for electroweak baryogenesis in the MSSM," *Phys. Rev. Lett.* **85** (2000) 5519–5522, arXiv:hep-ph/0002272 [hep-ph].

[193] T. Konstandin, T. Prokopec, and M. G. Schmidt, "Axial currents from CKM matrix CP violation and electroweak baryogenesis," *Nucl. Phys.* **B679** (2004) 246–260, arXiv:hep-ph/0309291 [hep-ph].

[194] T. Konstandin, T. Prokopec, and M. G. Schmidt, "Kinetic description of fermion flavor mixing and CP-violating sources for baryogenesis," *Nucl. Phys.* **B716** (2005) 373–400, arXiv:hep-ph/0410135 [hep-ph].

[195] J. R. Ellis, J. S. Lee, and A. Pilaftsis, "Electric Dipole Moments in the MSSM Reloaded," *JHEP* **0810** (2008) 049, arXiv:0808.1819 [hep-ph].

[196] J. Hudson, D. Kara, I. Smallman, B. Sauer, M. Tarbutt, *et al.*, "Improved measurement of the shape of the electron," *Nature* **473** (2011) 493–496.

[197] C. Baker, D. Doyle, P. Geltenbort, K. Green, M. van der Grinten, *et al.*, "An Improved experimental limit on the electric dipole moment of the neutron," *Phys. Rev. Lett.* **97** (2006) 131801, arXiv:hep-ex/0602020 [hep-ex].

[198] W. Griffith, M. Swallows, T. Loftus, M. Romalis, B. Heckel, *et al.*, "Improved Limit on the Permanent Electric Dipole Moment of Hg-199," *Phys. Rev. Lett.* **102** (2009) 101601.

[199] J. Hewett, H. Weerts, R. Brock, J. Butler, B. Casey, *et al.*, "Fundamental Physics at the Intensity Frontier," arXiv:1205.2671 [hep-ex].

[200] K. Schmidt-Hoberg, F. Staub, and M. W. Winkler, "Enhanced diphoton rates at Fermi and the LHC," *JHEP* **1301** (2013) 124, arXiv:1211.2835 [hep-ph].

[201] D. Comelli and J. Espinosa, "Bosonic thermal masses in supersymmetry," *Phys. Rev.* **D55** (1997) 6253–6263, arXiv:hep-ph/9606438 [hep-ph].